Polysubstance and Alcohol Dependence: Unique Abnormalities of Magnetic Resonance-Derived Brain Metabolite Levels

Christoph Abé, Anderson Mon, Timothy C. Durazzo, David L Pennington, Thomas P Schmidt and Dieter J. Meyerhoff

Neurodegeneration RIG, CIND VA Medical Center

Although comorbid substance misuse is common in alcohol dependence, and polysubstance abusers (PSU) represent the largest group of individuals seeking treatment for drug abuse today, we know little about potential brain abnormalities in this population. Brain magnetic resonance spectroscopy studies of mono-substance use disorders (e.g., alcohol or cocaine) reveal abnormal levels of cortical metabolites (reflecting neuronal integrity, cell membrane turnover/synthesis, cellular bioenergetics, gliosis) and altered concentrations of glutamate and γ-aminobutyric acid (GABA). The concurrent misuse of several substances may have unique and different effects on brain biology and function compared to any mono-substance misuse.

High field brain magnetic resonance spectroscopy at 4 Tesla and neurocognitive testing were performed at one month of abstinence in 40 alcohol dependent individuals (ALC), 28 alcohol dependent PSU and 16 drug-free controls. Absolute metabolite concentrations were calculated in anterior cingulate (ACC), parieto-occipital (POC) and dorso-lateral prefrontal cortices (DLPFC).

Compared to ALC, PSU demonstrated significant metabolic abnormalities in the DLPFC and strong trends to lower GABA in the ACC. Metabolite levels in ALC and light drinking controls were statistically equivalent. Within PSU, lower DLPFC GABA levels related to greater cocaine consumption. Several cortical metabolite concentrations were associated with cognitive performance.

While metabolite concentrations in ALC at one month of abstinence were largely normal, PSU showed persistent and functionally significant metabolic abnormalities, primarily in the DLPFC. Our results point to specific metabolic deficits as biomarkers in polysubstance misuse and as targets for pharmacological and behavioral PSU-specific treatment.Supported by NIH AA10788.

Multimodality Imaging of Rheumatoid Arthritis using Quantitative MRI and HR-pQCT

[1]Jose R. Teruel Antolin, [1]Andrew J. Burghardt, [1]Julien Rivoire, [1]Waraporn Srikhum, [1]Susan Noworolski, [1]Thomas M. link, [2]John B. Imboden, [1]Xiaojuan Li
Department of Radiology and Biomedical Imaging, Department of Medicine, UCSF

Purpose To develop advanced multimodality methods using MRI and high-resolution peripheral quantitative computed tomography (HR-pQCT) techniques for quantifying inflammation and joint damage in rheumatoid arthritis. Such quantitative tools will impact clinical trials that determine efficacy of novel therapies and will greatly assist clinicians in optimizing treatment strategies for individual patients. Specifically bone marrow edema (BME) has been suggested as a strong predictor for erosive progression in RA joints, however, no previous studies examined the bone structure within BME. This study aimed to quantify bone structure and perfusion properties of BME, normal bone marrow (NBM) and pannus tissue areas in wrists affected by RA using 3 Tesla MRI and HR-pQCT.

Methods and materials Sixteen RA patients (52.9 ± 12.7 years, 13 females) were imaged in a HR-pQCT system (82µm isotropic voxel) and in a 3T MRI scanner using an 8-channel wrist coil. Coronal T2-weighted fast spin-echo IDEAL and 3D dynamic contrast enhanced images were acquired. BME and pannus tissue areas were segmented semi-automatically in T2-w images. NBM areas were placed 1 to 3 mm far from BME regions and with similar distance to joint space. T2-w images were register to reformatted HR-pQCT and registration was applied to the segmented ROIs that were placed on original HR-pQCT images after upsampling (Figure 1). Perfusion parameters were calculated based on the signal-time curve obtained from DCE-MRI.

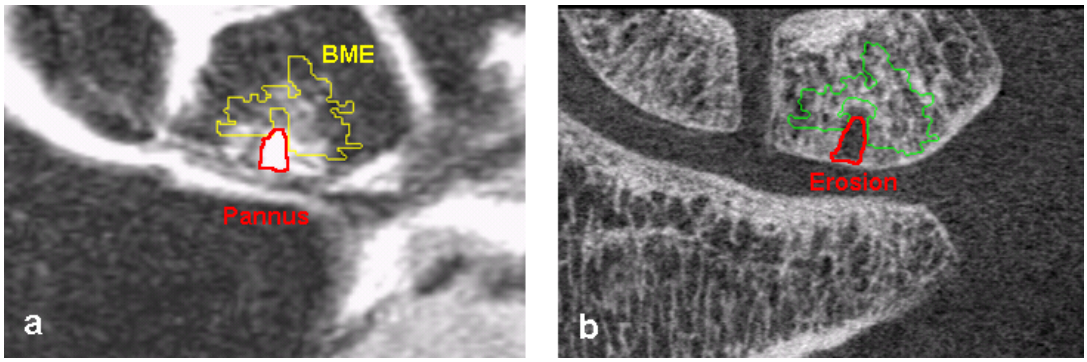

Figure 1. **a:** BME and pannus in T2w IDEAL image. **b:** HR-pQCT showing erosion and BME ROI superimposed.

Results Eleven out of 16 RA patients presented at least one BME region. Eighteen BME areas were segmented, 13 of them were presented around areas evidently affected by pannus tissue. The regions with pannus tissue in MRI always correspond to regions with erosion in HR-pQCT images (Figure 1). Two BME areas were presented next to early stage of pannus tissue (very small quantity of pannus penetrating the bone). For 3 of the BME regions, no pannus tissue were observed (thus no erosion). Significant increases in bone density and trabecular thickness were evidenced in all BME regions (Figure 2).

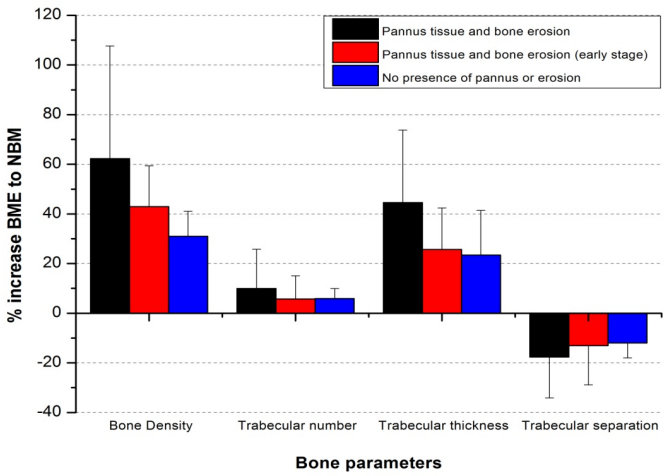

Figure 2. Percentage increase of bone parameters in regions presenting BME with regard to NBM areas ($P < 0.05$).

BME and pannus tissue areas show significantly increased perfusion. The maximum signal enhancement in BME was 20.33 ± 14.33 (% over NBM) within the carpal bones and 21.32 ± 10.52 within the distal radius/ulna. In pannus tissue areas was 16.48 ± 11.34 (% over NBM) within the carpal bones and 32.93 ± 16.71 within the distal radius/ulna.

Conclusions BME regions show a thickening in the trabecular structure that suggests a bone regeneration before pannus tissue produces erosion. Trabecular thickening within BME is higher when pannus tissue is already presented in the patient. This higher thickening suggests sclerosis occurring to protect the bone structure from pannus tissue and kinematic re-adaptation. Combining MRI and HR-pQCT provides a powerful multi-modality approach for better understanding BME and erosion, and identifying novel imaging markers for disease progression and treatment monitoring in RA.

Super-Resolution Track Density Imaging of Glioblastoma: Histopathologic Correlation

Barajas RF Jr., Hess C, Phillips J, Von Morze C, Yu JP, Chang S, Nelson S, McDermott M, Berger M, Cha S

Background: Despite significant advances in combined therapy, Glioblastoma multiforme (GBM) remains an aggressive neoplasm with a poor prognosis, in part, due to the ineffectiveness of MRI at delineating the invading tumor margin. Super-resolution track density imaging (TDI) generates anatomic images with sub-millimeter voxel resolution. We hypothesized that TDI is capable of defining regions of aggressive histopathologic features, such as tumor infiltration and white matter disruption, within GBM.

Methods: 43 tumor specimens (24 contrast enhancing, 12 non-enhancing, and 7 centrally necrotic regions) were collected from 18 patients with treatment-naïve GBM using MRI guided neurosurgical techniques. Immunohistochemical stains were used to evaluate the following histopathological features; hypoxia, architectural disruption, microvascular hyperplasia, and cellular proliferation. Track density maps were reconstructed at 0.25 mm isotropic spatial resolution using probabilistic streamline tractography combined with constrained spherical deconvolution (model order = 8, 0.1 mm size, 1,000,000 seed points). Additionally, fractional anisotropy (FA) maps were constructed. TDI and FA values were obtained from each tumor specimen site. P-value of 0.05 was considered significant. Correlation analysis was adjusted for multiple comparisons using the False Discovery Rate method

Results: All tissue specimens demonstrated the presence of tumor upon histopathologic analysis. None of the histopathologic features were differentially expressed among the three tumor specimen regions (P> 0.16). TDI was not significantly different between the three tumor regions, however, were more likely to be elevated within regions demonstrating aggressive histopathological features irrespective of the presence or absence of contrast enhancement (hypoxia, OR= 3.52, P= 0.01; architectural disruption, OR= 3.49, P = 0.03; and cellular proliferation, OR= 1.70, P = 0.05). When considering all tissue specimens, a strong positive correlation was observed between TDI and all histopathologic measures (P< 0.05). No correlation was found between FA and any histopathologic variable (P > 0.08). Within non-enhancing specimens, TDI positively correlated with hypoxia and architectural disruption (P< 0.05).

Conclusion: TDI is clinically useful for identifying regions of tumor infiltration within both enhancing and non-enhancing components of GBM. The ability to assess for GBM infiltration within similar appearing non-enhancing tissues could have a significant impact on patient management. Future investigations will focus on determining whether TDI can improve patient outcomes by guiding individualized therapeutic strategies within non-enhancing tumor.

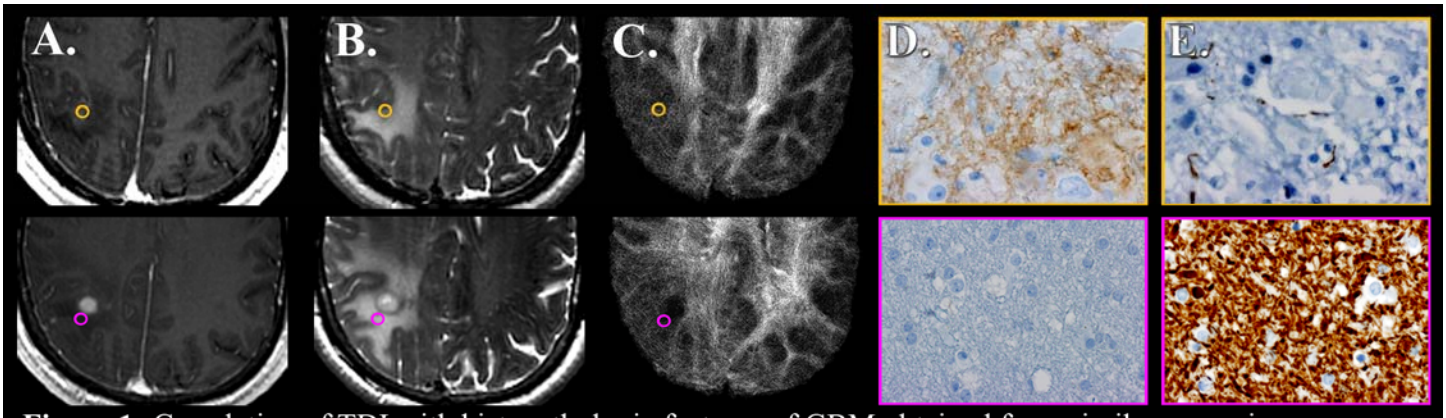

Figure 1: Correlation of TDI with histopathologic features of GBM obtained from similar appearing non-enhancing tumor regions. A) Axial T1 contrast enhanced, (B) FSE-T2, and (C) TDI shows increased TDI measurments (Top Row) within regions demonstrating increased cellular hypxia (D) and archictural disruption (E). This correlation suggests that TDI provides unique information that complements standard MRI sequences by identifying non-enhancing regions significantly infiltrated with tumor.

Susceptibility-weighted MR Imaging of Radiation Therapy-induced Cerebral Microbleeds in Gliomas: A 3T and 7T Comparison Study

Wei Bian[1,2] Christopher P. Hess[2], Susan M. Chang[3], Sarah J. Nelson[1,2,4], and Janine M. Lupo[2]
[1]UCSF and UC Berkeley Graduate Program in Bioengineering ,[2]Radiology and Biomedical Imaging , [3]Neurological Surgery, and [4]Bioengineering and Therapeutic Sciences, University of California San Francisco

BACKGROUND Cerebral microbleeds (CMBs) have been detected in the brain of patients with gliomas after receiving radiation therapy[1]. Although studies have shown improved sensitivity to microbleeds on MR magnitude images at 3T and 7T field strengths compared to 1.5T or by using susceptibility-weighted imaging (SWI)[2,3], it is not clear how much sensitivity is gained with SWI and 7T over 3T.

OBJECTIVE The purpose of this study was to compare radiation-induced microbleed detection between 3T and 7T and determine whether SWI added in the identification of radiation-induced microbleeds.

SUBJECTS and METHODS Ten patients with gliomas who had received prior radiation therapy were scanned at both 3T and 7T GE scanners on the same day. Both acquisitions used a 3D SPGR sequence with GRAPPA-based parallel imaging. Acquisition parameters were as follows: GRAPPA with R=2/3 (3T/7T), TE/TR = 28/56ms (3T) or 16ms/50ms (7T), Flip angle 20°, FOV 24cm, 0.5x0.5x2mm resolution, total scan time around 6 min. Standard SWI image post-processing was performed[4,5]. Minimum intensity projection images through 8 mm-thick slabs were generated from both magnitude and SWI images. Microbleeds were identified as small circular hypointense foci on the projected images. A Wilcoxon signed-rank test was performed to test whether there were significant differences in microbleed detection between groups.

RESULTS and DISCUSSION Similar to 3T, 7T SWI was significantly more sensitive to detecting CMBs compared to 7T magnitude images (p=0.002, Fig.1.a). 3T SWI detected significantly more CMBs than 7T magnitude images (p=0.006), even though at 7T there is already heightened susceptibility in magnitude images (Fig.1.b), indicating that SWI is still necessary at 7T. No group difference (p = 0.172) in CMB detection was found between 7T SWI and 3T SWI when including all 10 patients. However, a significantly more microbleeds (p = 0.016) were detected on 7T SWI after excluding 3 patients who had microbleeds surrounding air-tissue interfaces (Fig.1.c&d).

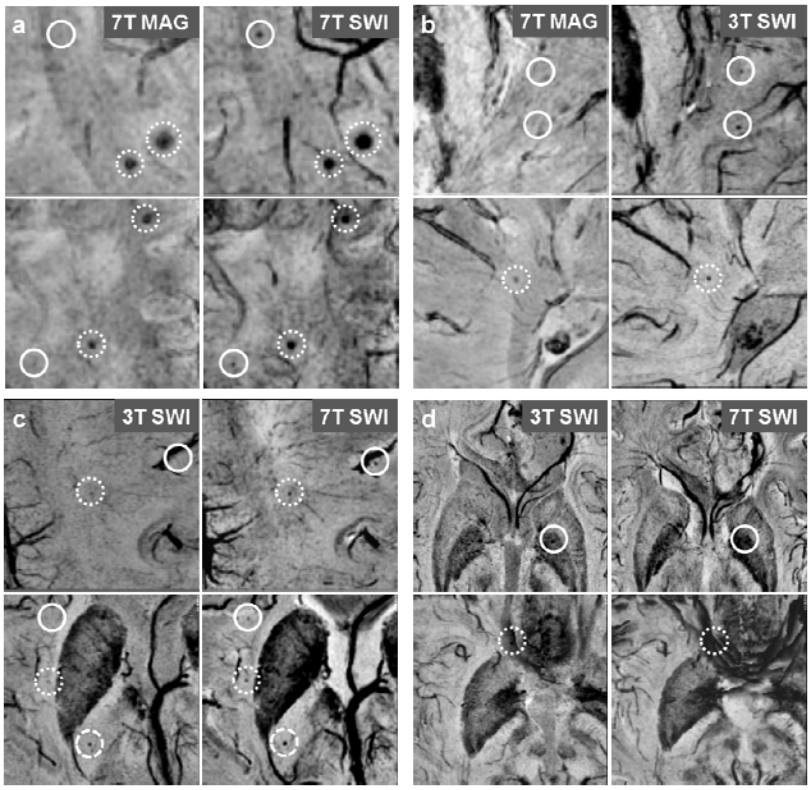

Figure 1. (a) 7T magnitude and SWI images from two patients (*top and bottom rows*). *Solid circles*: CMBs seen on 7T SWI only; *Dashed circles*: CMBs better contrasted on 7T SWI compared to 7T magnitude images. (b) 3T SWI and 7T magnitude images from two patients. *Solid circles*: CMBs seen on 3T SWI only; *Dashed circles*: CMBs better contrasted on 3T SWI compared to 7T magnitude images. (c) 3T and 7T SWI images from two patients. *Solid circles*: CMBs seen on 7T SWI only; *Densely-dashed circles*: CMBs better contrasted on 7T SWI compared to 3T SWI; *Loosely-dashed circles*: CMBs seen on both 7T and 3T SWI . (d) 3T and 7T SWI images from two patients. *Solid circles*: CMBs seen on 3T SWI but masked by the heavy susceptibility effect of iron content in the globus pallidus on 7T SWI; *Dashed circles*: CMBs seen on 3T SWI but masked by the phase wrap artifacts on 7T SWI.

REFERENCES:

1. Lupo JM et al., *Int J Raidat Oncol Biol Phys*. 2012;82(3):493-500
2. Nandigam RN et al., *Am J Neuroradiol*. 2009;30(2):338-43.
3. Conijn MM et al., *Am J Neuroradiol*. 2011;32(6):1043-9.
4. Lupo et al, *MRI*. 2009;27(4):480-488
5. Haacke et al., *MRM*. 2004;52(3):612-8.

CONCLUSIONS 7T SWI is more sensitive to radiation-induced cerebral microbleeds than SWI at 3T as long as the location of microbleeds is not in areas with heightened susceptibility artifacts. To achieve an optimal microbleed detection rate, tumor location should be considered in conjunction with field strength when managing these patients.

***Acknowledgements**: This study was supported by UC Discovery grant ITL-BIO04-10148 and a GEMS program training fellowship.*

Modified deflection model for magnetically steerable endovascular catheters for interventional MRI

Curtis J Caton, Alastair J Martin, Prasheel Lillaney, Aaron D Losey, Ryan S Sincic, Mark W Wilson, Steven W Hetts

Purpose: The purpose of this study is to validate a modified mathematical model for predicting deflections of magnetically steerable endovascular catheters inside clinical MRI scanners.

Background: The deflection model is based on the model derived by Settecase[1]:

$$\frac{\theta}{\sin(\gamma-\theta)} = \frac{nIABL}{EI_A}$$

where θ is the angle the catheter tip is deflected, γ is the initial angle of the catheter tip with respect to the B field, n is the number of coil turns, I is the current delivered, A is the cross-sectional area of the coil, B is the magnetic field strength, L is the unrestrained length of the distal end of the catheter, E is the elastic modulus of the catheter, and I_A is the area moment of inertia of the catheter. The model is modified for a new catheter prototype to take into account the added stiffness of the conducting wires inside the lumen of the catheter. This is done by using composite beam theory to incorporate the stiffness of the wires into the elastic modulus of the Settecase model. The relationship is as follows:

$$E_{equiv} = E_{cath} + \frac{E_{wire}I_{wire}}{I_{cath}}$$

where E_{equiv} is the equivalent elastic modulus to be inserted into the Settecase model, E_{cath} and E_{wire} are the elastic moduli of the original catheter and wires, and I_{cath} and I_{wire} are the area moment of inertias of the catheter and wires. For a 2.3 French catheter with an elastic modulus of 9.46 MPa and four 0.09 mm diameter copper wires, the equivalent elastic modulus is 118.7 MPa.

Materials and Methods: The distal tip of a 2.3 French catheter with a 30 turn copper coil was suspended within a phantom at unrestrained lengths ranging from 4 to 6 cm. Currents between -600 and 600 mA were applied remotely using a DC power supply in the MRI control room. The initial angle between the catheter tip and the main magnetic field was also varied between 30 and 90 degrees. Images were obtained with a 1.5 T scanner using "real-time" balanced SSFP MR pulse sequences.

Results and Conclusion: Observed deflection of the magnetic catheter with conducting wires inside the lumen strongly correlates with our model (R^2=0.89, Figure 1). Future work will aim to use optical measurement techniques to observe catheter deflections directly because of difficulty in measuring deflection angles using MR images. This validated model will serve as a valuable tool in the design of future magnetic catheter prototypes with specific desired deflection properties.

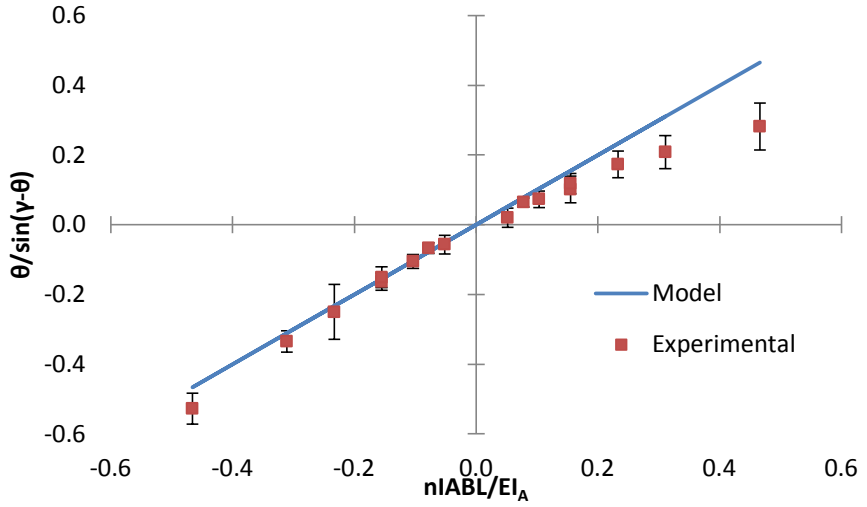

Figure 1: Plot of θ/sin(γ-θ) as a function of nIABL/EI$_A$. Experimental data from observed deflections is shown compared to model predictions (R^2 = 0.89).

[1] Settecase F, *et. al*. "Magnetically-assisted remote control (MARC) steering of endovascular catheters for interventional MRI: a model for deflection and design implications," Med. Phys. **34**, 3135 (2007)

Non-invasive assessment of IDH status in glioblastoma using dynamic ^{13}C MRS of hyperpolarized α-ketoglutarate and hyperpolarized pyruvate

Myriam M. Chaumeil[1], Sarah M. Woods[1], Olivia M. Danforth[1], Hikari A. I. Yoshihara[1], Alessia Lodi[1], Humsa Venkatesh[1], Janine M. Lupo[1], Aaron Robinson[2], Sarah J. Nelson[1], Russell O. Pieper[2,3] Joanna J. Phillips[2,3], Sabrina M. Ronen[1,3]

[1]Surbeck Laboratory of Advanced Imaging, Department of Radiology and Biomedical Imaging, [2]Brain Tumor Research Center, Department of Neurological Surgery, [3]Brain Tumor Research Center, Department of Pathology, University of California, San Francisco, CA, United States

INTRODUCTION Mutations in the isocitrate dehydrogenase (IDH) enzyme have been reported in 70-80% of low grade gliomas and upgraded glioblastomas (GBM)[1]. Inhibitors of mutant IDH are thus under development, raising the need for non-invasive methods enabling monitoring of IDH status. Wild type IDH catalyzes the decarboxylation of isocitrate to α-ketoglutarate (αKG), mutant IDH catalyzes the reduction of αKG into 2-hydroxyglutarate (2HG). To date, IDH status has been assessed mainly through 2HG detection *in vivo* and *ex vivo* using ^{1}H magnetic resonance spectroscopy (MRS)[2]. However, these methods are challenging. Our goal was to evaluate the potential of hyperpolarized (HP) αKG and pyruvate as novel ^{13}C MRS probes to inform on IDH mutational status in gliomas.

MATERIAL & METHODS U87 GBM cells were transduced with a viral vector coding for the wild-type IDH (U87IDHwt) or mutant IDH enzyme (U87IDHmut, R132H variant). Cells were grown on microcarrier beads, ($3.9\pm1.1\times10^7$ U87IDHwt cells, n=7; $3.2\pm0.1\times10^7$ U87IDHmut cells, n=7), and loaded into a 10-mm NMR tube connected to a perfusion system[4]. [1-^{13}C]-αKG or [1-^{13}C]-pyruvate were polarized using a hypersense polarizer (Oxford Instruments) for 1h. Following polarization, αKG/pyruvate was rapidly injected into live perfused cells ([αKG]=15mM, [pyruvate]=5mM). Following addition of HP compound, dynamic sets of HP ^{13}C spectra were acquired on a 500MHz INOVA spectrometer (Agilent Technologies, 13 deg pulses, 3 sec TR). The spectra were quantified using ACD/Spec Manager. Gamma-variate analysis (GVA) was performed on all datasets[5].

RESULTS & DISCUSSION Injection of HP α-KG resulted in build-up of HP glutamate (177.2ppm) in live U87IDHwt cells, whereas HP glutamate was barely detectable in U87IDHmut cells (Fig A&B). HP 2-HG was visible in U87IDHmut cell lysates (183.9ppm). However, due to the presence of the [5-^{13}C] α-KG peak at 184ppm, HP 2-HG could not be resolved unequivocally in the live cell studies. Studies using alternative HP α-KG sources are underway. HP lactate as produced from HP pyruvate was significantly higher in U87IDHwt perfused cells than in U87IDHmut (Fig C). GVA results show significant differences in the time-courses of glutamate and lactate formation between U87IDHwt and mut (Fig C&D, plain line). Results from the activity assays of aspartate transaminase (AST, Fig D), alanine aminotransferase (ALT, Fig E) and glutamate dehydrogenase (GDH, Fig F) suggest that GDH might play a role in the decreased glutamate production in U87IDHmut (57±12% drop, *p=0.01*). Decrease in LDH expression (Fig G) and activity (66±15%, *p=0.03,* Fig H) was also observed in U87IDHmut, in line with the observed drop in HP lactate production. This study demonstrates, to our knowledge for the first time, that HP α-KG permeates the cell membrane, enabling the investigation of its metabolism within a time frame compatible with a ^{13}C MRS experiment. Furthermore, HP α-KG and HP pyruvate are promising agents for interrogation of IDH mutational status, allowing assessment of metabolic reprogramming associated with the presence of this mutation.

REFERENCES 1.Dang et al., Nature (2009) **2.** Elkhaled et al, Sci Trans Med (2012) **4.** Ward et al, Cancer Res (2010) **5.** Lupo et al, MRM (2010)

ACKNOWLEDGMENTS This work was supported by NIH UCSF Brain Tumor SPORE P50 CA097257, NIH R21CA161545 a grant from UCSF Academic Senate, GE Healthcare, a fellowship from the American Brain Tumor Association and NIH NIBIB center grant P41EB013598.

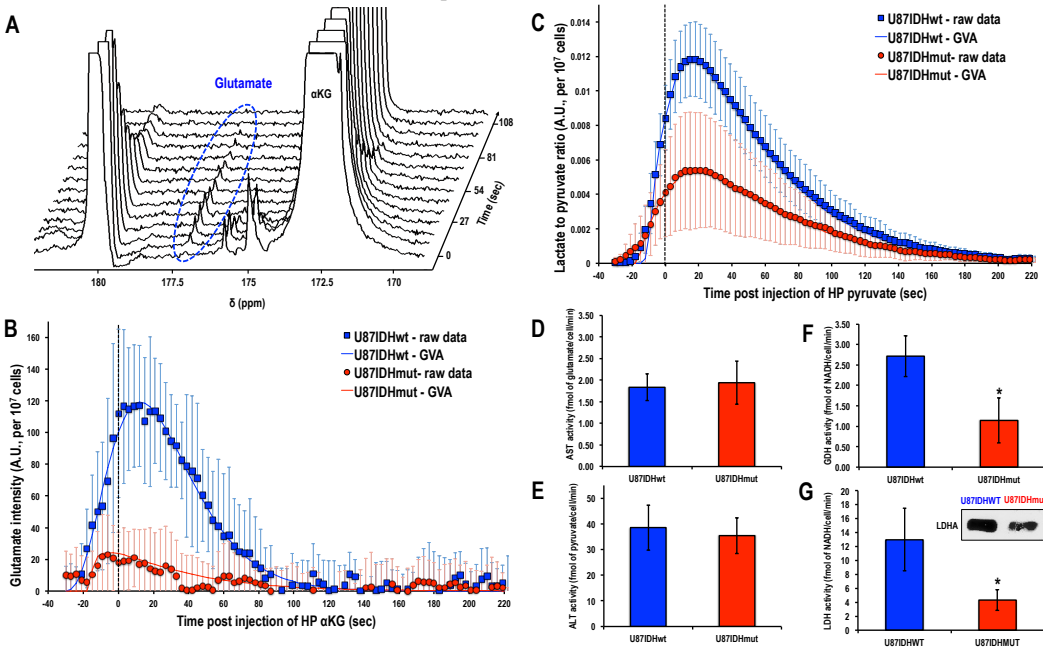

Figure Legend

(A) Stack plot of HP ^{13}C MR spectra following injection of HP [1-^{13}C] αKG in live U87IDHwt perfused cells (temporal resolution 9 sec), showing the formation of HP glutamate.

(B) Intensities of HP glutamate in U87IDHwt (■, GVA plain blue line) and U87IDHmut (○, GVA plain red line) perfused cells, showing the significantly higher level of glutamate in U87IDHwt as well as the delayed formation of HP glutamate

(C) Intensities of HP lactate-to-pyruvate ratio in U87IDHwt (■, GVA plain blue line) and U87IDHmut (○, GVA plain red line) perfused cells, showing the higher level of lactate in U87IDHwt.

(D) AST, **(E)** ALT, **(F)** GDH and **(G)** LDH activities (*$p<0.05$). Western blot analysis of LDHA shows decrease LDH expression in U87IDHmut cells (insert in G).

Diastolic Function Assessed by Cardiac MRI Using Longitudinal Left Ventricular Fractional Shortening

M.N. Dusch[1], S.R. Thadani[1], G.S. Dhillon[1], M.D. Hope[1]
University of California San Francisco, San Francisco, CA

Introduction: Left ventricular diastolic dysfunction (LVDF) is recognized as a significant contributor to morbidity and mortality in congestive heart failure (CHF). Of patients with new onset heart failure, up to 50% have normal left ventricular ejection fractions (LVEF) [1]. Cardiac magnetic resonance imaging (CMR) is a well-established tool to assess systolic dysfunction, but is rarely used to assess LVDF. Midwall longitudinal fractional shortening (MLFS) is a simple parameter shown to correlate with LVDF by echocardiography [2]. Leveraging the superior spatial resolution of CMR, we sought to examine the use of this parameter in the evaluation of LVDF with conventional echocardiography measures serving as a reference.

Methods: The imaging database was reviewed to identify all adult CMR cases with a horizontal long axis (HLA) steady state free precession (SSFP) sequence. Patients were included if they had a transthoracic echocardiogram (TTE) within 6 months of their CMR and LVEF between 55% and 65% by echocardiography. Patients were excluded if they had congenital heart disease, constrictive pericarditis, or a severe valvular defect. LVDF was graded by standard echocardiography criteria as normal (grade 0), impaired relaxation (grade I), pseudonormal (grade III), or restrictive (grade IV). MLFS was determined by calculating the percentage change in the measured distance between the base of the anterior mitral leaflet and the apical endocardium in systole and diastole using SSFP cine sequences in the HLA plane (Figure 1).

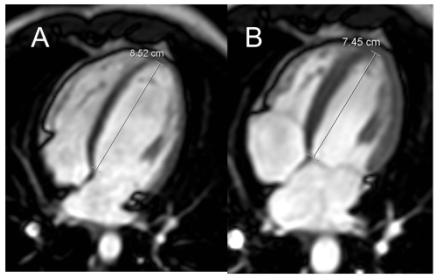

Figure 1: **Sample measurement of MLFS using representative frames from CMR study.** Panel A: Horizontal long axis measurement at end diastole. Panel B: Horizontal long axis measurement at end systole. MLFS calculated from the difference in measurement between Panel A and Panel B.

Results: Following the database review, 80 subjects were identified. LVDF breakdown is as follows: 40 with grade 0, 20 with grade I, 7 with grade III, and 13 with grade IV. The mean MLFS was significantly lower in patients with grade III or IV LVDF compared with grade 0 or I (Table 1). There was also a significant difference between grade 0 and I LVDF (Table 2).

Table 1: Normal vs. Abnormal LVDF measurement of MLFS

LVDF Grade 0/I MLFS % (95% Confidence Interval) n=60	LVDF Grade II/III MLFS % (95% Confidence Interval) n=20	*P* Value
0.20 (0.19-0.21)	0.14 (0.12-0.16)	0.001

Table 2: Within Normal LVDF measurement of MLFS

LVDF Grade 0 MLFS % (95% Confidence Interval) n=40	LVDF Grade I MLFS % (95% Confidence Interval) n=20	*P* Value
0.22 (0.21-0.22)	0.18 (0.16-0.20)	0.001

Conclusion: This study demonstrates that MLFS is a simple parameter to reliably identify LVDF in patients with preserved LVEF. This study also demonstrates that MLFS measurement in CMR is sensitive enough to detect age-related changes from grades 0 to 1 LVDF. Current methods of assessing LVDF with CMR require time consuming post-processing techniques [3]. In contrast, MLFS can be quickly measured using standard CMR sequences and is a simple means of identifying diastolic dysfunction in patients with preserved systolic function.

References: [1] Vasan R,et al., J Am Coll Cardiol. 1999; 33: 1948–1955. [2] Kurita A, et al., Echocardiography. 2012; 29: 397-402. [3] Karamitsos TD, et al. J Am Coll Cardiol. 2009; 54: 1407-1424.

Diastolic Function Assessed by Cardiac MRI Using Longitudinal Left Ventricular Fractional Shortening

M.N. Dusch[1], S.R. Thadani[1], G.S. Dhillon[1], M.D. Hope[1]
University of California San Francisco, San Francisco, CA

Introduction: Left ventricular diastolic dysfunction (LVDF) is recognized as a significant contributor to morbidity and mortality in congestive heart failure (CHF). Of patients with new onset heart failure, up to 50% have normal left ventricular ejection fractions (LVEF) [1]. Cardiac magnetic resonance imaging (CMR) is a well-established tool to assess systolic dysfunction, but is rarely used to assess LVDF. Midwall longitudinal fractional shortening (MLFS) is a simple parameter shown to correlate with LVDF by echocardiography [2]. Leveraging the superior spatial resolution of CMR, we sought to examine the use of this parameter in the evaluation of LVDF with conventional echocardiography measures serving as a reference.

Methods: The imaging database was reviewed to identify all adult CMR cases with a horizontal long axis (HLA) steady state free precession (SSFP) sequence. Patients were included if they had a transthoracic echocardiogram (TTE) within 6 months of their CMR and LVEF between 55% and 65% by echocardiography. Patients were excluded if they had congenital heart disease, constrictive pericarditis, or a severe valvular defect. LVDF was graded by standard echocardiography criteria as normal (grade 0), impaired relaxation (grade I), pseudonormal (grade III), or restrictive (grade IV). MLFS was determined by calculating the percentage change in the measured distance between the base of the anterior mitral leaflet and the apical endocardium in systole and diastole using SSFP cine sequences in the HLA plane (Figure 1).

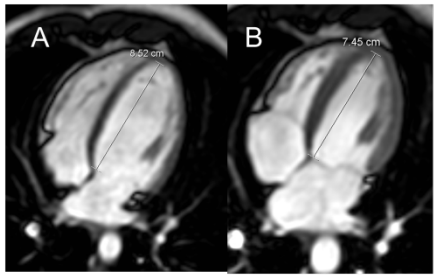

Figure 1: **Sample measurement of MLFS using representative frames from CMR study.** Panel A: Horizontal long axis measurement at end diastole. Panel B: Horizontal long axis measurement at end systole. MLFS calculated from the difference in measurement between Panel A and Panel B.

Results: Following the database review, 80 subjects were identified. LVDF breakdown is as follows: 40 with grade 0, 20 with grade I, 7 with grade III, and 13 with grade IV. The mean MLFS was significantly lower in patients with grade III or IV LVDF compared with grade 0 or I (Table 1). There was also a significant difference between grade 0 and I LVDF (Table 2).

Table 1: Normal vs. Abnormal LVDF measurement of MLFS

LVDF Grade 0/I MLFS % (95% Confidence Interval) n=60	LVDF Grade II/III MLFS % (95% Confidence Interval) n=20	*P* Value
0.20 (0.19-0.21)	0.14 (0.12-0.16)	0.001

Table 2: Within Normal LVDF measurement of MLFS

LVDF Grade 0 MLFS % (95% Confidence Interval) n=40	LVDF Grade I MLFS % (95% Confidence Interval) n=20	*P* Value
0.22 (0.21-0.22)	0.18 (0.16-0.20)	0.001

Conclusion: This study demonstrates that MLFS is a simple parameter to reliably identify LVDF in patients with preserved LVEF. This study also demonstrates that MLFS measurement in CMR is sensitive enough to detect age-related changes from grades 0 to 1 LVDF. Current methods of assessing LVDF with CMR require time consuming post-processing techniques [3]. In contrast, MLFS can be quickly measured using standard CMR sequences and is a simple means of identifying diastolic dysfunction in patients with preserved systolic function.

References: [1] Vasan R,et al., J Am Coll Cardiol. 1999; 33: 1948–1955. [2] Kurita A, et al., Echocardiography. 2012; 29: 397-402. [3] Karamitsos TD, et al. J Am Coll Cardiol. 2009; 54: 1407-1424.

Characterization of Metabolites in Malignant Gliomas Using *Ex vivo* ^{1}H High-Resolution Magic Angle Spinning Spectroscopy

A. Elkhaled[1], L. Jalbert[1], A. Constantin[1], H.A.I. Yoshihara[1], Joanna Phillips[2], A.M. Molinaro[3,4], S.M. Chang[3], and S.J. Nelson[1,5]

[1]Department of Radiology and Biomedical Imaging[2]Department of Pathology, [3]Department of Neurological Surgery, [4]Department of Biostatistics and Epidemiology, [5]Department of Bioengineering and Therapeutic Sciences, University of California - San Francisco

Introduction. Gliomas are routinely graded according to histologic criteria that have been established by the World Health Organization (WHO). Although this classification can be used to understand some of the variance in the clinical outcome of patients, there is still substantial heterogeneity within lesions of the same grade. A further complication in evaluating gliomas is that some undergo malignant transformation to a higher grade, and thereby manifest different pathology upon recurrence. This raises the question of whether a glioma has developed *de novo* at a given grade or transformed from a lower grade lesion that was previously undetected. The primary goal of this study was to use the NMR technique of proton high-resolution magic angle spinning (^{1}H HR-MAS) spectroscopy to characterize metabolic profiles of histologically and etiologically distinct glioma subtypes on the basis of original WHO grades and subsequent transformations.

Methods. This study evaluated image-guided tissue samples acquired from a large cohort of patients presenting with either new or recurrent gliomas of grades II - IV. A total of 126 patients [original WHO grade *N*(II,III,IV=53,23,50)] received a MR exam on a 3T magnet prior to surgery for removal of tumor. Using parameters derived from this exam, putative tumor regions were designated for targeted intra-operative sampling using BrainLab software. 1-4 tissue samples were removed during surgery, with a total of 251 [*M*(II,III,IV=110,40,101)] being collected. Half of the tissue biopsied was analyzed by a pathologist for confirmation of tumor presence and grade; the other half was analyzed via HR-MAS performed on a 500 MHz spectrometer using a CMPG acquisition. Quantification of relative metabolite levels was achieved with HR-QUEST. To assess the association of the metabolite parameters with various pathological grades and inter-grade transitions, we employed a proportional odds logistic regression model adjusted for repeated measures to evaluate the probability of observing given grade outcomes.

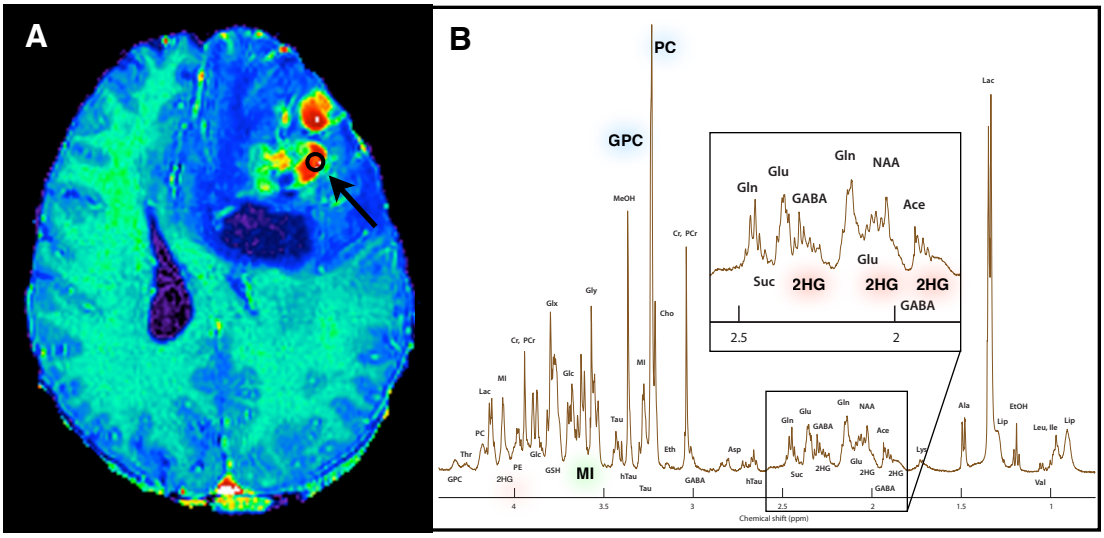

Figure 1. Image-guided target on secondary grade IV glioma (A) and accompanying HR-MAS spectrum showing signature elevation of PC/GPC, 2HG presence, and reduced MI (B).

Results. We found that elevations of the following metabolites and indices were statistically significant($p<0.001$) and characteristic of certain glioma subtypes: myo-intositol/total choline (MCI) in *de novo* and recurrent grade II gliomas; choline-containing species, including free choline and total choline, in *de novo* grade III gliomas and recurrent grade II gliomas that had converted to grades III or IV; phospho-choline/glycero-phosphocholine(PC/GPC) in *de novo* grade IV; and 2-hydroxyglutate(2HG) in *de novo* grade II&III gliomas and recurrent grade II&III gliomas that had converted to grade IV (Fig. 1). The characteristic elevation of PC/GPC in *de novo* GBM suggests that the greatest contribution to the *in vivo* total choline peak comes from PC. Interestingly, metabolic descriptions of histologic malignancy were found to differ across glioma subtypes. These data provide evidence that metabolite levels, some of which can be measured *in vivo*, represent a continuum of intra-grade and intra-lesion malignancy. Such information could be used to enhance the specificity of *in vivo* spectroscopy and aid in the designation of regions of relative therapeutic priority.

Caged boronic acid – [^{18}F]-FDG compounds for pH sensitive PET imaging of tumors

Principal Investigator: Robert Flavell, M.D., Ph.D.
Mentor: David M. Wilson, M.D., Ph.D.

Project Aims: The main goal of this project is to generate novel probes for positron emission tomography (PET) imaging that are targeted towards imaging pathologic processes which result in a local acidic environment, such as cancer. The general principle is to generate a pro-drug derivative of [^{18}F]-FDG that contains a blocking group that would spontaneously decompose upon exposure to acidic conditions. This would result in the local release of [^{18}F]-FDG, which could in turn be taken up by the surrounding tissues (Figure 1). In principle, this class of compounds may be useful in increasing the signal to noise obtained from FDG-PET imaging, which would be of widespread utility in clinical radiology.

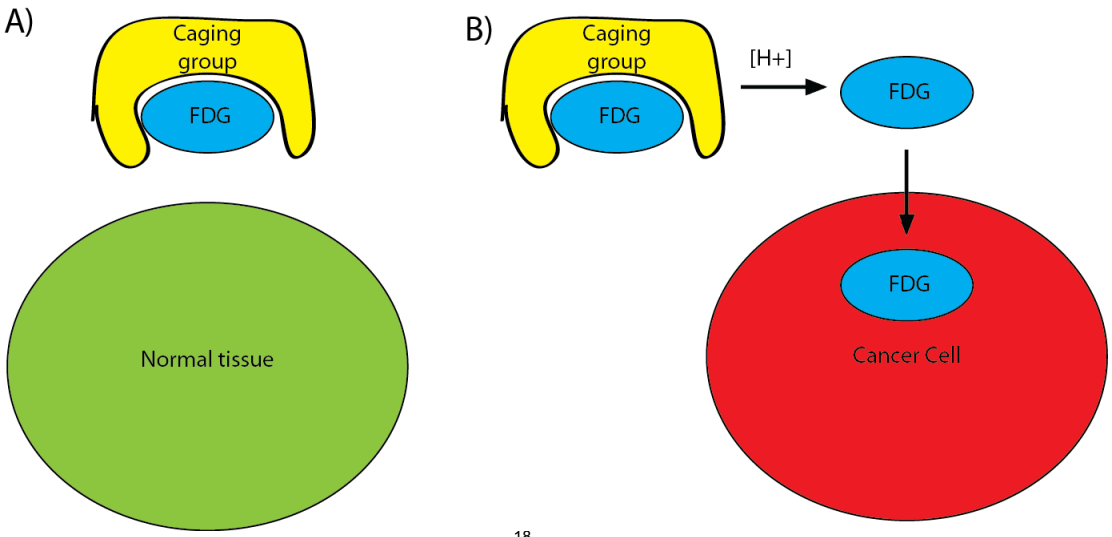

Figure 1. A) Under normal conditions, a caged [^{18}F]-FDG derivative could not be absorbed by tissues. B) Under acidic conditions, such as in a solid tumor, the caged [^{18}F]-FDG derivative would decompose, liberating free [^{18}F]-FDG, which could be absorbed by the adjacent cancer cells.

Specific Aim 1: Develop a small group of caged FDG-derivatives which are pH sensitive over the physiologic range. A small number of compounds based on the following structure will be prepared (Figure 2).

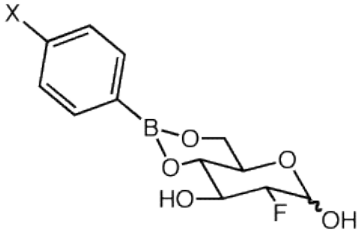

Figure 2. Proposed caged FDG structure. X = variable.

Specific Aim 2: Establish a radiosynthesis of the most promising ^{18}F-FDG derivative. This can be accomplished starting with [^{18}F]-FDG itself in a one step synthesis (see below).

Specific Aim 3: Demonstrate that cells will not take up the ^{18}F-FDG derivative unless acidified. This could be tested in established prostate cancer model cell lines.

Specific Aim 4: Perform biodistribution studies of caged ^{18}F-FDG derivative in animal models of prostate cancer. This could be performed in an animal model that is already widely used at UCSF, such as the transgenic adencarcinoma of the mouse prostate (TRAMP) model.

Previous Work and Background:

Molecular imaging of the acidic tumor microenvironment is an area of active research [1]. Techniques that have been used include magnetic resonance spectroscopy, hyperpolarized ^{13}C magnetic resonance spectroscopy, MR relaxometry, chemical exchange saturation transfer, and optical imaging [2-6]. Positron emission tomography offers the advantages of ready translation to clinical applications, high resolution, and fusion with computed tomography for simultaneous anatomic imaging. Previously, [^{11}C]-dimethyloxazolidinedione (^{11}C-DMO) has been applied to pH sensing in brain tumors [7]. More recently, a radiolabeled peptide, [^{64}Cu]-DOTA-pHLIP, was applied to imaging acidic prostate tumors in animal models [8]. Fluorine-18 is the ideal isotope for most PET imaging applications due to excellent resolution, optimal half life of 110 minutes, and ready availability at medical centers which have an on site cyclotron. Therefore, an ^{18}F-labeled pH sensor would be a promising tracer for imaging of acidic tumors.

Our proposed approach to generate a pH sensitive probe for tumor imaging involves the use of a boronate-caged ^{18}F-FDG pro-drug which would spontaneously decompose to release ^{18}F-FDG upon exposure to acidic conditions. Boronic acids spontaneously and reversibly bind to diols to form esters, and this property has been widely exploited in sugar sensing and in affinity purification of sugars and glycoproteins [9, 10]. The resulting esters are stable at basic pH but readily decompose back to the parent compounds in acidic conditions [11]. Previous studies on the interaction of α−methyl-glucopyranoside with phenylboronic acid demonstrate that the addition of these compounds occurs at the 4 and 6 position of the sugar [12]. Similarly, we anticipate that the addition of phenylboronic acid to 2-fluorodeoxyglucose (FDG) would occur at the 4 and 6 position, and that this ester would readily hydrolyze at acidic pH (Figure 3). Furthermore, by varying the para substituent, the pH sensitivity and stability of the compound could be varied over differing ranges [11]. For example, electron withdrawing substituents such as a nitro group would decrease the pH at which the compound would decompose. Conversely, electron donating substituents such as a methoxy group would increase the pH required for decomposition. Recent data suggest that the extracellular fluid withinextracellular matrix around solid tumors is acidic, and often in the range of 6-7 [1]. Thus, a boronic ester-FDG conjugate that would decompose at pHs below 6.8 or below would likely be optimal for imaging purposes.

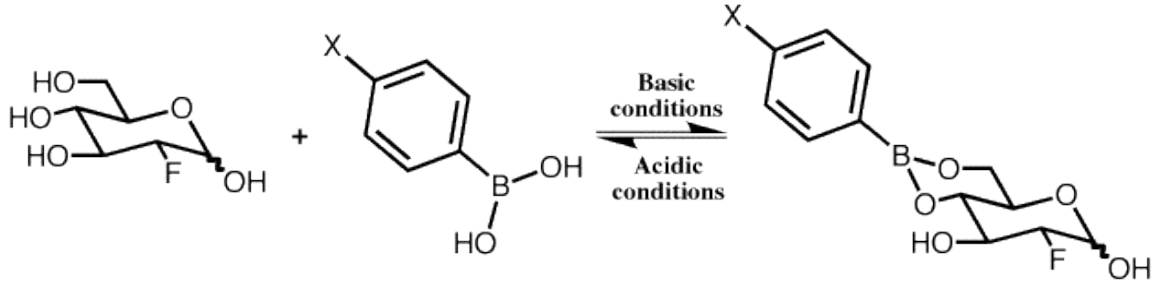

Figure 3. Proposed FDG boronic acid to ester equilibrium. X = variable.

Principal Investigator: Robert Flavell has significant relevant experience from prior research projects during his PhD and internship year. Specifically, he has experience in synthetic chemistry, radiochemistry and micro-PET imaging, and has previously worked on projects both directly on the radiochemistry of 18F-FDG (applications in peptide labeling) as well as in boronic acid chemistry.

Methods and Materials:

1. Synthesis of a small group of caged phenylboronic acid – 2-deoxyglucose derivatives. Initially, we would generate a series of model compounds to investigate the reactivity of phenylboronic esters that are close relatives to the eventual caged ^{18}F-FDG tracer. These model compounds can be synthesized at low cost and are needed to determine structures with the optimum pH sensitivity. 2-deoxyglucose (significantly less expensive than its fluorinated relatives) will be conjugated with various commercially available phenylboronic acid derivatives. Specifically, phenylboronic acid, and para-substituted derivatives including methoxy, nitro, carboxyl, and aminophenyl boronic acid will be used as starting materials. Synthetic methods would be based on previously published procedures, which were applied to the reaction of phenylboronic acid with methyl-glucopyranoside [12]. The identity of the resulting compounds could be assessed using standard techniques including NMR and mass spectrometry.

The stability of these compounds could then be assessed by incubating the resulting compounds in aqueous solution at varying acidity. The rate of decomposition to starting materials could then be determined using high performance liquid chromatography (HPLC). A single lead compound would be identified with optimal stability at pH 7.4 and reasonable rate of decomposition at pH 6.5. We could then synthesize the ^{19}F-FDG derivative of this compound using the optimized methods from the 2-deoxyglucose synthesis. The stability of this structure at varying pH would again be assessed by HPLC, and a sufficient quantity of the compound will be synthesized as a needed standard for subsequent radiosynthesis. Synthesis of the caged phenylboronic acid-FDG model compounds, as well as establishing their stability in aqueous solution will be peformed by Dr. Flavell who has extensive experience with boronate chemistry.

2. Radiosynthesis of an ^{18}F-FDG-boronic acid derivative. One advantage of our method is that the radiosynthesis begins from ^{18}F-FDG, which is readily available at clinical centers that perform PET imaging. The radiosynthesis would be accomplished by direct incubation of ^{18}F-FDG with the appropriate phenylboronic acid derivative under optimized conditions. A purification step would be necessary in order to remove excess contaminating starting materials, likely using HPLC. The compound could then be reformulated in appropriate buffers for injection. Radiochemical purity and specific activity could be obtained using standard methods. These syntheses will be performed by Dr. Flavell, who has experience with small-molecule radiotracers for PET. Dr. VanBrocklin and Joe Blecha will assist in the radiosynthesis.

3. *In vitro* cell assay to demonstrate selective uptake by cells in acidic media. Recently, a perfused cellular or "bioreactor" platform has been developed by Dr.'s Keshari, Kurhanewicz, and VanBrocklin for PET use, modeled closely after designs used successfully for hyperpolarized ^{13}C MRI [13]. A proof-of-principle study demonstrated significant retention of ^{18}F-FDG in encapsulated cells, in a density-specific manner (unpublished data). This system is an ideal way to validate the mechanism of our caged ^{18}F-FDG-boronic acid tracer. Immortalized cancer cells (PC3) will be encapsulated in alginate beads, loaded in the bioreactor, and perfused with media containing the ^{18}F-FDG-boronic acid tracer. Studies will be conducted on the microPET-CT scanner at China Basin. Retention of ^{18}F label by the cells will be compared in the presence and absence of acidic media. In a separate study, ^{18}F-FDG itself will be used. These simple studies will verify the intended mechanism, i.e. that the cells do not accumulate ^{18}F tracer until ^{18}F-FDG is liberated from the caged boronate precursor. Dr. Flavell will take

advantage of ongoing PET-bioreactor studies at UCSF, and testing of the caged FDG-boronate compounds will be performed by Dr.'s Wilson, VanBrocklin, and Keshari who have collaborated extensively on perfused cellular systems.

4. Biodistribution of the ^{18}F-FDG-boronic acid derivative in normal mice and in prostate cancer mice. Micro-PET imaging will be performed following injection of the appropriate caged ^{18}F-FDG compound, both in normal mice as well as in TRAMP mice. Similarly, biodistribution analysis will be performed by sacrificing animals post-injection and then quantitfying the radioactivity in the organs using a scintillation counter. These studies will be performed in accordance with an established (active) IUCAC protocol. Several ^{18}F studies in TRAMP mice using the microPET-CT scanner are currently being performed by Dr.'s Wilson, VanBrocklin, Kurhanewicz and Keshari and adding an additional tracer is trivial.

Significance:

This approach has the potential to dramatically increase the signal-to-noise obtained for detecting acidic tumors using PET. Several tumors (including prostate) have an acidic microenvironment, linked to local invasiveness and metastatic potential [14]. Therefore, this technology could both allow better specificity of cancer diagnosis, and identify tumors with more aggressive features. In addition, the question of tumor pH is of broad interest to researchers in many fields, including basic cancer biology, drug design, and molecular imaging.

The described FDG-boronate compound would represent the first pH sensitive ^{18}F labeled probe for PET imaging. As previously mentioned, the relatively long half-life of ^{18}F makes it an appealing isotope for general clinical use. This would also represent the first example of an ^{18}F-FDG liberating pro-drug, which would represent a significant accomplishment in the field of nuclear medicine, and provide a general platform to synthesize related molecules. In comparison to other PET tracers, the FDG-boronate ester is a remarkably simple, tunable structure.

This project will be an important first step in obtaining extramural grant funding. Specifically, Dr. Flavell intends to obtain a T32 training grant and this preliminary work would provide an important starting point. In addition, Dr. Flavell will soon be eligible for an RSNA grant during fellowship, and continuing his basic science research during residency is key to his pursuit of future NIH funding.

Budget and budget justification

Supplies: We are requesting the following amount for chemicals and chemical supplies (total **$2981.70**). The following materials are requested: 2-Deoxyglucose: $189.00, 5g. (Sigma-Aldrich), Phenylboronic acid: $35.30, 1g (Sigma-Aldrich), 4-Nitrophenylboronic acid: $57.00, 1g (Sigma-Aldrich), 4-Carboxyphenylboronic acid: $33.40, 1g (Sigma-Aldrich), 4-Aminophenylboronic acid: $122.00, 1g (Sigma-Aldrich), 4-Methoxylphenylboronic acid: $27.00, 1g (Sigma-Aldrich). 2-Fluoro-2-deoxyglucose: $524.00, 100 mg (Sigma-Aldrich), Assorted glassware: $500 (Chemglass), HPLC column: Vydac C18 RP-HPLC analytical column; $943.00, TLC plates: $252.00 (Sigma-Aldrich/Merck), Solvents: Approximately $300.

Cyclotron recharge: FDG for this project will be produced in the cyclotron. Each batch (up to 120mCi) will be prepared as needed. It is available on a daily basis with 24 hour notice to the cyclotron staff. The cost for FDG is $115 per 120mCi batch. Batches will be used for optimization of radiochemical synthesis and subsequently for micro-PET imaging. A total of $**1,035** is requested (8 batches at $115/ batch).

Small Animal PET/CT scanner time: The expenses for the microPET studies include use and amortized maintenance of the small animal scanner and support a portion of the imaging technical time. A total of $**1,750** is requested (10 one hour studies at $175/h).

NMR Recharge (Probe characterization). We are requesting **$920.00** for the NMR spectrometer recharge. The recharge for use of the research 11.7T Varian NMR covers a variety of costs, including service charges and supplies. The NMR studies in this project will require approximately 8.0 hours of NMR time at $115/hour.

Murine Procurement/Housing and Care. We are requesting **$3250.00** for costs associated with the procurement, housing, feeding and general care for approximately 10 TRAMP mice. Based on previous murine studies, we estimate an average animal procurement and cage costs to be $325 per mouse. (10 mice x $325/mouse = $3250).

Total budget: **$9936.70**

References:

1. Zhang, X., Y. Lin, and R.J. Gillies, *Tumor pH and its measurement.* Journal of nuclear medicine : official publication, Society of Nuclear Medicine, 2010. 51(8): p. 1167-70.
2. Gillies, R.J. and D.L. Morse, *In vivo magnetic resonance spectroscopy in cancer.* Annual review of biomedical engineering, 2005. 7: p. 287-326.
3. Gallagher, F.A., et al., *Magnetic resonance imaging of pH in vivo using hyperpolarized 13C-labelled bicarbonate.* Nature, 2008. 453(7197): p. 940-3.
4. Garcia-Martin, M.L., et al., *High resolution pH(e) imaging of rat glioma using pH-dependent relaxivity.* Magnetic resonance in medicine : official journal of the Society of Magnetic Resonance in Medicine / Society of Magnetic Resonance in Medicine, 2006. 55(2): p. 309-15.
5. Ward, K.M. and R.S. Balaban, *Determination of pH using water protons and chemical exchange dependent saturation transfer (CEST).* Magnetic resonance in medicine : official journal of the Society of Magnetic Resonance in Medicine / Society of Magnetic Resonance in Medicine, 2000. 44(5): p. 799-802.
6. Hassan, M., et al., *Fluorescence lifetime imaging system for in vivo studies.* Molecular imaging, 2007. 6(4): p. 229-36.
7. Rottenberg, D.A., et al., *In vivo measurement of brain tumor pH using [11C]DMO and positron emission tomography.* Annals of neurology, 1985. 17(1): p. 70-9.
8. Vavere, A.L., et al., *A novel technology for the imaging of acidic prostate tumors by positron emission tomography.* Cancer research, 2009. 69(10): p. 4510-6.
9. Karnati, V.V., et al., *A glucose-selective fluorescence sensor based on boronic acid-diol recognition.* Bioorganic & medicinal chemistry letters, 2002. 12(23): p. 3373-7.
10. Abraham, E.C., R.E. Perry, and M. Stallings, *Application of affinity chromatography for separation and quantitation of glycosylated hemoglobins.* The Journal of laboratory and clinical medicine, 1983. 102(2): p. 187-97.
11. Barker, S.A., et al., *Interaction of Areneboronic Acids with Monosaccharides.* Carbohydrate research, 1973. 26(1): p. 33-40.
12. Ferrier, R.J.H., A.J.; Overend, W.G.; Smith, B.C., *Boric acid derivatives as reagents in carbohydrate chemistry. Part IV. The interaction of phenylboronic acid with hexopyranoid compounds.* Carbohydrate research, 1965. 1: p. 38-43.
13. Keshari, K.R., et al., *Hyperpolarized (13)C spectroscopy and an NMR-compatible bioreactor system for the investigation of real-time cellular metabolism.* Magnetic resonance in medicine : official journal of the Society of Magnetic Resonance in Medicine / Society of Magnetic Resonance in Medicine, 2010. 63(2): p. 322-9.
14. Rofstad, E.K., et al., *Acidic extracellular pH promotes experimental metastasis of human melanoma cells in athymic nude mice.* Cancer research, 2006. 66(13): p. 6699-707.

Molecular Characterization of Inflammation in Mouse Models using Hyperpolarized ^{13}C-Pyruvate

Jeffrey T. Gu BS, Linda Nguyen BS, Gonça Koc MD, John D. MacKenzie MD, and John Kurhanewicz Ph.D
Department of Radiology and Biomedical Imaging, University of California San Francisco

Purpose: To develop the capability of hyperpolarized carbon-13 (^{13}C) imaging at 14-Tesla to study detection and therapeutic strategies in mouse models of inflammation.

Methods: With IACUC approval, inflammation was induced with Freund's complete adjuvant (0.4 mL/kg) in healthy 8 week-old Balb/c mice. At the peak of inflammation (7d post-induction), mice were anesthetized, placed in an agarose gel-holder, and positioned in the NMR scanner. In a separate experiment, mice were treated with a combination of methotrexate (MTX) and etanercept (ETC), or MTX and indomethacin (IND) and observed. Proton (^{1}H) and carbon-13 (^{13}C) imaging was performed on a 14.1-T Varian 600WB animal NMR scanner equipped with 55-mm 100-G/cm gradients and insert volume RF coils for ^{1}H and ^{13}C (L=4 cm, D=4 cm for both). Proton T2W images were obtained with TR=1400 ms, TE=20 ms, slice thickness=1 mm, and FOV=30 x 30 mm through the area of inflammation (paw or soft tissues). ^{13}C spectra (TR=162.76 ms, ESP=13.05 ms, FOV=30 x 30 mm, single 10 mm axial slice) were obtained immediately after the intravenous injection of 300µl of hyperpolarized $^{13}C_1$-pyruvate using DNP (15-20% liquid-state polarization). Tissues were processed and inspected for histological changes of inflammation. Imaging data were processed with VNMRJ and SIVIC imaging software.

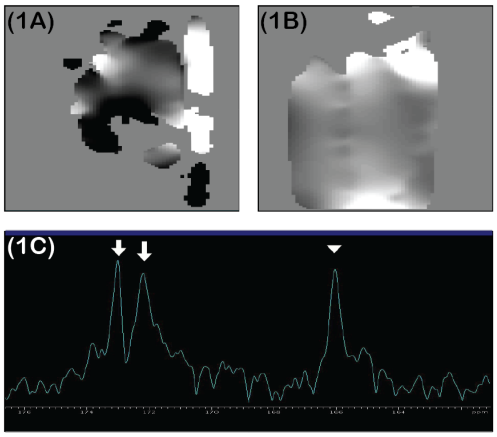

Figure 1

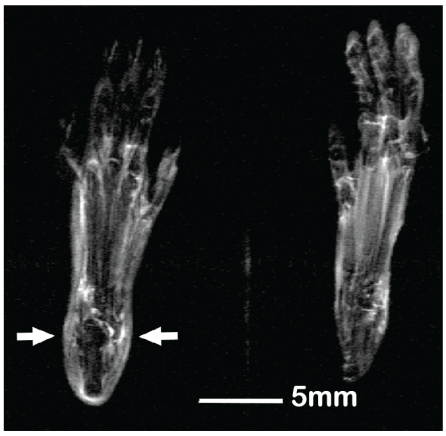

Figure 2

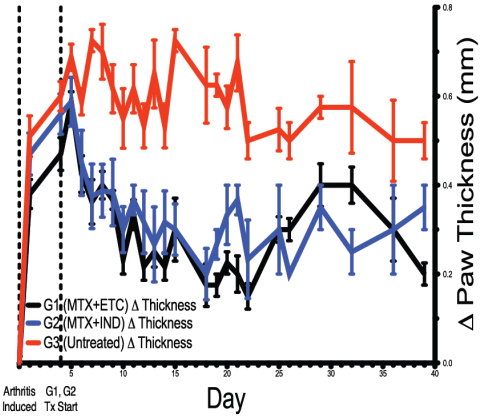

Figure 3

Figure 1: Field map homogeneity of hind paws improves with use of dense agarose gel (Fig 1A without and Fig 1B with gel). (Fig 1C) Spectra obtained at the hind paws shows ^{13}C-pyruvate (arrows) and ^{13}C-urea phantom (arrow head). Figure 2: High-resolution T2W images show swelling in arthritic paw (arrows) vs contralateral control. Figure 3: Treatment response after administration of MTX+ETC, or MTX+IND vs. untreated controls (n=10, for each group).

Results: Field homogeneity improved using agarose gel (1A without, 1B with gel). Hyperpolarized ^{13}C-pyruvate was subsequently detected in hind-paws (1C). This correlates with anatomic T2W imaging (Fig 2) with swelling, edema and increased T2W signal intensity at the inflamed right paw (arrows) vs. the opposite control. Inflammation was confirmed with clinical parameters (Fig 3) and histological changes (data not shown). A mouse model for detecting clinical parameters of treatment response (decreased paw swelling and erythema) has also been developed (Fig 3) for future use and testing with ^{13}C-MRSI.

Discussion: Recently, ^{13}C imaging at 14-T has been established at UCSF, and may be ideal for studying mouse models of inflammation. Our preliminary data suggest that hyperpolarized ^{13}C-pyruvate signal intensity may be detected in areas of inflammation (MacKenzie et al. Radiology. 2011; 259:414-420), and may correlate with high-resolution proton imaging and histological and clinical parameters. Although several technical hurdles remain to observe conversion to ^{13}C-lactate at 14-T, we have achieved key steps (minimizing field inhomogeneity, detection of pyruvate, and selection of an attractive animal model) on the path to testing ^{13}C imaging as a non-invasive measure for monitoring treatment response of inflammation.

Diffusion MRI of Hyperpolarized ^{13}C Metabolites

Bertram L. Koelsch†, Kayvan R. Keshari‡, Tom H. Peeters‡, Peder E. Z. Larson†‡, David M. Wilson‡, John Kurhanewicz†‡
†UC Berkeley – UCSF Graduate Program in Bioengineering ‡Department of Radiology and Biomedical Imaging, UCSF

Introduction: The use of hyperpolarized ^{13}C pyruvate has been shown to be useful in tumor detection and treatment response[1,2]. Recently here at UCSF, a phase I clinical trial showed the potential for using hyperpolarized ^{13}C pyruvate in detecting prostate cancer. In these studies, the excessive production of hyperpolarized ^{13}C lactate is used to differentiate tumorous and normal tissue. However, it is not only hyperpolarized ^{13}C lactate production that can help identify tumors, but the intra- versus extracellular distribution of hyperpolarized ^{13}C lactate could help discern tumor aggressiveness[3]. Larson *et al.* recently developed a super stimulated echo sequence to suppress vascular hyperpolarized ^{13}C signal and thereby allow for more reliable tumor delineation *in vivo*[4]. Extending this technique and creating a diffusion filter could allow for measurement of both the generation of hyperpolarized ^{13}C lactate and its tissue distribution. In this study, we develop a diffusion weighted hyperpolarized MRI pulse sequence that will allow for measurements of the intra- and extracellular distribution of hyperpolarized ^{13}C metabolites.

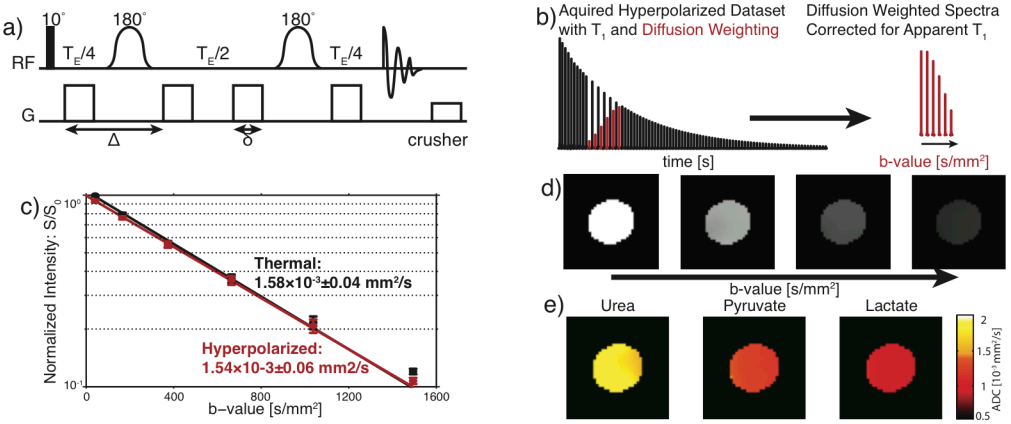

Figure 1. (a) The pulsed gradient double spin echo with a 10° excitation used in all hyperpolarized diffusion weighted acquisitions. (b) The experimental methodology used for concurrently measuring the hyperpolarized molecule's T_1 and its diffusion coefficient. (c) Validation that the diffusion coefficient of measured with hyperpolarized ^{13}C urea matches that of urea at its thermal equilibrium polarization. (d) Representative T_1 corrected diffusion weighted images with increasing b-values (1.7, 173, 693 and 1560 s/mm2) used to generate ADC maps. (e) ADC maps of ^{13}C urea (1.55×10-3±0.07 mm^2/s), ^{13}C pyruvate (1.12×10-3±0.06 mm^2/s) and ^{13}C lactate (0.98×10- 3±0.04 mm^2/s) in solution at 27°C.

Results and Discussion: We implemented a double pulsed gradient spin echo sequence to acquire quantitative hyperpolarized diffusion weighted spectra and images. We have adapted the sequence (**1a**) for diffusion weighting hyperpolarized magnetization by using a small flip angle excitation pulse and a short T_R. The spin echo also refocuses T_2*, which is problematic at higher field strengths. Signal loss is inherent to hyperpolarized experiments due to the inherent T_1 of the nuclei. By concurrently measuring the hyperpolarized metabolite's T_1 (**1b**), we can quantitatively isolate hyperpolarized signal loss solely due to diffusion weighting (**1c**). Using a concentric echo planar imaging readout and a frequency selective excitation, we can simultaneously measure the diffusion coefficients of various hyperpolarized metabolites (**1d** & **1e**).

Prior studies have used diffusion weighting of protons to separate intra- and extracellular signals in an *in vitro* perfusion system[5]. This separation is possible because of the differences in the motional properties of molecules in these two environments. With a similar approach, we will use a bioreactor system developed in-house[6] in combination with diffusion weighting of hyperpolarized metabolites to separate intra- and extracellular signals. This experiment will allow for the simultaneous measurement of membrane transport and intracellular enzymatic conversion. Furthermore, implementation of this hyperpolarized diffusion weighted imaging sequence to measure the *in vivo* tissue distribution of hyperpolarized metabolites in preclinical animal cancer models will follow these *in vitro* bioreactor studies.

Acknowledgments: The authors would like to acknowledge the valuable advice of Mark Van Criekinge, M.S., and Subramaniam Sukumar, Ph.D., as well as support from National Institute of Health grants, K99 EB014328 (KRK), R00 EB012064 (PL), R01 CA166766 (DW) and P41 EB013598 (JK).

References: 1. Albers, M. *et al. Cancer Research* **68**, 8607 (2008). 2. Ward, C. S. *et al. Cancer Research* **70**, 1296–1305 (2010). 3. Ganapathy, V., Thangaraju, M. & Prasad, P. *Pharmacol Therapeut* **121**, 29–40 (2009). 4. Larson, P. E. Z. *et al. IEEE Trans. Med. Imaging* **31**, 265–275. 5. Van Zijl, P. C. *et al. P Natl Acad Sci Usa* **88**, 3228–3232 (1991). 6. Keshari, K. *et al. Magn. Reson. Med.* **63**, 322–329 (2010).

TITLE: Analysis of the Knee Rotational Kinematics in ACL-ruptured Patients Using 3.0 Tesla Magnetic Resonance Image

AUTHORS: Kim, Jong-Min1, 2; Seol, Allen D.1; Wu, Samulel3; Karupppasamy, Subburaj3; Rivoire, Julien3; Li, Xiaojuan3; Ma, C. Benjamin1

INSTITUTIONS: 1. Dept of Orthopaedic Surgery, University of California, San Francisco, San Francisco, CA, United States

2. Dept of Orthopaedic Surgery, University of Ulsan, College of Medicine, Asan Medical Center, Seoul, Korea

3. Musculo-skeletal Quantitative Imaging Research, Dept of Radiology, University of California, San Francisco, San Francisco, CA, United States

ABSTRACT BODY:

Introduction: Anterior cruciate ligament (ACL) rupture affects the knee kinematics and may result in posttraumatic osteoarthritis in the end. Therefore, accurate measurement of rotational instability is important in ACL-ruptured patients. However, quantitative measurement of rotation has been difficult with currently used methods. We developed a rotational loading device to evaluate rotational kinematics of the knee in magnetic resonance image (MRI) machine. We hypothesized that ACL-ruptured knees would demonstrate greater rotational instability than healthy, contralateral knees.

Methods: We prospectively collected 16 patients with unilateral ACL tear. Healthy, contralateral knees served as control. There were 8 men (31.6 ± 6.7 years) and 8 women (33.6 ± 7.8 years). Bilateral knee MRIs were acquired in full extension using 3.0 Tesla MRI machine with an 8-channel phased-array knee coil (Invivo, Orlando, FL, USA). In MRI examination, all patients were placed in a custom device to apply a constant axial load of 44 N and sequential external and internal rotational torque (3.35 Nm). Fast spin echo T2-weighted sagittal images (TR/TE = 4,000/50.96, FOV = 16 cm, 512 X 256 matrix, in-plane resolution of 0.3 mm, slice thickness of 1.5 mm, repetition time of 3,500 ms, and an echo time of 9.7 ms) were acquired in both rotational torque and segmented for rotational calculation using in-house software. We compared rotation arc between ACL-ruptured and control group using paired t-test. This study was approved by the institutional review board in our institution and we obtained informed consent from all subjects.

Results: We chose 4 cases to be segmented by two independent researchers to verify the reliability. The intraclass correlation coefficient (ICC) for rotation arc measurement in two observers was 0.948. Average extension in MRI acquisition was -2.9° ± 3.4° in ACL-ruptured knees and -3.2° ± 2.8° in healthy, contralateral knees with negative value defined as hyperextension. ACL-ruptured knees demonstrated significantly greater arc of rotation compared with control knees (6.8° ± 4.2° vs. 4.9° ± 4.1°, P = 0.026) (Fig 1. Median value with upper and lower quartiles, as well as the range of rotation arc are shown in the graph.). No significant difference was identified between gender of the patients.

Discussion: Evaluations of rotational kinematics in small degrees of knee flexion have been reported in our previous studies. However, rotational kinematics in ACL-ruptured patients in full extension has rarely been evaluated quantitatively with high resolution MRI under rotational torque. MRI proved to be a reproducible method to measure rotational kinematics. Greater rotation arc in ACL-ruptured knees was identified compared to control knees in full extension. We will continue to follow up these patients regularly after operative treatment to perform a longitudinal study.

Significance: Increased rotation in ACL-ruptured knees in full extension indicates different starting point from normal knees during pivot shift phenomenon.

Concentric Rings K-space Trajectory for ^{13}C MRSI

W Jiang, P Larson, M Lustig

UC Berkeley/UCSF Joint Graduate Program in Bioengineering

Keywords: ^{13}C spectroscopic imaging; concentric rings; non-Cartesian sampling; non-uniform reconstruction; phantom scan

Abstract: Echo-planar-based spectroscopic techniques are popular for acceleration in CSI. The spectral bandwidth(SBW) of EPSI is limited by slew rate. System imperfections will induce undesirable ghosting artifacts for EPSI. Concentric rings k-space sampling has advantages of reduced slew rate, acquisition timesaving, and robustness to timing errors, providing a powerful alternative for accelerating MRSI. This method has been applied into fat-water separation MRI[1] and in vivo proton MRSI [2]. The feasibility of concentric rings trajectory and preliminary phantom scan results for ^{13}C MRSI are presented.

Theory: Concentric rings trajectories sample k-space continuously, making the slew rate requirements less than EPSI, given the same prescription. Due to this property, it can provide sufficient SBW. Each ring covers 4 quadrants in spatial k-space, which will halve the total scan time. The symmetric property of the rings makes it robust to timing delays, which only result in rotation of the image. When gridding the data, all the rings are weighted by their k-space velocity, which is proportional to the radius. And its SNR efficiency is a constant of 87%[3][4], compared with currently used ^{13}C EPSI efficiencies of 61% (flyback) and 94% (standard).

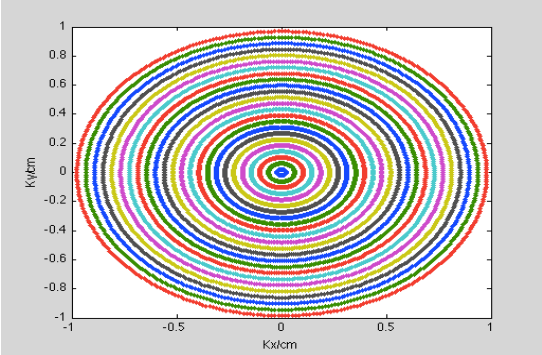

Fig.1. Spatial k-space coverage of all rings

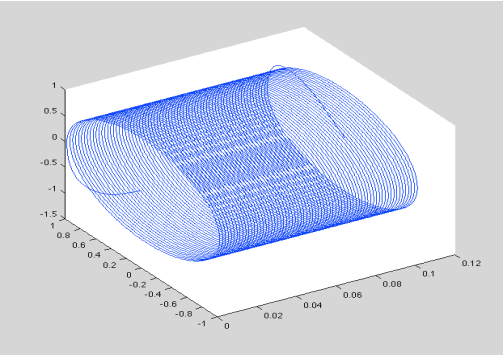

Fig.2. One ring multiply retraced in time for spectroscopic imaging

Method: Gradient waveforms were designed in MATLAB (The Mathworks, Natick MA) using custom software and cvx toolbox. Trajectories were designed for the 5x5 mm^2 spatial resolution, 24x24 cm^2 FOV and 683Hz SBW, 10Hz spectral resolution, as Fig.1,2 shows. The following acquisition parameters were used: TE/TR=0.724ms/2s, 24 phase-encoded excitation, resulting in a total scan time of 48s. The readout gradients were implemented in a GRE pulse sequence on a GE Signa 3T scanner (GE Healthcare Technologies, Waukesha WI). All the data were processed offline using MATLAB and SIVIC software (UCSF, San Francisco, CA). We used 2 syringes full of ^{13}C-urea as our phantoms and used a GE proton phantom for a reference scan.

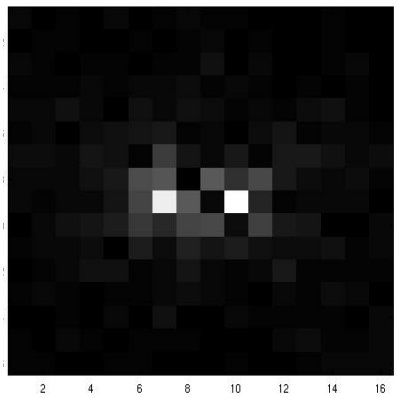

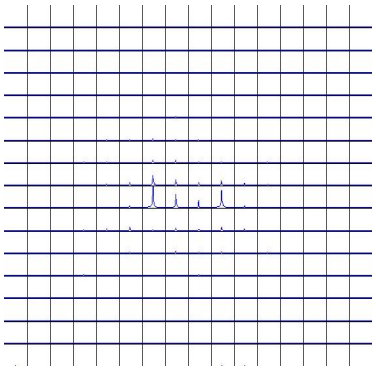

Fig.3. (Left) 2D image for ^{13}C phantom(16*16 grid)
Fig.4.(Right) Spatial-spectral display for the

Result and Discussion: With the ^{13}C phantoms, we used concentric rings sequence to sample the k-space data and NUFFT algorithm [5] for reconstruction. The results are shown in Fig.3, 4. We also used the same sequence to image a GE proton phantom for reference, whose image quality was comparable to a standard GRE sequence, as Fig.5 shows.

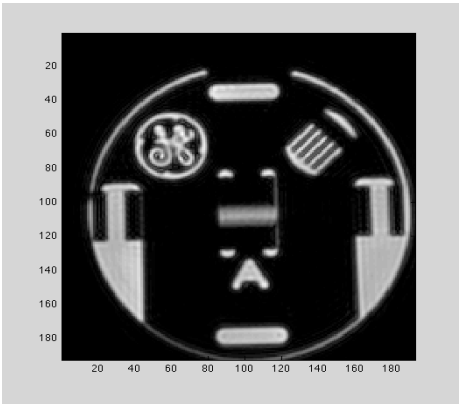

Fig.5. GE proton phantom image using a concentric rings trajectory

Conclusion: Our preliminary phantom scans demonstrated the potential of using concentric rings in ^{13}C MRSI. Currently, we are doing sophisticated comparison phantom scans to evaluate this method. In the future, we can apply this method into Spin Echo or PRESS based sequences to get better SNR and localization. We plan to exploit the sparsity of concentric rings to apply them with compressed sensing as well.

Reference:

[1] Wu. Holden H. [D] Stanford University, 2009. [2] Furuyama J, et al. MRM 2012;67. [3] CH Cunningham, et al. MRM 2005;54:1286-1289. [4] Tsai C, Nishimura D. MRM 2000; 43:452–458. [5] Fessler J, et al. IEEE TRANS 2003:Feb: VOL. 51, NO. 2

Design and Synthesis of Novel Organophosphate Inhibitors as Lead Agents for PET Imaging of Acetylcholinesterase (AChE)

S. James[1], H. VanBrocklin[1], K.S .Ahmed[2], L . Sankaranarayanan[2], C.K .Chao[2], M. Braden[2], J.M. Gerdes[2], C.M. Thompson[2]

[1]Dept of Radiology and Biomedical Imaging, The University of California, San Francisco, CA 94107
[2]Dept of Biomedical and Pharmaceutical Sciences, The University of Montana, Missoula, MT 59812

This project seeks to develop the first *in vivo*, functional assay for organophosphorus (OP) chemical agents. Organophosphate nerve agents are a concern as chemical threats, and as such represent a valuable synthetic target. The development of countermeasures to OP attacks is paramount in order to reduce casualties and minimize impact. However, there are very few functional assays capable of assessing the efficacy of new therapeutics and countermeasures. The purpose of this study is to develop a real-time, functional positron-emission tomography (PET) assay to: (a) test and evaluate the danger of select OP compounds, (b) assess and validate new therapeutics and (c) assess and evaluate existing and new countermeasures.

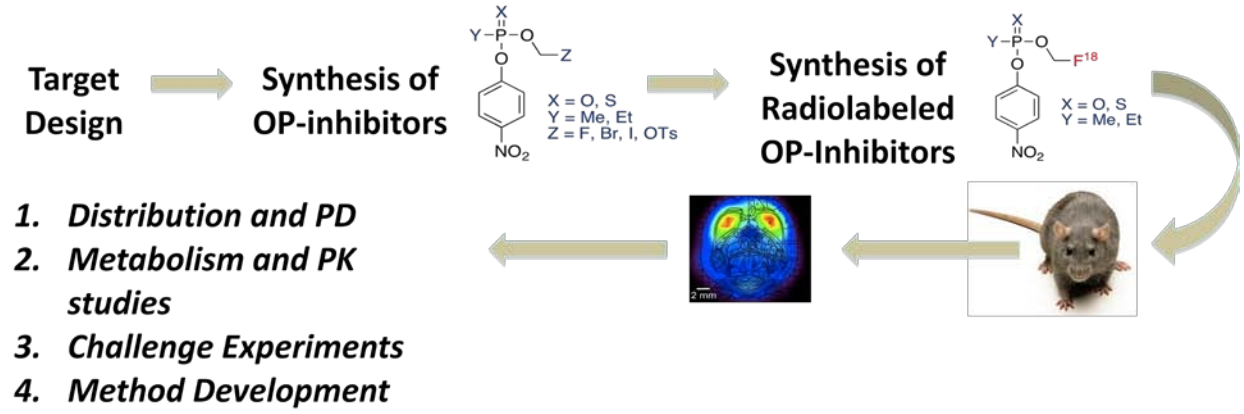

The two major research objectives were accomplished in this project. A radioactive fluorinated *p*-nitrophenoxy OP analog was successfully synthesized and purified. This radiotracer was then injected into normal rats to elucidate the biodistribution and develop a baseline profile. In addition, preliminary challenge scans were done as well, to establish binding specificity of the radiotracer.

MR Parameters are Indicative of Malignant Transformation in Infiltrating Low-grade Gliomas

Llewellyn E. Jalbert, Adam Elkhaled, Joanna J. Phillips, Rupa Parvataneni, Susan M. Chang, Soonmee Cha, and Sarah J. Nelson

Infiltrating gliomas are aggressive tumors of central nervous system that include astrocytomas, oligodendrogliomas, and mixed oligoastrocytomas. The prognosis for these patients can vary significantly depending on the grade of malignancy and histological characteristics, as defined by the World Health Organization (WHO). Although patients diagnosed with low-grade glioma (WHO grade II) generally live much longer than their high-grade counterparts (WHO grades III and IV), there is significant heterogeneity in outcome. Many patients initially diagnosed with low-grade tumors will undergo malignant transformation and upgrade to a higher grade lesion at the time of recurrence. This study aimed to analyze advanced *in vivo* MR imaging and spectroscopy parameters obtained from the pre-surgical examinations of patients previously diagnosed with low-grade gliomas, that were presenting in the clinic with recurrent tumor of varying histological grades of malignancy. We hypothesized the parameters characteristic of higher grade tumors may be indicative of malignant progression in patients with low-grade gliomas. Preoperative MR imaging and spectroscopy was performed on either a 1.5 or 3T GE scanner on 127 patients presenting in the clinic with a recurrent, low grade glioma. In addition to standard anatomical sequences, diffusion weighted imaging (DWI), perfusion weighted imaging (PWI), and spectroscopy imaging (MRSI) was performed. Analysis of metrics describing the volumes and median values of intensities for DWI, MRSI, and PWI data have indicated that there are significant global differences across all three histologic grades of tumor, and between those that underwent malignant transformation to a higher grade (grades III & IV) and those that did not (grade II) (Figure 1.) These parameters may be useful in the routine evaluation of patients with low-grade gliomas, and assessment of malignant transformation in the clinic, so that physicians may make decisions about patient care in a timely manner.

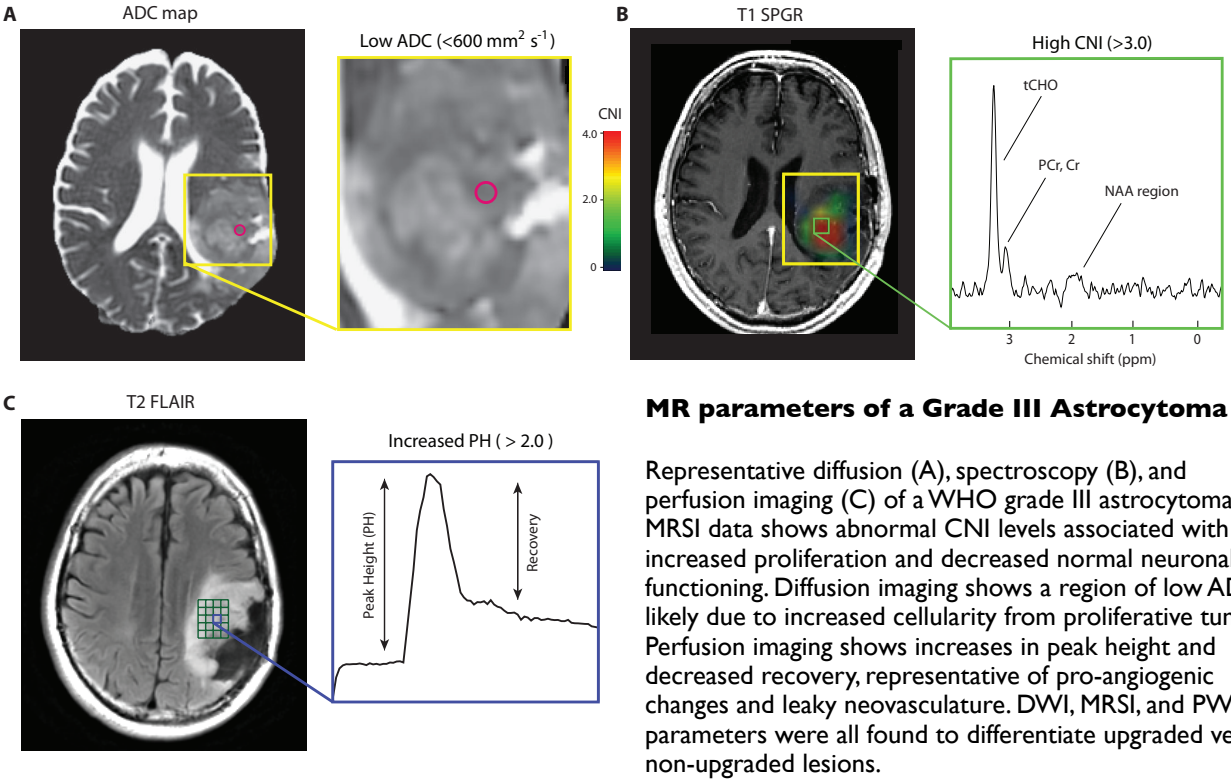

MR parameters of a Grade III Astrocytoma

Representative diffusion (A), spectroscopy (B), and perfusion imaging (C) of a WHO grade III astrocytoma. MRSI data shows abnormal CNI levels associated with increased proliferation and decreased normal neuronal functioning. Diffusion imaging shows a region of low ADC, likely due to increased cellularity from proliferative tumor. Perfusion imaging shows increases in peak height and decreased recovery, representative of pro-angiogenic changes and leaky neovasculature. DWI, MRSI, and PWI parameters were all found to differentiate upgraded versus non-upgraded lesions.

Evaluation of Synovitis and Cartilage Composition Changes after Acute ACL-Injury Using Quantitative MRI

Hoppe, Michael[1]; Wu, Samuel[1]; Rivoire, Julien[1]; Nardo, Lorenzo[1]; Link, Thomas M.[1]Ma, C. Benjamin[2]; Li, Xiaojuan[1];
1.Department of Radiology and Biomedical Imaging, University of California - San Francisco, San Francisco, CA, United States.
2. Department of Orthopaedic Surgery, University of California - San Francisco, San Francisco, CA, United States.

Introduction:

ACL injury can lead to premature osteoarthritis (OA) (1). An increase in inflammatory cytokines, synovial proliferation, and edema in Hoffa's fat pad have been correlated with acute ACL injury (2,3,4). Recent studies suggest inflammation precedes proteoglycan loss and can lead to irreversible collagen loss (3,5). However, no previous studies examined the relationship between synovitis and early cartilage degeneration in acutely injured knees. Understanding this relationship will provide insight on OA development after acute injury, and help identify novel treatment. Our lab has shown elevation of cartilage T1ρ in acute ACL injury (6), indicating early degeneration. The objective here is to evaluate the relationship between synovitis and cartilage T1ρ changes after acute ACL injury using MRI.

Methods:

Thirteen patients with acutely-torn ACL's and having healthy contra-lateral knees were studied at 3T GE HDx MRI scanner using an 8-channel knee coil. A 3D fast spin-echo (CUBE) sequence was used for evaluating synovitis. T1ρ imaging and mapping was performed using the MAPSS sequence developed in our lab. Cartilage was segmented semi-automatically on the CUBE images and rigidly registered to T1ρ-weighted images. Cartilage sub-compartments were defined as in Figure 1. T1ρ differences (ΔT1ρ) were calculated per compartment and sub-compartment with respect to the "healthy knee" per patient. Thickening of the synovial fold, edema, and fluid collection within the surrounding soft tissues were considered synovitis. Hoffa's fat pad was scored separately. Heterogeneity of the fat pad due to edema or increased vascularity and thickening of the surrounding synovial was defined as synovitis. A 2-tailed Student's t-Test was used to compare ΔT1ρ between subjects with and without synovitis.

Results:

Seven of thirteen patients showed synovitis- five also in Hoffa's fat pad. Significantly higher ΔT1ρ were observed between the subjects with and without synovitis in the lateral tibia (LT) and medial tibia (MT), Table 1. These differences were seen in the whole compartment and most sub-compartments for the LT. For the MT, these differences are seen in the whole compartment and the middle sub-compartment (MT-c) only.

Discussion:

Synovitis is observed in 64% of this ACL-injured cohort. This corroborates with previous findings indicating increased inflammation post ACL-injury (2,3,5). The presence of synovitis was correlated with elevated T1ρ values in articular cartilage, suggesting the inflammatory response after ACL injury causes early cartilage matrix changes. Larger cohorts and follow-ups are warranted to investigate the synovitis changes after ACL injury and repair, and explore the possible relationship between synovitis and long-term cartilage degeneration. A better understanding of synovitis and cartilage degeneration will help stratify injuries and identify potential treatment targets (pharmacologic treatment to suppress inflammation for example) for post-traumatic OA after acute injury.

Acknowledgements: The study was supported by NIH P50 AR060752.
References: [1] Lohmander, et al Am J Sports Med 2007. [2] Dahlberg, L et al, Br J Rheumatol 1994;33(12):1107-11. [3]Catterall, JB et al. Arthritis Res Ther 2010..[4] Abreu, MR et al. Skeletal Radiol 2008. [5]El-Gabalawy, H Arthritis Res 1999. [6]Li, X et al, Radiology 2011 258(2):505-14.

Table 1. ΔT1ρ (in ms) in the medial tibia (MT) and lateral tibia (LT).

		ALL MT	MT-a	MT-c	MT-p	All LT	LT-a	LT-c	LT-p
Synovitis	Mean	2.3	1.24	3.07	3.06	3.08	3.04	3.35	4.18
N=7	Std. Dev.	6.53	6.78	7.52	7.21	4.95	5.55	5.28	5.07
No Synovitis	Mean	-4.81	-1.59	-9.15	-1.6	-6.02	-2.53	-6.58	-4.79
N=6	Std. Dev.	2.91	10.59	7.65	5.88	3.31	1.87	4.98	4.55
	p-Value	0.048	0.582	0.02	0.262	0.005	0.059	0.008	0.01

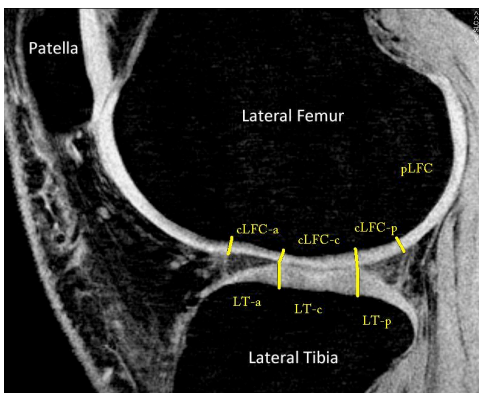

Figure 1. Sub-compartment convention.

Abstract for the 9th Annual Imaging Research Symposium

Title:
Longitudinal increase of T2 relaxation time in normal subjects indicating physiological aging of the collagen network and cartilage matrix - data from the osteoarthritis initiative (OAI)

Authors:
U.R. Heilmeier, P. Beringer, L. Nardo, H. Liebl, S. Lee, G. Joseph, C.E. McCulloch, M.C. Nevitt, T.M. Link

Abstract:
Purpose: To analyze physiological changes of cartilage matrix in healthy subjects using T2 relaxation time measurements over a period of 48 months.

Methods and Material: Right knee 3 Tesla MRI studies of 55 subjects (17 male, 38 female, aged 45 - 60, BMI 23.9 ± 5.7) of the osteoarthritis initiative control cohort were studied at baseline, 2-year and 4-year follow-up. All subjects had no risk factors or radiographic signs of osteoarthritis (OA) at baseline and were free of OA symptoms for the entire examination period. Knee cartilage was segmented and T2 maps were generated in five compartments (patella, medial and lateral femoral condyle, medial and lateral tibial pleateau). Mean T2 relaxation time values and changes over time were measured for each compartment. Statistical analysis was performed using a mixed random effects model accounting for multiple timepoints and adjusted for age, sex and BMI.

Results: All subjects showed significant increases in mean T2 over time (baseline- 24 -48 months) in each compartment (Fig1). The yearly rate of T2 change was highest in the patella (0.78 ms, $p < 0.001$) and lateral femur (0.71 ms, $p < 0.001$). It was lower in the lateral tibia (0.45 ms, $p < 0.001$), medial femur (0.36 ms, $p < 0.001$) and medial tibia (0.50 ms, $p < 0.001$).

Conclusion: Using T2 relaxation time as a sensitive biomarker for cartilage collagen network integrity, this is the first study that radiologically demonstrates over 48 months, that healthy subjects undergo age-related changes in cartilage composition resulting in continuously increasing T2 values over time. These findings need to be considered when evaluating pathologic changes of knee cartilage such as OA.

Figure 1:

T2 changes over time (Baseline, 2-years and 4-years follow-up) measured in the lateral femoral (lf), medial femoral (mf), lateral tibial (lt), medial tibial (mt) and patellar (pat) cartilage knee compartment.

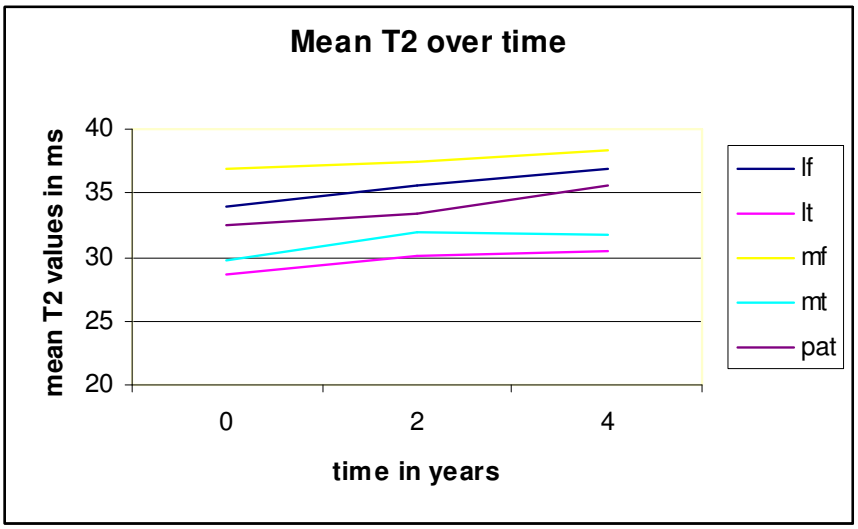

"Rapid Magnetization Prepared Diffusion Weighted Imaging of Articular Cartilage *in-vivo*"

Aditi Guha, Cory Wyatt, Sharmila Majumdar

Musculoskeletal Quantitative Imaging Research, Department of Radiology and Biomedical Imaging, University of California, San Francisco

Diffusion imaging has been primarily focused on brain application with limited applications in the knee. One limitation of diffusion imaging in the knee is the long TE (40-60ms) in most of the sequences that have been used. While this is not a detriment in the brain, it can be a problem in the knee where several tissues have short T2 relaxation times including the cartilage (32ms) and meniscus (11ms). Thus imaging of the knee with a short TE diffusion sequence would substantially increase signal to noise, which would in turn be applied to improve diffusion measurements in meniscus and cartilage. Research has shown that diffusion weighted imaging in knee has a strong potential as a biomarker and can act as a new and potent investigation tool for tissue integrity of meniscus and for early diagnosis of cartilage degeneration. In the past, researchers have proposed new sequences for diffusion weighted imaging but these have largely been proof of concept studies and have not been followed up with in-vivo imaging in patient cohorts, especially at 3T.

A new sequence for diffusion weighted imaging of knee at 3T has been proposed and evaluated. The proposed stimulated echo preparation with MAPSS acquisition sequence is more signal efficient than the conventional spin echo sequence and can image the whole knee volume in half the acquisition time compared to the most commonly used line scan sequence. The proposed sequence has been tested in phantoms, *ex-vivo* specimens and *in-vivo* knees with encouraging results. Further optimization and validation of the sequence is proposed for successful acquisition of diffusion values in knee cartilage and meniscus in healthy volunteers and osteoarthritis patient cohorts.

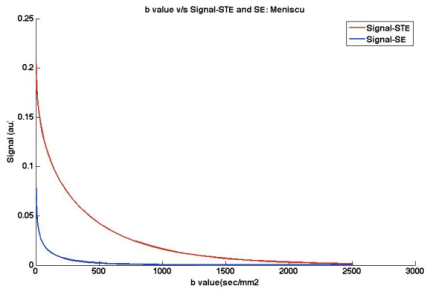

Plot showing signal comparison between the proposed sequence (red line) with the conventional SE sequence (blue line) for meniscus

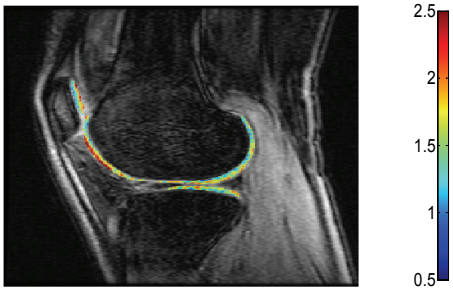

Lateral in-vivo image of a healthy volunteer knee with ADC colormap overlaid.

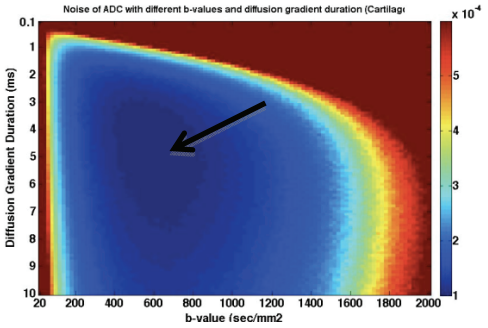

2D colormap showing the noise of ADC measurement with different b-values plotted against the diffusion gradient duration (d) for cartilage. The arrow indicated the region of lowest noise.

	Mean Diffusivity (ADC) value		FA value	
	Mean	**Standard Deviation**	**Mean**	**Standard Deviation**
Medial Femoral	1.43	0.3	0.29	0.11
Medial Tibia	1.53	0.26	0.25	0.09
Lateral Femoral	1.55	0.3	0.28	0.1
Lateral Tibia	1.64	0.29	0.33	0.1
Trochlea	1.69	0.34	0.28	0.08
Patella	1.48	0.36	0.26	0.08

Table showing the mean and standard deviation values of *in-vivo* knee images obtained using proposed sequence.

Project Title: Prospective Randomized Sham-Controlled Study to Evaluate the Safety and Efficacy of a High-Intensity Focused Ultrasound Device for Noninvasive Body Sculpting

Principal Investigators: Maureen P. Kohi, M.D. Viola Rieke, Ph.D., and Sharmila Majumdar, Ph.D.

■ Research Plan

A. Project Aims

Aim 1: To determine the safety of ExAblate Model 2100 system (InSightech Ltd, Tirat Carmel, Israel) for body sculpting.

Aim 2: To determine the efficacy of ExAblate system for body sculpting.

Aim 3: To determine the tolerability of ExAblate system for body sculpting.

B. Previous Work and Background

While several cardiovascular conditioning and muscle toning exercises have been designed and trademarked to shape and tone the human body, over the years multiple medical procedural alternatives have become available. Liposuction is the most common surgical procedure for body sculpting (1) but is an invasive procedure with potential complications. Multiple noninvasive or minimally invasive options for body sculpturing include cryolipolysis, radiofrequency, laser-based, or light-based therapies, injection lipolysis and low-frequency non-thermal ultrasound (2-11). A relatively new treatment for body sculpting is high intensity focused ultrasound (HIFU).

The ExAblate MR guided focused ultrasound is a HIFU system for non-invasive thermal ablation of soft tissue tumors (12-16). First, a series of MR images of the target tissue are obtained and are reviewed by the physician on the ExAblate system workstation. This allows the physician to identify the treatment target volume, delineate the contour of the treatment site on the images and finally review the treatment plan. The specific parameters required to effectively treat the delineated region are calculated by the planning software. Once treatment begins, an ultrasound transducer generates a point of HIFU energy called a sonication. This sonication raises the temperature of the tissue resulting in coagulation necrosis. While the sonication occurs, real-time MR images are acquired to provide quantitative, temperature map of the targeted area. The process of sonication is repeated at multiple adjacent sites to cover the entire delineate treatment volume. The ExAblate system is currently used for the treatment of symptomatic fibroids and painful bony metastatic disease and is being investigated for the treatment of early stage, low risk prostate cancer.

With respect to body sculpting, HIFU generates high-energy sonographic waves (100 to 10,000 W/cm^2), which converge at a specific focal point in the subcutaneous tissue resulting in rapid rise of temperature in the tissue to greater than 65° C resulting in coagulative cell necrosis of adipocytes (17-19). Through this technique, localized destruction of adipose tissue at precise tissue depths can be achieved without damage to the surrounding skin or tissue. Following HIFU treatment, the dead adipose cells induce an inflammatory response attracting macrophages which engulf and transport lipids and cellular debris away from the treatment area. Most of the destroyed adipocytes are resorbed within 12 weeks after treatment and 95% are resorbed after 18 weeks, resulting in overall reduction of local fat volume (20).

Prior studies have demonstrated the safety and efficacy of HIFU in humans (20-22). In a study of 282 patients undergoing a single treatment session of HIFU (lasting 45-60 minutes on average), Fatemi (20) illustrated a decrease in waist circumference by an average of 4.7 cm after 3 months. In an additional study with 85 patients who underwent a single HIFU treatment session Fatemi (21) described an average decrease in waist circumference of 4.6 cm after 3 months. Gadsden et al (22) performed a study with 152 patients who received HIFU. Post treatment ultrasound confirmed that the HIFU effects were limited to the targeted subcutaneous adipose tissue and that the dead adipose cells underwent phagocytosis. In these studies post treatment

complications included edema, dysesthesia, and ecchymosis. No changes in clinical laboratory parameters were noted.

Jewell et al (23) were the first to perform a randomized sham-controlled trial to evaluate the safety and efficacy of HIFU for body sculpting in 180 patients. Using the LipoSonix system (Medicis Technologies Corp., Scottsdale, Ariz.), HIFU was performed at two different energy levels (59-J/cm^2 and 47-J/cm^2). They demonstrated that at total doses of 141 J/cm^2 (three passes at 47 J/cm^2) and 177 J/cm^2 (three passes at 59 J/cm^2) was associated with average reductions in waist circumference of more than 2 cm. Adverse events included mild to moderate discomfort, bruising, and edema. No laboratory abnormalities were noted.

While the reviewed literature is promising, further research is warranted regarding the safety and efficacy of HIFU for body sculpting using the ExAblate System.

C. Methods

Study Design:
We are proposing a pilot prospective randomized sham-controlled study to evaluate the safety and efficacy of HIFU using the ExAblate Model 2100 Type 1.1 System for body sculpting. We intend to recruit 30 patients: 10 in the sham group with intend to treat following 3 months, 10 in the treatment group with low energy dose, and 10 in the treatment group with high energy dose. We intend to follow patients for 3 months after their HIFU session.

Number of Patients and Centers: 30 patients. Single center: UC San Francisco

Population:
Inclusion Criteria

1. Adult female or male patients, age 18 years to 65 years, any race
2. Body mass index less than or equal to 30 kg/m^2
3. Thickness of subcutaneous adipose tissue in the abdomen and flanks greater than or equal to 2.5 cm
4. Ability to give written informed consent

Exclusion Criteria

1. Implanted electrical/metal device preventing MR imaging
2. Scar in the treatment area
3. Skin disease; abnormalities of the skin or soft tissues of the abdominal wall
4. Pregnant/lactating
5. Coagulation disorders
6. Hernias
7. Cancer, cardiovascular disease, diabetes
8. Claustrophobia

Protocol
Study participants will be recruited through advertisement and will be assigned randomly 1:1:1 to receive HIFU at 0 J/cm^2 (three passes; sham group), a “high” total dose (632 J, delivered over a splot length of 4.5 cm, and diameter of 0.5 cm), and a “low” total dose (430 J, delivered over a spot length of 4.5 cm, and diameter of 0.5 cm) to the treatment area defined by the investigators. MR guidance will be ensured to avoid vessels and othe anatomical tissues, and adjustments in spot length, and energy will be made to ensure that J/cm^2. Temperature mapping in fat will be accomplished using a dual flip angle SPGR based technique (Bey, et. al. Mag. Reson. Med, 67, 457-463, 2012). The patients will be asked to not change their diet or exercise routine as to try to control for confounders. On the treatment day, the patient will be positioned on the MR scanner and the HIFU transducer will be placed at the appropriate level to deliver the treatment. Treatment will be limited to the anterior abdomen and flanks. Moderate sedation will be administered during the procedure. Patients will be discharged following the procedure once reaching pre-sedation Modified Aldrete score. Baseline and post treatment waist circumference will be document at 1, 4, 8, and 12 weeks. Complete blood count, markers of

inflammation, basic metabolic, coagulation and lipid panels in addition to renal and liver function tests will be obtained during these times. Patient satisfaction surveys will also be obtained at these times.

Safety endpoints will include adverse events, serious adverse events, and unanticipated adverse device events. A serious adverse event is defined as any event that is life-threatening, resulted in permanent damage or impairment of a body function or structure, or required medical or surgical intervention to avoid such outcomes. Unanticipated adverse device events is defined as any serious effect on health or safety or any life-threatening problem or death caused by or associated with the device, or any other unanticipated serious problem associated with the device that relates to the patient's rights, safety, or welfare (23).

Analysis

Safety will be assessed in all patients. Efficacy will be assessed in the intent-to-treat population and also in a per-protocol population. The per-protocol population will only include patients who will not have major protocol violations, who complete the treatment as planned, and who do not develop conditions that may confound the analysis. Least squares mean changes from baseline waist circumference will be evaluated using analysis of covariance with treatment and study site as fixed effects and baseline waist circumference and weight change from baseline as covariates. By using the least squares mean we attempt to correct for weight changes. Overall patient satisfaction will be assessed based on the surveys provided. Patient discomfort and adverse events will also be documented.

D. Significance

We developed our research proposal in order to assess the safety and efficacy of HIFU using the ExAblate system for body sculpting. While many options exist for body sculpting, HIFU is perhaps the most noninvasive treatment. Once we have data from this pilot study, we intend to perform a larger, potentially multi-center prospective randomized controlled-sham trial to further evaluate the safety and efficacy of HIFU for body sculpting, a new application using this modality.

■ References

1. American Society of Plastic Surgeons. 2011 Report of the 2011 Statistics: National Clearinghouse of Plastic Surgery Statistics. Available at http://www.plasticsurgery.org/news-and-resources/2011-statistics-.html. Accessed July 29, 2012.
2. Avram MM, Harry RS. Cryolipolysis for subcutaneous fat layer reduction. Lasers Surg Med. 2009;41:703–708.
3. 4. Dover J, Burns J, Coleman S, et al. A prospective clinical study of noninvasive cryolipolysis for subcutaneous fat layer reduction: Interim report of available subject data. Lasers Surg Med.2009;41:706.
4. Manuskiatti W, Wachirakaphan C, Lektrakul N, Varothai S. Circumference reduction and cellulite treatment with a Tri-Pollar radiofrequency device: A pilot study. J Eur Acad Dermatol Venereol. 2009;23:820–827.
5. Sadick NS, Mulholland RS. A prospective clinical study to evaluate the efficacy and safety of cellulite treatment using the combination of optical and RF energies for subcutaneous tissue heating. J Cosmet Laser Ther. 2004;6:187–190.
6. Caruso-Davis MK, Guillot TS, Podichetty VK, et al. Efficacy of low-level laser therapy for body contouring and spot fat reduction. Obes Surg 2011;21:722-9.
7. Jackson RF, Dedo DD, Roche GC, Turok DI, Maloney RJ. Low-level laser therapy as a non-invasive approach for body contouring: A randomized, controlled study. Lasers Surg Med. 2009;41:799–809.
8. Khan MH, Victor F, Rao B, Sadick NS. Treatment of cellulite: Part II. Advances and controversies. J Am Acad Dermatol 2010;62:373–384.
9. 10. Matarasso A, Pfeifer TM. Mesotherapy and injection lipolysis. Clin Plast Surg. 2009;36:181–192.

10. Ascher B. Safety and efficacy of UltraShape Contour I treatments to improve the appearance of body contours: Multiple treatments in shorter intervals. Aesthet Surg J. 2010;30:217–224.
11. Moreno-Moraga J, Valero-Alte´s T, Riquelme AM, Isarria-Marcosy MI, de la Torre JR. Body contouring by non-invasive transdermal focused ultrasound. Lasers Surg Med. 2007;39:315–323.
12. Hynynen, K., et al., MR imaging-guided focused ultrasound surgery of fibroadenomas in the breast: a feasibility study. Radiology 2001; 219:176-185.
13. Cline, H.E., et al., Focused US system for MR imaging-guided tumor ablation. Radiology, 1995. 194(3): p. 731-7.
14. Cline, H.E., et al., Magnetic resonance-guided thermal surgery. Magn Reson Med, 1993. 30(1): p. 98-106.
15. Hynynen, K., et al., The feasibility of using MRI to monitor and guide noninvasive ultrasound surgery. Ultrasound Med Biol, 1993. 19(1): p. 91-2.
16. Cline, H.E., et al., MR-guided focused ultrasound surgery. J Comput Assist Tomogr, 1992. 16(6): p. 956-65.
17. Haar GT, Coussios C. High intensity focused ultrasound: physical principles and devices. Int J Hyperthermia 2007;23:89–104.
18. Dubinsky TJ, Cuevas C, Dighe MK, Kolokythas O, Hwang JH. High-intensity focused ultrasound: Current potential and oncologic applications. AJR Am J Roentgenol. 2008;190:191–199.
19. Kennedy JE, Ter Haar GR, Cranston D. High intensity focused ultrasound: Surgery of the future? Br J Radiol. 2003; 76:590–599.
20. Fatemi A. High-intensity focused ultrasound effectively reduces adipose tissue. Semin Cutan Med Surg 2009; 28:257-62.
21. Fatemi A, Kane MA. High-intensity focused ultrasound effectively reduces waist circumference by ablating adipose tissue from the abdomen and flanks: A retrospective case series. Aesthetic Plast Surg. 2010;34:577–582.
22. Gadsden E, Aguilar MT, Smoller BR, Jewell ML. Evaluation of a novel high-intensity focused ultrasound device for ablating subcutaneous adipose tissue for noninvasive body contouring: safety studies in human volunteers. Aesthet Surg J 201;31:401-410.
23. Jewell ML, Baxter RA, Cox SE, et al. Randomized sham-controlled trial to evaluate the safety and effectiveness of a high-intensity focused ultrasound device for noninvasive body sculpting. Plast Reconstr Surg 2011;128:253-62.

■ Budget and Budget Justification

MR Scanner Time

Clinical MR scanner time: 30 scans x $900/scan	$27,000

The scan cost per hour is $450. While the HIFU session lasts for almost 1 hour, pre and post procedural setup time must be considered. As such, a 2 hour time will need to be blocked for each session. Funding is required for 30 patients at a cost of $900 per scan.

Subtotal	**$27,000**

UCSF

Protocol review and IRB fees	$5,000

One-time payment paid for the time and effort put forth by UCSF for regulatory document management and project team initiation/protocol review.

Subtotal	**$5,000**

STATISTICAL ANALYSIS

Statistical analysis: 16 hours x $81/hour	$1,296

The rate for statistician consult is $81 per hour. It is estimated that approximately 16 hours of data analysis and write of the statistical methods is needed. Estimated cost for 16 hours at $81 per hour is $1,296.

Subtotal	**$1,296**
Total	**$33,296**

■ **CHR/IACUC Approval**

This study is pending approval by the committee on human research at our institution.

Reduced FOV Decreases Susceptibility Artifact in Diffusion Tensor MRI for Prostate Cancer Detection

Korn N[1], Kurhanewicz J[1,2], Banerjee, S[3], Noworolski SM[1,2]
[1]Department of Radiology and Biomedical Imaging, University of California, San Francisco
[2]Graduate Group in Bioengineering, University of California, San Francisco and Berkeley
[3]GE Healthcare, Menlo Park, California

Introduction: DTI increases both sensitivity and specificity in detecting prostate cancer in multiparametric MR studies[1]. However, DTI images suffer from high susceptibility artifact near interfaces between air, blood, or fecal matter in the rectum, distorting the peripheral zone of the prostate, where 70% of cancers are located. The aim of this study was to determine if the severity of visually-assessed image distortion is less in prostate ADC maps generated from a novel, reduced FOV diffusion imaging technique[2] than from a standard diffusion sequence and to determine if the ADC contrast between untreated tumors and healthy appearing tissue within subjects is as high as or better than the standard sequence.

Methods: Twenty patients with suspected prostate cancer underwent 3T MRI of the prostate with a fluid-filled endorectal coil for signal enhancement. Standard (STD) (128x128, phase FOV=1, FOV=24, NEX=4) and reduced FOV (rFOV) (128x64, FOV=18-24, phase FOV=.5, NEX=6) diffusion sequences were acquired using an oblique 2D single-shot EPI spin-echo sequence with TR/TE=5000/min, b=600, and 3-4mm slices. The rFOV technique employs a 2D RF pulse which limits the excitation FOV in the phase-encoding direction. This helps shorten the echo-train length for a given resolution, reducing off-resonance effects in the image.

Distortions in the ADC maps can be visualized as changes in the contour of the prostate, particularly in the area of the rectal wall, relative to corresponding fast spin echo T2-weighted images. The incidence and severity of distortion and its improvement were assessed by a side-by-side comparison of ADC maps created from the STD and rFOV diffusion sequences.

ROIs were placed in regions of reduced ADC which corresponded to positive biopsy findings and to radiologist-identified tumor regions (n=14). ROIs were also placed in regions of homogenous, presumably healthy peripheral zone tissue (n=20). Tumor contrast was calculated as: [tumor intensity – healthy tissue intensity]/ healthy tissue intensity. Paired t-tests were performed to assess any significant difference in signal or contrast between the sequences.

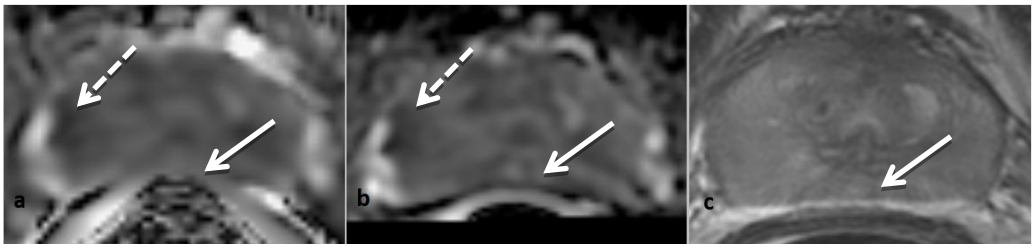

Fig. 1 Arrows denote distorted curvature in the medial peripheral zone on standard ADC(a), less curvature on rFOV(b), and no curvature on the T2-weighted image(c) of a representative patient. Note the reduced ADC in the suspected tumor region (dashed arrow) on both ADC maps.

Results: Ten of the twenty patients scanned showed rectal wall distortion interfering with peripheral zone signal. An example, typical distortion pattern case is shown in Fig 1. Eight of the ten distortion cases showed visibly-decreased distortion in the rFOV sequence. One patient showed severe artifact due to a hip implant, which was not improved by the rFOV sequence.

Discussion: The reduced FOV diffusion sequence yielded decreased rectal wall susceptibility artifact in 80% (8/10) of cases. This sequence provided significantly higher contrast between tumor and healthy tissue. This technique shows great promise for improving diffusion-weighted image quality thereby potentially improving the detection and assessment of prostate cancer volume and grade.

Sequence	Healthy Tissue (n=20)	Tumor (n=14)	Contrast (n=14)
STD	1710 ± 225	971 ± 112	42.9± 0.1
rFOV	1713 ± 235	926 ± 125	45.2± 0.1
Significance	p<0.221	p<0.028	p<0.037

Table 1. Paired t-test results for ADC maps [x10^{-3}mm2/s] and magnitude contrast [%]

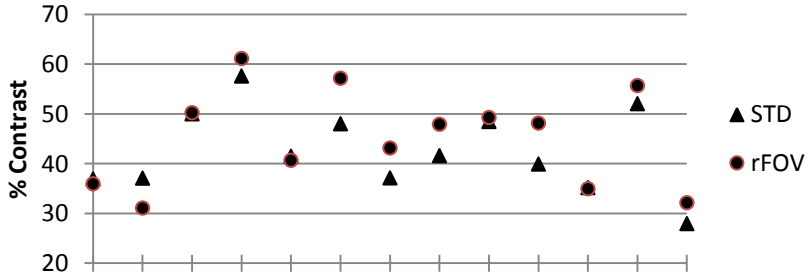

Fig 2. Magnitude contrast of both STD and rFOV sequences represented as a percentage. Each patient is a tick mark on the horizontal axis.

References: 1. Turkbey, B et al. Current Opinion in Urology 2012;(22)4;310-315 2. E.U. Saritas et al, MRM 468-473, 2008

Functional Impairments in Knee Osteoarthritis and Intramuscular Fat Infiltration of Thigh Muscles.

Deepak Kumar, PT, Phd; Dimitrios Karampinos, PhD; Wilson Lin; Toran Macleod, PT, PhD; Lorenzo Nardo, MD; K.Subburaj, PhD; Justin Singh; Thomas M. Link, MD; Sharmila Majumdar, PhD; Richard Souza, PT, PhD

Purpose: To investigate the relationship between quadriceps (Q) and hamstrings (H) lean cross-sectional area (LCSA) and intramuscular (IM) fat with strength, severity of meniscus and cartilage lesions, radiographic osteoarthritis (OA), self-reported and performance based measures of disability.

Subjects: Data from 53 subjects [Age: 53.7 (9.9) years; BMI : 24.3 (3.3) kg/m2], out of 105, have been analyzed to date.

Methods: All subjects had 3-T high resolution MRI for semi-quantitative WORMS grading of meniscus and cartilage lesions and , axial T1-W and IDEAL MRI for quantification of Q and H LCSA and IM fat. KL grading was done on radiographs. Q and H isometric and isokinetic force was measured on a dynamometer. Function was assessed using KOOS, Timed-up and go (TUG) and Stair Climbing Test (SCT). Partial correlations accounting for age and BMI were used to assess relationship of Q and H LCSA and IM fat measures with strength and function. Non-parametric tests were used to assess the relationship of LCSA and IM fat measures with KL and WORMS grades. One-way ANOVA, accounting for age and BMI were used to assess differences in Q and H LCSA, IM fat, strength and function between people with knee OA (KL > 1) and Controls, those with and without posterior horn medial meniscus (PHMM) tears and those with and without cartilage lesions.

Results: After accounting for age and BMI, higher Q and H IMfat were related to worse self-reported and performance measures of function. Q and H LCSA was not related to any functional measures but had strong relationships with all strength measures. Q and H IMfat was also related to strength measures but the relationship was weaker. Thigh muscle LCSA and IMfat measures were not related to KL grades. Greater Q and H IMfat was related to more severe PHMM tears, and patellar and tibial cartilage lesions. There were no difference in thigh muscle LCSA or IMfat, strength and function between people with knee OA and Controls, after accounting for age and BMI. People with PHMM tears had higher Q and H IMfat but no difference in LCSA, strength, TUG or SCT. People with PHMM tears had worse KOOS scores. There were no differences in thigh muscle IMfat or LCSA between those with and without cartilage lesions. There were no differences in strength or functional measures between the groups.

Conclusions: IM fat was related to severity of meniscus and cartilage lesions indicating a possible systemic mechanism of degenerations of knee tissues. Further longitudinal studies need to be done to assess the long term changes in IM fat in this population.

Clinical Relevance: Thigh muscle IM fat is more significantly related to self-reported disability and functional performance than LCSA indicating that IM fat has an important role in disease pathogenesis. Clinicians need to consider the role of muscle compositional change while managing patients with knee meniscus tears, cartilage lesions and osteoarthritis.

Analysis of pre- and post-radiotherapy MRSI in patients with newly-diagnosed GBM to predict outcome

Yan Li, MD, PhD,[1] Janine M. Lupo, PhD,[1] Rupa Parvataneni, MS,[2] Kathleen R. Lamborn, PhD,[2] Soonmee Cha, MD,[1] Susan M. Chang, MD,[2] and Sarah J. Nelson, PhD[1,3]

[1]Department of Radiology and Biomedical Imaging, University of California, San Francisco, CA 94158, United States
[2]Department of Neurological Surgery, University of California, San Francisco, CA 94158, United States
[3]Department of Bioengineering & Therapeutic Sciences, University of California, San Francisco, CA 94158, United States

Glioblastoma (GBM) is the most common and malignant type of glioma. Despite the advances in multimodality treatments, patients with GBM have a limited prognosis, with a median survival of 15 months. Conventional MRI is a powerful tool for delineating structural abnormalities in gliomas such as areas where the brain-blood barrier (BBB) has been compromised, but is not a direct reflection of changes in tumor biology. 3D 1-H MRSI provides parameters for estimating tissue function and may therefore contribute to the prediction of outcome. In this study, we assessed the predictive values of MRSI parameters at the time of pretreatment (pre-RT, baseline) and a follow-up 2 months later (F2mo, post-RT) in relationship to 6-month progression-free survival (PFS-6) and overall survival (OS) in the 64 patients with newly-diagnosed GBM being treated with RT and concurrent chemotherapy (81%, temozolomide). Evaluated were metabolite indices and metabolite ratios. Logistic linear regression and Cox proportional hazards models were utilized to evaluate metabolite parameters on PFS-6 and OS, respectively. Stepwise regression was then performed on the significant variables. Decreased ratio of N-acetyl aspartate to choline containing compounds to (NAA/Cho) in the CNI3 (Cho to NAA index >3) at the baseline, as well as elevated CNI in the CNI2 (CNI>2), CNI3, or CNI2T (within T2 lesion having CNI>2) at the F2mo was associated with shorter PFS-6. Patients with elevated lipid and lactate values at the baseline, F2mo or from pre-RT to post-RT, had significantly worse OS. The number of voxels within the CNI2 or CNI2T at the F2mo was correlated with PFS-6 and OS, respectively, while the anatomic volumes were only associated with OS. Our studies indicate that 3D MRSI parameters are important for predicting PFS-6 and OS for patients with GBM.

Cartilage T2 relaxation time measurements predict progression of Osteoarthritis assessed with KL score - Data from the Osteoarthritis Initiative

Authors: H. Liebl, N. Singh, G. Joseph, L. Nardo, J. Lynch, C.E. McCulloch, M.C. Nevitt, T.M. Link

Purpose: To evaluate the performance of T2 relaxation time measurements in predicting the onset of osteoarthritis (OA).

Methods and Materials: Three Tesla MRIs were performed in 100 individuals with no radiological signs of OA (Kellgren-Lawrence (KL) Score 0 or 1). Fifty individuals with KL scores of 0 or 1 at baseline which showed progression to OA with an increase of KL Score of ≥ 2 over 4 years were compared to 50 individuals with KL Scores of 0 or 1 at baseline which showed no change in KL scores. T2 relaxation time measurements were all performed at baseline. Five knee cartilage compartments were analyzed (patella, lateral and medial for both femur and tibia). The progression cohort was subdivided into a mild progression (KL increase of 2 over 4 years) and accelerated progression group (KL increase of 3 or more over 4 years). Statistical analysis was performed using ANOVA and student's t-test.

Results: Individuals with progression to OA showed higher baseline T2 relaxation time measurements in all compartments than the controls, but statistical significance was only reached in the patella (control versus mild progression, P = 0.0014; control versus severe progression, P = 0.0079). The accelerated progression group showed the highest mean global baseline T2 measurement (Mean ± SEM, 47.3 ± 0.9 ms) compared to the mild progression group (46.8 ± 0.6 ms) and the controls without progression (45.9 ± 0.4 ms). The highest baseline values were found in the accelerated progression group at the patella (50.1 ± 1.5 ms) and the medial femoral compartment (55.2 ± 1.5 ms), where morphological cartilage lesions in OA are typically found.

Conclusions: Baseline T2 measurements were elevated in individuals that progressed to knee OA (KL ≥ 2) over 4 years compared to controls that showed no progression. Baseline T2 relaxation time measurements also predicted the degree of progression and therefore may potentially allow to predict manifestation of radiological OA, at stages where focal morphological change may not be visualized.

Simulations of Multi-Shot Spiral Imaging with Off-Resonance Correction and Variable Density k-Space Sampling

Hui Liu, Norbert Schuff, Gerald Matson

[1] Center for Imaging of Neurodegenerative Diseases, SFVAMC, CA, [2]University of California at San Francisco, CA, [3]NCIRE, San Francisco, CA.

Introduction: Multi-shot spiral imaging has the advantages of efficient use of the gradient performance of the system, and inherently suppresses flow and motion artifacts. Acquisition speed can be further enhanced by variable density spirals which under-sample the outer k-space regions [1]. However, spiral acquisitions are more sensitive to off-resonance artifacts than Cartesian acquisitions, and the relatively intensive computation required for reconstruction has hindered applications of spiral imaging. Recently, Meng et al [2] demonstrated an efficient reconstruction method using constant density spiral sampling that included off-resonance (OR) correction with significantly improved computation efficiency. In this work, we use simulations to show that their approach can be applied to variable density spiral sampling in order to further reduce the acquisition time. Our numerical simulations show computation-efficient image reconstruction results exhibiting high fidelity of image quality with minimal under-sampling artifacts.

Methods: Meng 's approach formulates the conversion from spiral to Cartesian k-space as [2]:

$$\mathbf{T} \cdot \mathbf{S}_{\mathbf{Cartesian}} = \mathbf{S}_{\mathbf{spiral}} \qquad (1)$$

where $\mathbf{S}_{\mathbf{Cartesian}}$ has been corrected for off-resonance artifacts. This approach avoids the need for point density calculations and corrections for the filter used, and also lessens the need for oversampling. In addition, $\mathbf{S}_{\mathbf{Cartesian}}$ vector on the left-hand side would represent the image, the T matrix in this case is sparse, which greatly facilitates the calculations. We first developed our spiral k-space trajectory which featured uniform spiral sampling at inner k-space but transitioned to variable density sampling [3] for outer k-space regions. It also incorporated the correction [4] to avoid gradient and slew rate violations in the k-space center and the transition to variable density sampling. Second, we simulated the spiral k-space with options of adding off-resonance effects and Gaussian noise, and also options for k-space filtering and image over-sampling. Finally, we implanted off-resonance correction and reconstructed the image by 2DFFT. A Shepp-Logan phantom was used to evaluate the accuracy of the proposed method. The computer algorithms were written in Matlab and incorporated GUI interfaces to facilitate usage.

Results and Discussion: Figure 1 shows a single-arm spiral k-space trajectory (red represents the slew-rate limited regime, blue and green are gradient limited regimes, where green is the variable density region). Fig. 2 shows a simulated off-resonance (OR) map. Figure 3 shows the reconstructed image without off-resonance correction, while Fig. 4 shows the off-resonance corrected reconstructed image. For this case, a conjugate gradient algorithm was used to solve equation 1. However, we will discuss other methods for solving equation 1.

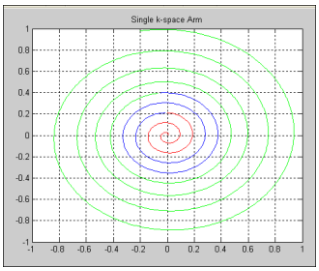

Fig. 1.Single-arm k-space trajectory.

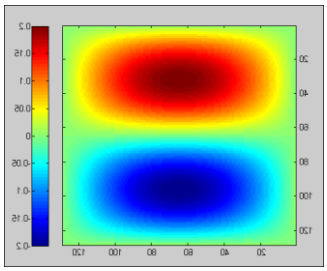

Fig. 2. Off-resonance map.

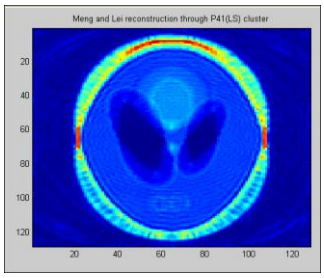

Fig. 3. Reconstructed image without OR correction.

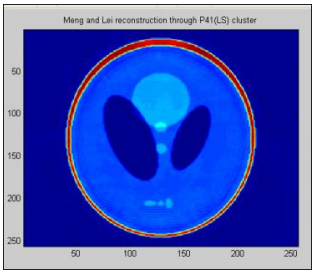

Fig. 4. Reconstructed image with OR correction.

Conclusions: Our results show that the Meng et al method can efficiently and accurately reconstruct the image with off-resonance correction even with variable density spiral acquisition which under-samples the outer k-space regions. Future work will include further investigation of reconstruction methods, including methods used for compressed sensing.

References: 1. MRM 65, p1287, 2011 2. MRM 63, p1691, 2010 3. MRM 50, p214, 2003. 4. ISMRM abstract 1342, 2008.

Multi-Shot Spiral MPRAGE Imaging with Off-Resonance Correction

Hui Liu, Norbert Schuff

[1] Center for Imaging of Neurodegenerative Diseases, SFVAMC, CA, [2]University of California at San Francisco, CA, [3]NCIRE, San Francisco, CA.

Introduction: Multi-shot spiral imaging has the advantages of fast acquisition, efficient use of the gradient performance of the system, and inherently suppresses flow and motion artifacts. However, spiral acquisitions are more sensitive to off-resonance artifacts than Cartesian acquisitions, and the relatively intensive computation required for reconstruction has hindered the widely applications of spiral imaging. Recently, Wei et al [1] demonstrated an efficient off-resonance correction method called ORACLE with significantly improved computation efficiency. In this work, we applied this approach to correct spiral MPRAGE image. Our results showed that this computation-efficient image reconstruction result exhibits high fidelity of image quality with corrected off-resonance artifacts.

Methods:

The acquired multi-shot k-space data is segmented into multiple segments (fig3) based on their acquisition times. The field map was obtained from gradient echo dual echo mapping sequence. Acquired spiral data was regridded onto the Cartesian grid. A convolution with the kernels was then carried out to derive artifact-free data for each Cartesian grid point. When the entire k-space is corrected, a fast Fourier transform is taken to reconstruct the artifact-free image. An ADNI phantom was used to evaluate the accuracy of the proposed method. The experiment was performed at 3T Siemens Skyra MRI system. The customized computation algorithms were written in Matlab. Spiral MPRAGE image parameters are as follows: TR=3s, average = 1, Image size is 268 x 268, FOV=256mm, 48 spiral arms, 590 samples, dwell time is 3.83μs. Image raw data(K-space data) were acquired for off-resonance correction. Total acquisition time is 5.5 second.

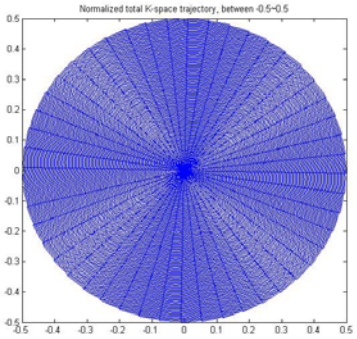

Fig.1. 48-arms k-space

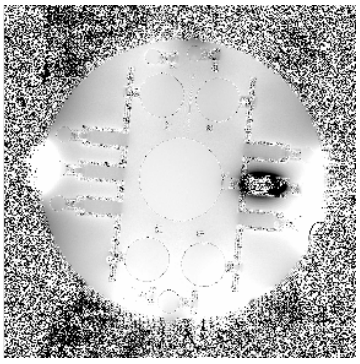

Fig. 2. Off-resonance map

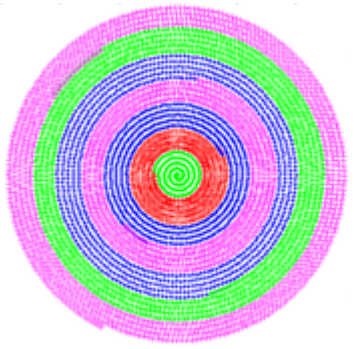

Fig3. Segmented k-space

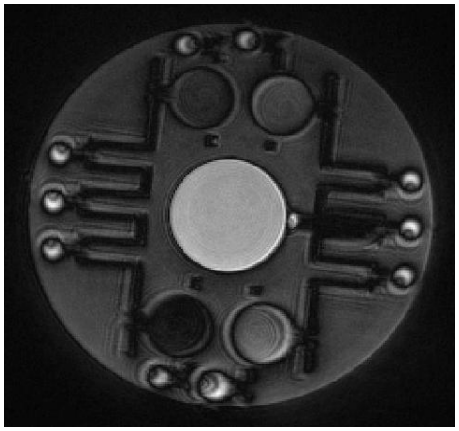

Fig. 3. Off-Resonance un-corrected

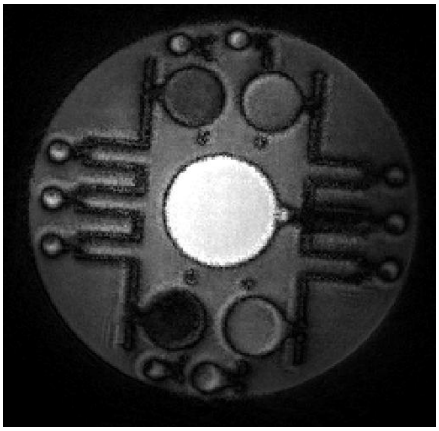

Fig. 4. Off-resonance corrected

Results and Discussion: Fig.1 shows a 48-arm spiral k-space trajectory. Fig.2 shows the off-resonancemap. Fig. 3 shows the segmented k-space. Fig.4 shows the reconstructed image without off-resonance correction, while Fig. 5 shows the off-resonance corrected image. The off-resonance corrected image still shows some bright edges artifacts, which might be caused by imperfection of gradient system. Further corrections such as gradient delay, k-space spiral trajectory correction, eddy-current and concomitant field caused artifacts are under development.

Conclusions: Our results show that this ORACLE method can efficiently and accurately reconstruct the image with off-resonance correction. Future work will include further investigation of correction of imperfect gradient system, variable density sampling and corresponding reconstruction methods, including methods used for compressed sensing.

References: 1.Wei Lin et al, MRM 2011

CIRcular Cartesian UnderSampling (CIRCUS) with a Golden Ratio Profile: A Variable Density 3D Cartesian Sampling Strategy for Compressed Sensing and Parallel Imaging

Jing Liu, David Saloner

University of California San Francisco, San Francisco, CA

Introduction: Compressed sensing (CS) and parallel imaging (PI) methods have been exploited to significantly reduce scan time, which is highly desirable for 3D/4D imaging applications that usually involve unreasonable long scan times. To recover MR images from undersampled data, random sampling is desired for CS. In practice, non-Cartesian trajectories (such as spiral, radial), or Cartesian sampling patterns (such as spiral-like, radial-like, random, Poisson-disk) have been investigated for undersampling along k_y-k_z plane in 3D imaging scans. Poisson-disk sampling (PDS) provides even but random distribution of samples, which is well suitable for CS&PI [1]. Variable-density PDS (vPDS) can even further improve image reconstruction. However, the computational cost required for this algorithm is high and makes it impractical. This study proposed a method for generating undersampling patterns for 3D Cartesian acquisition, providing high flexibilities of designing sampling patterns, which include radial, spiral as well as pseudo-random sampling patterns. This proposed method is easy to implement, flexible to adjust the sampling trajectories and ordering. It provides high accuracy of image reconstruction with CS&PI. It also allows flexible interleaving schemes for dynamic imaging.

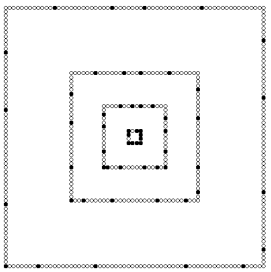

Fig. 1. Circular undersampling

Methods: To undersample the k-space, only a portion of the points will be acquired. To decide the locations of the points to sample and the sampling order to follow, we introduce our CIRcular Cartesian UnderSampling (CIRCUS) method. The 3D k-space sampling matrix N×N on k_y-k_z plane is divided into N/2 square frames of different sizes, ranging from 2×2 to N×N (Fig.1, four representative frames are shown). Our sampling pattern design is based on circular sampling along the edges of the square frames.

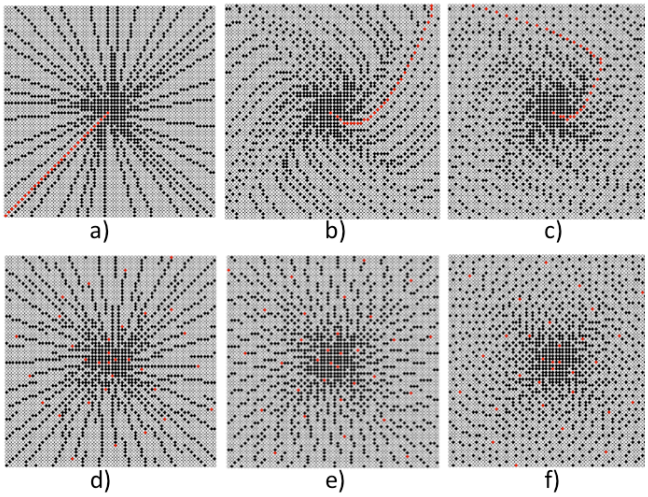

Fig. 2. k_y-k_z plane. a) Circular undersampling at each frame starts from the same position (left bottom corner), b-f) starting points with linear and nonlinear shifts at each frame.

The idea is to select the indexes of the sampling points along the edges of the square frame by skipping a certain number of points based on a golden ratio profile [2] (Fig.1, solid dots are selected for sampling). By introducing either linear or nonlinear shifts to the starting points of the square frames, we can flexibly design the sampling patterns to be spiral, radial, randomized spiral /radial (Fig.2). A few representative sampling patterns obtained with CIRCUS method are shown in Fig. 2, where read dots denote the starting points of circular sampling at each square frame.

Results and Discussion: Fig.3 shows different undersampling patterns (R=8) and their corresponding images reconstructed with SPIRIT & L_1-norm Wavelet regularization [3]. It has been demonstrated that variable density sampling significantly outperforms the uniform random sampling. Results obtained with CIRCUS are all similar to that obtained with vPDS, although radial and spiral samplings have slight higher reconstruction errors.

Conclusion: This study propose a novel method for generating undersampling patterns for 3D Cartesian imaging with CS&PI reconstruction.

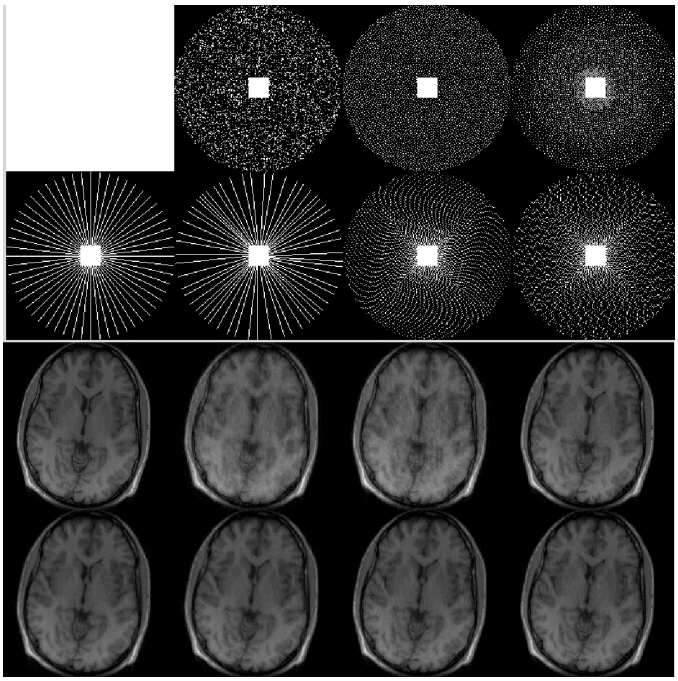

Fig. 3 k-space sampling patterns and corresponding reconstructed images. Top row: full; uniform random; PDS; vPDS; Bottom row (CIRCUS): uniform radial; radial with golden ratio profile; randomized spiral/radial. R=8.

References: 1. Lustig M, et al. MRM 2007;58, p1182. **2**. Winkelmann S, et. al., IEEE-TMI, 26, p68. **3**. Lustig M, et al. MRM 2010; 64, p457.

MR Parameters are Indicative of Malignant Transformation in Infiltrating Low-grade Gliomas

Llewellyn E. Jalbert, Adam Elkhaled, Joanna J. Phillips, Rupa Parvataneni, Susan M. Chang, Soonmee Cha, and Sarah J. Nelson

Infiltrating gliomas are aggressive tumors of central nervous system that include astrocytomas, oligodendrogliomas, and mixed oligoastrocytomas. The prognosis for these patients can vary significantly depending on the grade of malignancy and histological characteristics, as defined by the World Health Organization (WHO). Although patients diagnosed with low-grade glioma (WHO grade II) generally live much longer than their high-grade counterparts (WHO grades III and IV), there is significant heterogeneity in outcome. Many patients initially diagnosed with low-grade tumors will undergo malignant transformation and upgrade to a higher grade lesion at the time of recurrence. This study aimed to analyze advanced *in vivo* MR imaging and spectroscopy parameters obtained from the pre-surgical examinations of patients previously diagnosed with low-grade gliomas, that were presenting in the clinic with recurrent tumor of varying histological grades of malignancy. We hypothesized the parameters characteristic of higher grade tumors may be indicative of malignant progression in patients with low-grade gliomas. Preoperative MR imaging and spectroscopy was performed on either a 1.5 or 3T GE scanner on 127 patients presenting in the clinic with a recurrent, low grade glioma. In addition to standard anatomical sequences, diffusion weighted imaging (DWI), perfusion weighted imaging (PWI), and spectroscopy imaging (MRSI) was performed. Analysis of metrics describing the volumes and median values of intensities for DWI, MRSI, and PWI data have indicated that there are significant global differences across all three histologic grades of tumor, and between those that underwent malignant transformation to a higher grade (grades III & IV) and those that did not (grade II) (Figure 1.) These parameters may be useful in the routine evaluation of patients with low-grade gliomas, and assessment of malignant transformation in the clinic, so that physicians may make decisions about patient care in a timely manner.

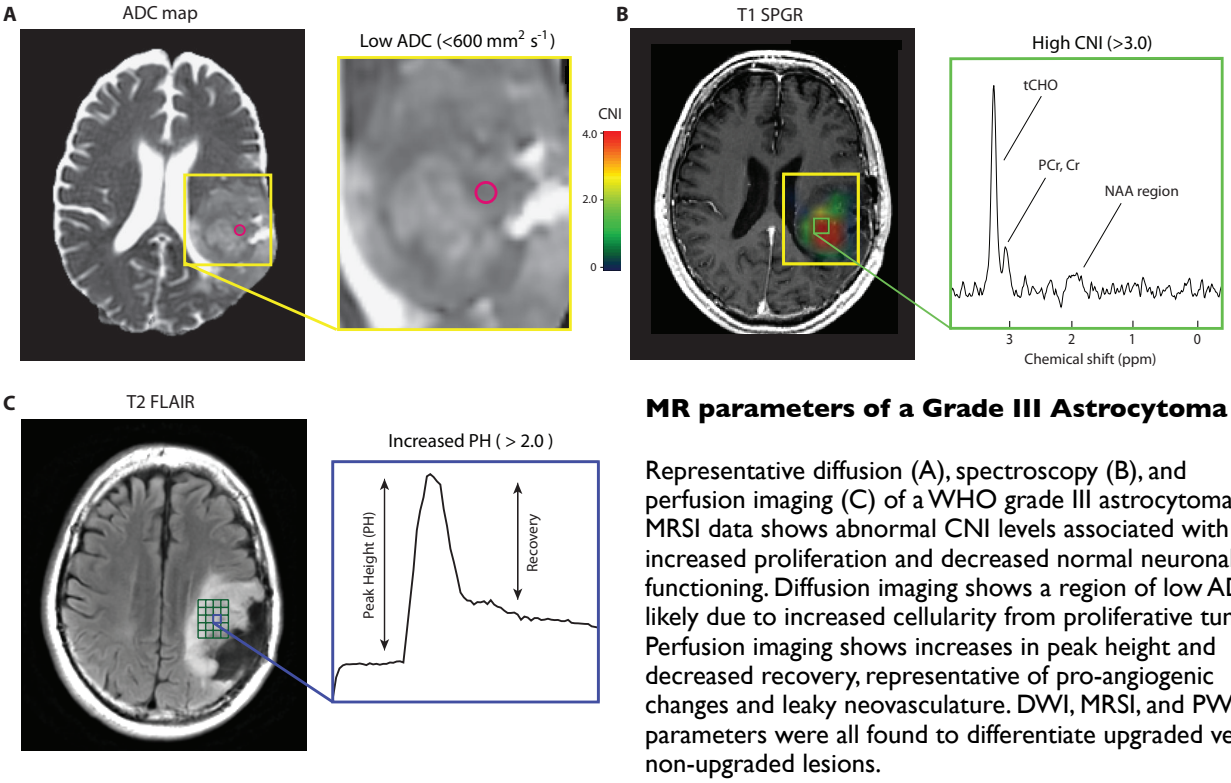

MR parameters of a Grade III Astrocytoma

Representative diffusion (A), spectroscopy (B), and perfusion imaging (C) of a WHO grade III astrocytoma. MRSI data shows abnormal CNI levels associated with increased proliferation and decreased normal neuronal functioning. Diffusion imaging shows a region of low ADC, likely due to increased cellularity from proliferative tumor. Perfusion imaging shows increases in peak height and decreased recovery, representative of pro-angiogenic changes and leaky neovasculature. DWI, MRSI, and PWI parameters were all found to differentiate upgraded versus non-upgraded lesions.

Development of a Novel Vascular Phantom for Navigation Testing in Interventional MRI

Aaron D Losey, Alastair J Martin, Prasheel Lillaney, Anand S Patel, Ryan S Sincic, Curtis J Caton, Erin Yee, Bradford Thorne, Mark W Wilson, Steven W Hetts

Introduction: Interventional MRI is an emerging field that offers unique capabilities, such as the ability to steer catheters by creating a magnetic field near the catheter tip. Efficacy of MR guided navigation must be tested *in vitro* in vascular phantoms that mimic the *in vivo* environment. Previous vascular phantoms have shortcomings including lack of MRI compatibility, artifact creation, non-physiologic stiffness, and high frictional resistance that limits navigation capabilities. We sought to develop a vascular phantom from poly(vinyl) alcohol cryogel (PVA-C) that overcomes these limitations and provides a tool to test our magnetically-assisted remote control (MARC) endovascular catheter for interventional MRI.

Methods and Materials:
Design Considerations: Design considerations for the phantom were as follows: MRI compatible, MR relaxation times similar to body tissues, smooth lumen that mimics vessel feel during navigation, compatible with flow, range of navigational difficultly, and the ability to accommodate 6 French catheters.

Phantom Box Construction: To provide physiologically relevant vessel trajectories, multiple symmetric angles (30-90°) and diameters (3/16-7/8 in.) were designed from Delrin rods connected together and placed in an acrylic box (Figure 1). PVA-C will be poured into the phantom box and cross-linked with freeze-thaw cycles. The rods will be removed leaving a pathway mimicking vessel lumens.

PVA-C Process: A test gel was created using a process previously outlined by Surry, et al. Sevol Grade 165 PVA powder (Sekisui Specialty Chemicals America, Dallas, TX) was used to create 10% PVA cryogel by mixing 50g of PVA powder and 450g of de-ionized water in a flask. The mixture was stirred for 30 minutes and heated in a steam autoclave at 121°C for 30 minutes. The resulting gel was stirred for 30 minutes, and then poured into a polymethylpentene jar. The gel was allowed to sit for 21 hours, spun on a clinical rotator for 2 hours, and then set for another hour. The phantom was then frozen at -20°C for 12 hours. At the end of 12 hours, the gel was cooled for 12 hours at room temperature. This cycle was repeated 3 times. Images were obtained with a 1.5 T scanner using T1 and T2-weighted images, along with quantitative T1 and T2 measurements.

Results and Discussion: Radiographic T1 and T2 images of the test phantom are shown in Figure 2. T1 and T2 relaxation times (mean ± SD) for the PVA-C were 1129 ± 309 ms and 188 ± 13 ms. The standard deviations show acceptable ranges for homogeneity, however the T1 and T2 values are slightly longer than the typical range for tissue. An additional freeze-thaw cycle will be performed to lower the relaxation times for the vascular phantom. These initial steps provide the foundation for a human-scale vascular phantom that can be used for testing navigation in our MARC endovascular catheter.

Figure 1

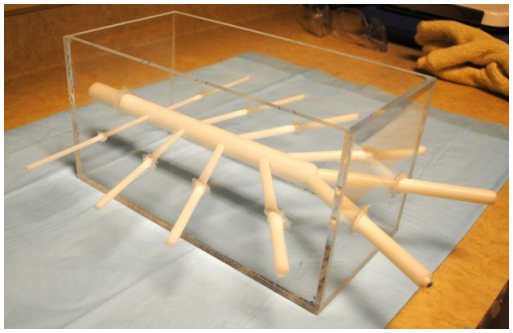

Figure 2

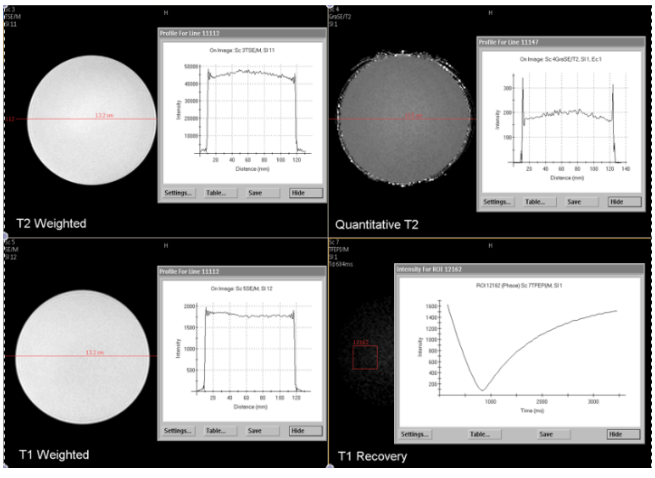

Relating Radiation Dose to Microbleed Formation in Patients with Glioma

Janine M. Lupo[1], Mekhail Anwar[2], Christopher P. Hess[1], Susan M. Chang[3], and Sarah J. Nelson[1,4]

[1]Radiology and Biomedical Imaging, [2]Radiation Oncology, [3]Neurosurgery, [4] Bioengineering and Therapeutic Sciences

Introduction: Radiotherapy (RT) is an integral component in the management of patients with glioma, but the damage that it can cause to healthy brain tissue function is of concern.[1] The histologic response to radiation initially shows characteristic vascular changes that later result in the formation of hemosiderin-containing deposits or microbleeds.[2] Our prior studies using Susceptibility-Weighted Imaging (SWI) have characterized the extent and time-course of these lesions[3]; however, the relationship between microbleed characteristics and RT dose has not been assessed. The goal of this study was to investigate the effects of RT dose on microbleed characteristics in patients with glioma.

Methods: SWI data from 10 patients with high-grade glioma scanned serially between 1.8 to 4.3 years from receiving RT were analyzed. Patients received external-beam RT with adjuvant chemotherapy. T2*-weighted images were acquired on a 3T scanner with an 8-channel head coil using a 3D flow-compensated SPGR sequence with TE/TR=28/56ms, flip=20°, FOV=24cm, matrix=512x144 with parallel imaging, and 2mm slice-thickness. Standard SWI post-processing was performed on each coil, and the combined images were projected through 8 mm-thick slabs. Microbleeds were identified as foci of susceptibility that did not correspond to vessels or contrast-enhancing tumor on consecutive slices. Radiation dosimetry maps were reconstructed on a Pinnacle treatment planning system and fused with the SWI images after alignment to the original treatment CT images[4]. The aligned dose maps were segmented into high- (>45 Gy), mid- (30-45Gy), and low- (15-30Gy) dose regions. To compare microbleed counts across patients, the number of microbleeds within each dose region was normalized by the volume of brain tissue in that region.

Results: Increases in microbleed density (MD) were observed with dose (Figure 1A&B). At 2 years post-RT, MD was significantly greater in the high-dose than mid-dose region ($p=0.03$, Wilcoxon signed-rank test) and no microbleeds existed in the low-dose region. By 3-4 years post-RT, microbleeds were observed in the low-dose region, though significantly fewer than in other regions ($p<0.02$). MDs at 3-4 years post-RT were significantly higher than corresponding MDs at 2 years post-RT in all dose regions ($p<0.001$). The rate of initial microbleed formation was correlated to the volume of the high-dose region (Spearman rank correlation, $r=.92$, $p<0.05$, Figure 1C). After 2 years, only a trend towards an increased rate of formation with larger lower-dose volume was observed. Microbleed volume was not related to dose.

Conclusions: We have demonstrated that the appearance of radiation-induced microbleeds is dependent upon dose of radiation received with increases in microbleed density in higher dose regions and microbleeds initially forming first in high-dose and later in lower dose regions. The rate of formation was dependent upon the volume of high-dose radiation the tissue received. The ability to detect these lesions and characterize their relationship with dose received to normal-appearing brain tissue may be important in determining which parts of the brain are most susceptible to radiotherapy, assessing cognitive outcome, and considering therapeutic strategies and planning target volumes in patients with lower grade tumors, who have longer survival.

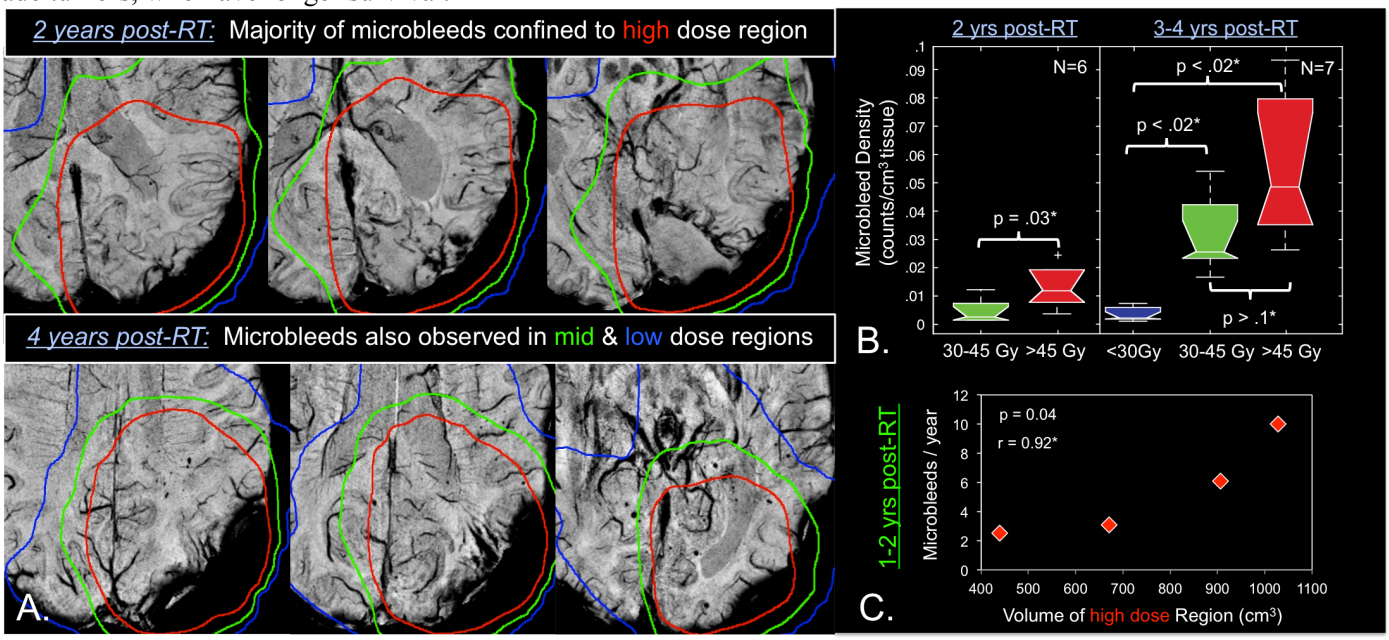

Figure 1. In A, contoured dose maps overlaid on SWI images. In B, comparison of MD, in low-,mid-, and high-dose regions. In C, correlation of microbleed formation with volume of high dose region 1-2 years post-RT.

References: [1] Karim A et al. *Int J Radiat Oncol Biol Phys* 2002;52(2):316-324, [2] Fajardo LF. Acta Oncol. 2005;44(1):13-22. [3] Lupo JM et al. Int J Radiat Oncol Biol Phys. Epub 2011 Oct 12. [4] Jenkinson M. et al *NeuroImage* 2002;17(2):825-841.

The research was supported by UC Discovery grant ITL-BIO 04-10148, and NIH grants R01 CA059880, R01 CA127612-01A1, & P50 CA97257

Catheters for Interventional MR: LaserLathe Fabrication of Micro-Coils for Remote Catheter Tip Deflection

V. Malba, P. Lillaney, A.F. Bernhardt, L.B. Evans, C.D. Harvey, T.P.L. Roberts, R.L. Arenson, M. Wilson, A.J. Martin, R. Taylor, S. Hetts

Introduction: Remote guidance of catheters for endovascular interventions has been the object of considerable research and development over the past ten years [1]. Much of that work was based on the idea that, in the presence of an external magnetic field, a correctly oriented magnetic moment at the catheter tip could be utilized to deflect the catheter into a particular blood vessel branch. One major approach utilizes the external magnetic field of an MRI to interact with a magnetic moment created by passing an electric current through coils placed at the catheter tip [2].

Methods: We propose a lithographic technique to manufacture the coils, which we call LaserLathe [3]. This method allows non-planar surfaces such as cylinders to be patterned with feature sizes as small as 5 um. A conductive coating (a "seed layer") consisting of a copper layer (~200 nm) over a titanium layer (~50 nm) was deposited on the non-planar surface with a sputtering system fitted with a rotary fixture for uniform deposition on a cylinder. The purpose of the Ti/Cu seed layer is to create a conductive layer onto which a positive electrodeposited photoresist can be electroplated. The photoresist coating provides a uniform photoactive layer on the surface which can be patterned with a laser. Figure 1 shows a schematic of the LaserLathe apparatus. It consists of three high-precision translation stages (x, y, and z), and one high-precision rotary stage. The axis of the rotary stage is parallel to the translation of the x-stage. The "cutting tool" for the LaserLathe is a 405-nm, 50 mW diode laser. It doesn't actually cut; it is used to expose the positive photoresist. The z-stage is used to focus the beam by moving a microscope objective through which the beam is passing. With precision motion control of the stages provided by a Delta Tau PMAC card, any design can be patterned on the surface of the cylinder.

Results/Discussion: Examples of typical designs are shown in figures 2 and 3, which illustrate the solenoid and racetrack coil designs. By encapsulating one of these cylinders within the other it is possible to create two-axis coil, which allows for magnetic moments to be created in two orthogonal directions at the tip of the catheter making the device more versatile. The most effective multi-axis design would have one coil pattern, a layer of dielectric, and the other coil pattern all on one cylinder. We are working on this approach as a future direction for this project.

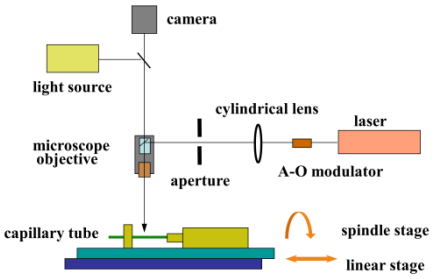

Figure 1: The LaserLathe apparatus.

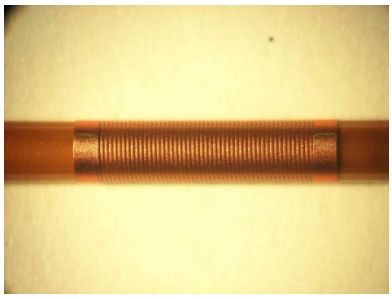

Figure 2: 50-turn helical coil patterned on a 1.37 mm OD polyimide cylinder. 0.5 mm collars at each end are solder attachment pads.

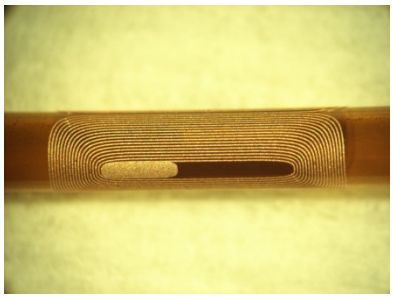

Figure 3: 40-turn racetrack coil. There is a solder attachment pad at the center of the racetrack

References:

1. Roberts, T.P., et al., *Remote control of catheter tip deflection: an opportunity for interventional MRI.* Magnetic resonance in medicine : official journal of the Society of Magnetic Resonance in Medicine / Society of Magnetic Resonance in Medicine, 2002. **48**(6): p. 1091-5.
2. Arenson RL, H.W., Roberts TPL. , *Magnetically directable remote guidance systems, and methods and use therof.*, U.S.P. Office, Editor 2001, The Regents of the University of California, Oakland, CA: United States.
3. Vincent Malba, R.M., Leland B. Evans, Anthony F. Bernhardt, Monique Cosman, Kin Yan, *Laser-Lathe Lithography--a Novel Method for Manufacturing Nuclear Magnetic Resonance Microcoils.* Biomedical Microdevices, 2003. **5**(1): p. 21-27.

Responsiveness of compartment-specific quantitative cartilage MRI measures over 2 years in individuals with knee osteoarthritis

Geetha Mohan, Deepak Kumar, Joseph A. Schooler , Thomas M. Link, Sharmila Majumdar

Musculoskeletal Quantitative Imaging Research Group, Dept. of Radiology and Biomedical Imaging, University of California San Francisco, San Francisco, CA, USA

Introduction: Osteoarthritis (OA) is one of the most common causes of disability. Accurate and non-invasive MR imaging techniques to detect changes in cartilage structure and composition are critical to track the progression of OA and to monitor treatment effects. Hence, it is essential to evaluate the responsiveness of these imaging techniques.

Aim: To evaluate the responsiveness of compartment specific morphological and compositional cartilage MRI measures over 2 years in knee OA patients.

Methods: Twenty four patients with knee OA (KL grade 1-4) underwent 3-T knee MRI at baseline, 12 and 24 months. High-resolution SPGR sequence was used for cartilage segmentation and calculation of cartilage thickness and volume. $T_{1\rho}$- and T_2- relaxation times (mean, bone layer and cartilage layer) were quantified using standard sagittal sequences. All parameters were calculated for the lateral femoral condyle (LF), medial femoral condyle (MF), lateral tibia (LT), medial tibia (MT) and the patella (PT) using an in-house software developed with Matlab. Standardized response mean (SRM) was calculated for each MRI measure between the three time points as the mean of change divided by the standard deviation of change.

Results: In this preliminary analysis, cartilage volume and T_2 relaxation times had higher SRM values over 2 years. The best cartilage volume SRM was for the lateral tibial compartment and the patella after 2 years (-0.74 and -0.6 respectively). The SRM for cartilage volume measures ranged from -0.1 to -0.49 and the SRM for $T_{1\rho}$ ranged from -0.1 to -0.51. The SRM for T_2 measurement (mean) was -0.52, -0.79 in the medial tibia at 1 year and 2 years respectively and -0.61 for patella at 2 years. The best SRM for T_2 measurement (bone layer) was -0.9 for medial tibia at 2 years. The SRM for T_2 measurement (cartilage layer) was -0.71 for the lateral tibia at 2 years, -0.57 for the medial tibia at 1 year and -0.76 for patella at 2 years.

Conclusion: These preliminary results suggest that cartilage volume and T_2 relaxation time measures are responsive to changes in cartilage over a period of 2 years in people with knee OA. We continue to perform additional analyses including more subjects to confirm these findings. These initial results suggest that these metrics may be useful as responsive outcome measures in prospective clinical studies and trials.

Acknowledgment: We thank all the subjects who participated in this study and Dr Xiaojuan Li for her expertise in MRI .

Responsiveness of compartment-specific quantitative cartilage MRI measures over 2 years in individuals with knee osteoarthritis

Geetha Mohan, Deepak Kumar, Joseph A. Schooler , Thomas M. Link, Sharmila Majumdar

Musculoskeletal Quantitative Imaging Research Group, Dept. of Radiology and Biomedical Imaging, University of California San Francisco, San Francisco, CA, USA

Introduction: Osteoarthritis (OA) is one of the most common causes of disability. Accurate and non-invasive MR imaging techniques to detect changes in cartilage structure and composition are critical to track the progression of OA and to monitor treatment effects. Hence, it is essential to evaluate the responsiveness of these imaging techniques.

Aim: To evaluate the responsiveness of compartment specific morphological and compositional cartilage MRI measures over 2 years in knee OA patients.

Methods: Twenty four patients with knee OA (KL grade 1-4) underwent 3-T knee MRI at baseline, 12 and 24 months. High-resolution SPGR sequence was used for cartilage segmentation and calculation of cartilage thickness and volume. $T_{1\rho}$- and T_2- relaxation times (mean, bone layer and cartilage layer) were quantified using standard sagittal sequences. All parameters were calculated for the lateral femoral condyle (LF), medial femoral condyle (MF), lateral tibia (LT), medial tibia (MT) and the patella (PT) using an in-house software developed with Matlab. Standardized response mean (SRM) was calculated for each MRI measure between the three time points as the mean of change divided by the standard deviation of change.

Results: In this preliminary analysis, cartilage volume and T_2 relaxation times had higher SRM values over 2 years. The best cartilage volume SRM was for the lateral tibial compartment and the patella after 2 years (-0.74 and -0.6 respectively). The SRM for cartilage volume measures ranged from -0.1 to -0.49 and the SRM for $T_{1\rho}$ ranged from -0.1 to -0.51. The SRM for T_2 measurement (mean) was -0.52, -0.79 in the medial tibia at 1 year and 2 years respectively and -0.61 for patella at 2 years. The best SRM for T_2 measurement (bone layer) was -0.9 for medial tibia at 2 years. The SRM for T_2 measurement (cartilage layer) was -0.71 for the lateral tibia at 2 years, -0.57 for the medial tibia at 1 year and -0.76 for patella at 2 years.

Conclusion: These preliminary results suggest that cartilage volume and T_2 relaxation time measures are responsive to changes in cartilage over a period of 2 years in people with knee OA. We continue to perform additional analyses including more subjects to confirm these findings. These initial results suggest that these metrics may be useful as responsive outcome measures in prospective clinical studies and trials.

Acknowledgment: We thank all the subjects who participated in this study and Dr Xiaojuan Li for her expertise in MRI .

Selective Effects of Vascular Risk Factors on Hippocampal Subfield Atrophy

Mueller SG, Schuff N, Kriger S, Truran D, Kramer J, De Carli C, Weiner MW, Chu H

Background: Hippocampal volume loss is a hallmark of dementia including cerebrovascular disease/dementia (CVD). However, the hippocampus consists of distinct subfields and there is evidence that they are differently affected by different disease processes. Alzheimer's Disease e.g. is characterized by volume loss in ERC, subiculum, CA1 and CA1-2transition (dorsal section of CA1) while volume loss in the preclinical stage (MCI) is most prominent in CA1-2transition. The purpose of this project was to investigate if cognitive impairment in subjects at risk for vascular disease is associated with a distinct pattern of subfield atrophy

Methods: The study encompassed 67 (mean(SD) age: 77.9(6.6), f/m: 42/25) cognitively intact (CDR 0: 48) and mildly impaired (CDR 0.5: 19) subjects with increased vascular risk (diabetes, hypertension, hyperlipidemia and/or corresponding treatment). Vascular risk factors (VRF) particularly fasting glucose ((mean(range)103.1(79-196)), total cholesterol (TChol 183.5(117-314)) and systolic (SBP)/diastolic (DBP) blood pressure (137.4(100-196)/74.7(60-94)) and whole-head T2 (ICV calculation), FLAIR (white matter lesion load (WML)) and PD weighted high resolution hippocampal images (manual subfield parcellation) were obtained in all subjects. A MANOVA was used to identify subfields with significant volume loss in CDR 0.5 subjects and stepwise regression analyses to determine which VRF or combination thereof significantly influenced subfield volumes.

Results: CDR 0.5 subjects had significantly smaller CA1 (mean(SD) 191.3(33.9) vs. 221.3(33.3), CA1-2transition (10.7(1.0) vs. 11.6(1.4)) and CA3&DG (134.1(20.9) vs. 158.4(25.2)) volumes than CDR 0. CA1 was negatively associated with SBP, CA1-2transition with TChol and CA3&DG with TChol and SBP. WML had a negative effect on CA1 but not on CA1-2transition or CA&DG. WML was positively associated with age but not with CDR status or VRFs.

Conclusions: The hippocampal atrophy pattern observed in this population of cognitively intact and mildly impaired elderly subjects with increased VRF was similar to that in preclinical AD with exception with the more severely affected CA3&DG. Elevated SBP and TChol were associated with volume loss in CA3&DG while CA1 and CA1-2transition were influenced by SBP respectively TChol. The selective vulnerability of these subfields for hypertension/hyperlipidemia is consistent with that described in animal models and autopsy studies. Their usefulness for diagnostic purposes has to be further investigated.

Quantitative Assessment of Fat Infiltration in the Rotator Cuff Muscles using MRI and Correlation with Clinical Parameters

Lorenzo Nardo[1], Sonia Lee[1], Dimitrios Karampinos[1], Julio Carballido-Gamio[1], Benjamin Ma[2], Thomas M. Link[1], Roland Krug[1,2]

[1]Musculoskeletal and Quantitative Imaging Research, Department of Radiology and Biomedical Imaging, UCSF, SF, CA
[2]Department of Orthopaedic Surgery, University of California, San Francisco, San Francisco, CA

Introduction: The fatty infiltration of rotator cuff muscles (RCM) is the main factor in the clinical decision making regarding the management of the patient with rotator cuff tear. For this reason it is crucial to accurately quantify fat within the muscles. The purpose of our work was to validate the semi-quantitative Goutallier's classification (GC) in comparison to a novel, quantitative chemical shift-based water-fat imaging technique termed IDEAL as predictors of clinical parameters, specifically strength, range of motion and pain.

Materials and Methods: Each rotator cuff muscle of 57 shoulder-MR images (30 males, 27 woman, aged between 22 and 69) was scored for fat infiltration independently by two radiologists using Goutallier's classification. A physical examination was conducted by an orthopedic surgeon. Clinical data concerning pain, strength and range of motion of the shoulder were recorded. All shoulder MR examinations were performed using a 3.0-T imager (MR750; GE Healthcare, Milwaukee, Wis) with a 4 channel shoulder surface coil (GE Healthcare Milwaukee, WI). MRI sequence selection included sagittal oblique T2-weighted fat suppressed fast spin echo, sagittal oblique T1-weighted, sagittal oblique proton density-weighted fast spin echo and a novel six-echo spoiled gradient echo pulse sequence. A slice thickness of 4 mm and a field of view (FOV) of 12 cm was maintained for all the sequences. Fat fraction maps were reconstructed online from the six gradient echo images using the IDEAL algorithm with T2* correction and a multi-peak model for the fat spectrum.

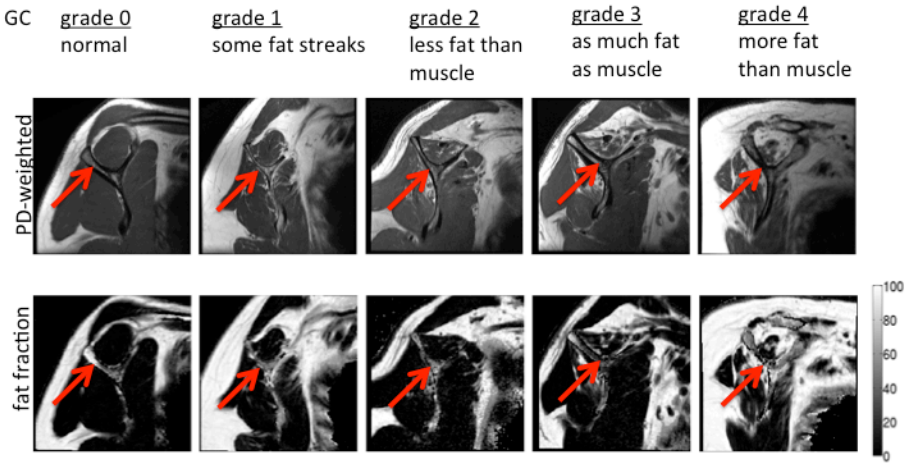

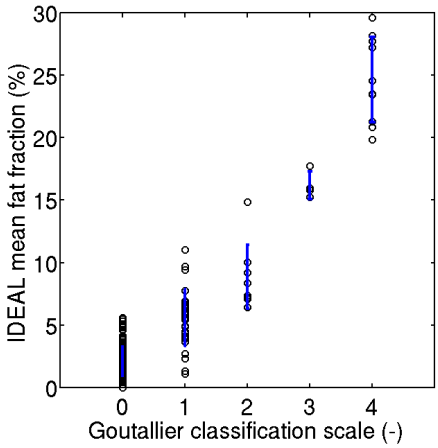

Figures: *Left:* Goutallier graded clinical PD-weighted images (top) are shown along with IDEAL fat fraction maps (bottom). *Right:* Comparison of GC and IDEAL fat fraction values in all four muscle compartments.

Results: A comparison of Goutallier graded clinical MR images and IDEAL images is shown in the left figure. GC correlated well with the quantitative IDEAL values (fisher exact test kappa > 0.9). Mean fat fraction values consistently increased with Goutallier grade (Figure right): grade 0 ranged from 0% to 5.59%, grade 1 from 1.1% to 9.70%, grade 2 from 6.44% to 14.86%, grade 3 from 15.25% to 17.77%, grade 4 from 19.85% to 87.17%. We found that GC consistently overestimates the fat content in the muscles. Ideal quantification of fatty infiltration showed better correspondence with clinical values than the clinical Goutallier score using Spearman rank correlation; in particular IDEAL fat quantification was able to predict deficit in strength, range of motion and pain better than the Goutallier score.

Discussion: Chemical shift based water-fat MRI is a novel tool, which allows accurate, quantitative assessment of fatty infiltration in the rotator cuff muscles with high accuracy. As fatty infiltration and atrophy in the RC muscles have been shown to be negative prognostic factors for successful repair of RC tears, an objective measure is clearly needed and would help the orthopedic surgeons in their decision-making process regarding different treatment options.

Funding Sources: NIH; Grant numbers: R01AR057336, 1P30AR058899.

^{13}C -MRSI with Dynamic Nuclear Polarization in Stimulated Splenic Lymphocytes

Linda Nguyen BS, Jeffrey Gu BS, Yi-Fen Yen PhD, John Kurhanewicz PhD, John MacKenzie MD

Purpose: To test and validate hyperpolarized ^{13}C-pyruvate and alterations in its conversion to ^{13}C-lactate as an imaging biomarker for disease severity in inflammation.

Methods: Balb/c mice were induced with systemic inflammation by IP injection of 1 or 5 mg/kg lipopolysaccharide (LPS) or control phosphate buffered saline (PBS). LPS stimulated splenic lymphocytes were harvested at 2 days after induction of inflammation. Metabolism of pyruvate and its conversion to lactate were measured in three ways: 1) colorimetric enzymatic assay for lactate production in cell culture media at 0.5-4 hours after cell harvest, 2) qRT-PCR measurement of mRNA transcript levels for lactate dehydrogenase (LDHA/B), the enzyme responsible for converting pyruvate to lactate, and monocarboxylate transporter (MCT1 and 4), the cell-surface molecules responsible for intra/extra-cellular lactate shuttling and 3) non-invasive carbon-13 magnetic resonance spectroscopic imaging (^{13}C-MRSI) by incubating cells with hyperpolarized ^{13}C-pyruvate using dynamic nuclear polarization (DNP) and then detecting the conversion of pyruvate to lactate with ^{13}C-MRSI.

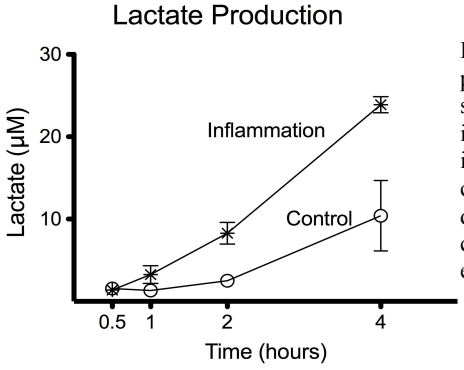

Figure 1. Lactate production in stimulated (LPS induced inflammation) and control cells, detected by colorimetric enzymatic assay.

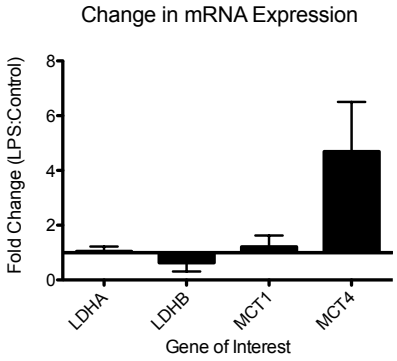

Figure 2. Expression levels of LDHA, LDHB, MCT1, and MCT4 after LPS induced inflammation.

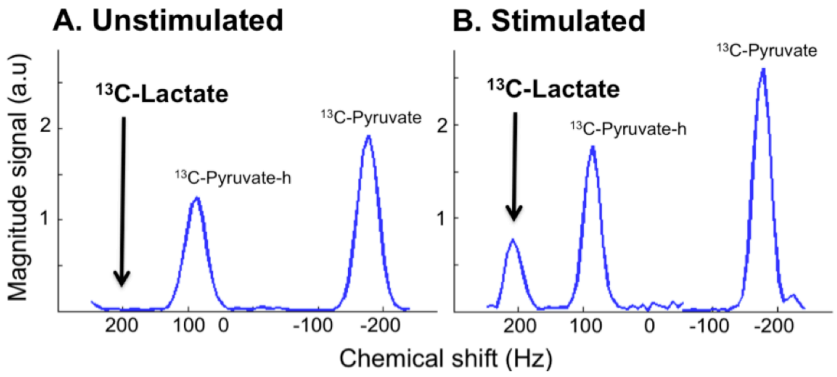

Figure 3. Lactate production in -/+LPS stimulated cells, detected by ^{13}C-MRSI with hyperpolarized ^{13}C-pyruvate.

Results: Lactate levels and the molecular machinery used to produce and transport lactate were altered in inflamed cells. In aliquots of media obtained from cell culture, lactate production was significantly increased in stimulated splenic lymphocytes (Fig. 1). RNA extracted from stimulated lymphocytes had relatively unchanged expression levels of LDHA and MCT1 between stimulated and unstimulated cells: however, expression levels of LDHB were slightly downregulated by 40%, while MCT4 was upregulated approximately 5-fold with LPS stimulation (Fig. 2). ^{13}C-MRSI with hyperpolarized ^{13}C-pyruvate showed that stimulated lymphocytes produced greater amounts of ^{13}C-lactate than unstimulated lymphocytes (Fig. 3).

Discussion: Our preliminary cell experiments suggest that lactate production is elevated in inflammation. This is supported by biochemical and ^{13}C-MRSI data. Higher levels of lactate with LPS stimulation were detected by both ^{13}C-MRSI with hyperpolarized ^{13}C-pyruvate and by a colorimetric enzymatic lactate assay. This may be because immune cells when stimulated have increased energy demands metabolizing pyruvate to lactate at higher levels. RNA expression experiments show that stimulation may cause changes at the cellular level. The significant upregulation of the purported lactate exporter MCT4 is an important result. By increasing MCT4 levels to transport more lactate out of the cell, stimulated cells may be compensating for the increased production of lactate. Future experiments with a macrophage cell line would determine specific cell types responsible for increased lactate levels with stimulation. In addition, treatment experiments would determine if ^{13}C-MRSI with DNP can detect treatment response; particularly, if treatment of stimulated cells with anti-inflammatory drugs results in attenuation of the ^{13}C-lactate levels detected.

A Technique for Laminar Analysis of Cortical Microstructure in Longitudinal Studies

Jasmine Nirody, Willy Tjong, Janina Patsch, Andrew Burghardt, Thomas Link, Brian Feeley, Ben Ma, Galateia Kazakia

Introduction: As the mechanical competence of long bones depends to a large degree on cortical structure, quantification of cortical structure parameters is vital to both fracture risk prediction and therapeutic intervention. Studies have shown that there exists considerable spatial variability in cortical microstructure, particularly porosity. The goal of this study was to develop a technique to characterize cortical microstructure variability specifically among laminar layers. Our motivation is that laminar assessment may elucidate mechanisms through which cortical porosity develops, for example by expansion of the marrow space, the vascular network, or both.

Materials and Methods: In the laminar analysis technique the cortical compartment is first segmented from high resolution peripheral QCT (HR-pQCT) images. Second, a 3D sphere-filling algorithm is used to find the cortical midline, which is then dilated in 1 deg sections by a local thickness map. This divides the cortex into three laminae corresponding to endosteal, intracortical, and periosteal regions (Fig. 1). A skeletonization routine is then used to assign each pore to a single lamina based on the location of the pore's centroid. Total pore area, total pore number, and average pore size are then calculated within each region. This technique was applied to a longitudinal HR-pQCT dataset obtained from the distal tibiae of individuals (n = 10, age = 34 +/- 8 yrs at baseline) undergoing knee surgery that required a 6-wk disuse period post-surgery. This dataset included a baseline scan just prior to the disuse period, a follow-up scan at the end of the 6-wk disuse period, and two additional scans in the recovery period following return to weight-bearing. Repeated measures ANOVA and post-hoc t-tests of each timepoint versus baseline were used to determine how parameters within each region evolved over time.

Results: At baseline, the highest total pore area was found in the endosteal layer (Fig. 2). High endosteal porosity was associated with high total pore number rather than high average pore size. Following the disuse period (Fig. 3), total pore area increased in the overall cortical compartment (+17.6% increase from baseline, $p<0.05$). Endosteally, this increase in total pore area was manifested through both increase in total pore number (8% increase, $p<0.05$) and average pore size (10% increase, $p<0.05$), while periosteal pores showed only significant increase in size (18% increase in average pore size, $p<0.01$).

Conclusion: Laminar evaluation of changes in porosity describe the microstructural genesis of increased porosity and suggest that unique mechanisms may act within endosteal and periosteal regions of the cortex in this disuse cohort.

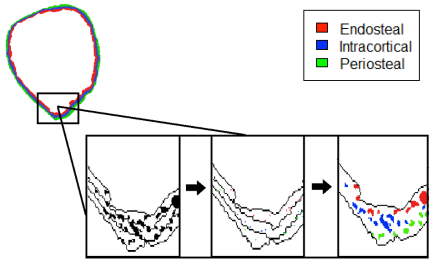

Fig. 1: The pore assignment technique is demonstrated on a small section of a tibial cross-section.

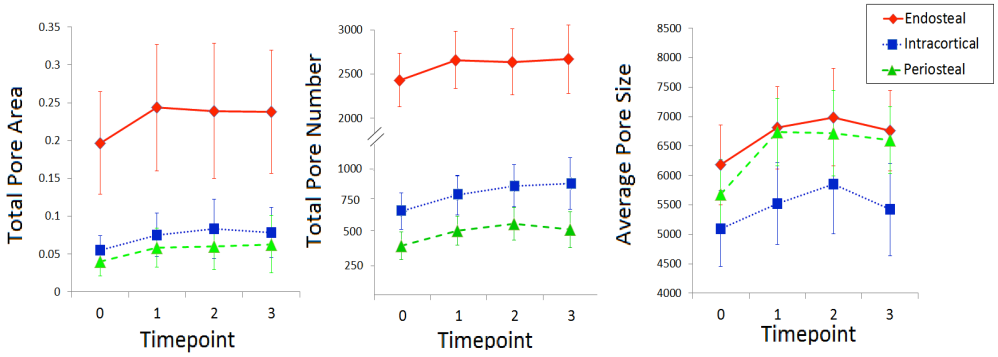

Fig. 3: Progression with time for TPA (top), TPN (bottom left), and APS (bottom right) at the distal site of the affected leg. Timepoints are denoted as follows: 0 = baseline, 1 = 6 wks after non-weight-bearing, 2 = 6 wks after return to weight-bearing, 3 = 12 wks after return to weight-bearing. For TPA and TPN, left vertical axes correspond to endosteal data, while right vertical axes correspond to intracortical and periosteal data. 95% CI are shown by error bars.

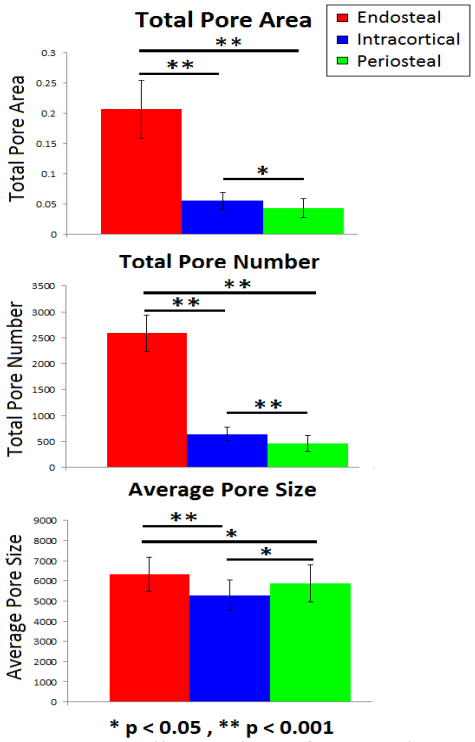

Fig. 2: Baseline values for Total Pore Area (TPA), Total Pore Number (TPN), and Average Pore Size (APS) in each laminar region.

Investigations of Aqueous Europium Fluorophores using Broadband Cavity Enhanced Absorption Spectroscopy

Ryan Orendorff[1, 2, 3, a)] and Clemens Kaminski[3]
[1)] *University of California San Francisco, San Francisco USA*
[2)] *University of California Berkeley, Berkeley USA 94704*
[3)] *University of Cambridge, Cambridge UK CB3 0DS*

(Dated: 21 September 2012)

Many modern spectroscopic techniques that attempt to understand electronic transitions of atoms in material are limited by the light sources available to the instrument. Common spectroscopic light sources limit the bandwidth available to probe a substance or require extremely long acquisition times to acquire a spectrum due to the sequential wavelength scanning. The development of "white" lasers has allowed for spectroscopic information to be acquired using a broad range of wavelengths simultaneously, while reducing the acquisition time through the high power from the laser. White lasers, when coupled with an optical cavity, create a ideal candidate for acquiring highly sensitive broadband spectroscopic data at fast acquisition rates. This technique is commonly known as *Broadband Cavity Enhanced Absorption Spectroscopy* (BBCEAS).

In this report, a BBCEAS setup with a supercontinuum fibre laser source was created to identity trace concentrations of analytes inside a liquid medium. Performing spectroscopic measurements in a liquid environment is quite difficult due to the attenuation and scatting of the light in liquid media. However, our BBCEAS instrument was able to acquire spectra from nanomolar concentrations of rhodamine 6G, with a bandwidth of 150 nm at acquisition times in the milliseconds. In addition, the effects of laser intensity fluctuations, mirror imperfections, and liquid turbulence were examined and corrected for using a novel statistical technique not previously seen in the literature.

With a well characterised BBCEAS instrument, experiments were performed on measuring the concentration of aqueous europium and europium complexes in a solution. Europium is a peculiar metal lanthanide metal because it's photoluminescent quantum yield is nearly one, and yet its absorption cross section is exceptionally tiny. This makes europium an ideal fluorophore if it can be put in an environment that increases its absorption cross section. This can be done by placing europium in a chelation complex, which acts as a catcher's mitt for photons coming towards the complex and acts to increase the signal in an absorption measurement. These chelation complexes can be tailored to obtain specific absorption wavelengths, fluorescent wavelengths and branching ratios.

Europium contains a magnetic dipole moment that allows for both an accurate prediction of the branching ratios from the chelation complex and the ability to perform experiments in a simple manner using only the absorption spectrum from the chelated europium. This report provides the theoretical calculations to determine the photoluminescent properties of europium chelated fluorophores, and the BBCEAS instrumentation provides a simple yet sensitive method by which to measure the absorption spectra required for the theoretical calculations.

This theoretical and experimental combination allows researchers to create a "tunable" fluorophore with high quantum yields, opening up possibilities for novel, sensitive fluorescence measurements. For example, a europium tailored fluorophore can be used as in a protein assays to detect not only minuscule quantities of proteins but to also identify which proteins are in the solution. Additionally, the ability to tailor the fluorescent wavelengths allows for the creation of narrow bandwidth OLEDs that require only minute concentrations of europium in order to provide an intense signal.

[a)] Email: ryan.orendorff@ucsf.edu

The Structural Connectome of the Human Brain in Agenesis of the Corpus Callosum

Julia P. Owen[1,2], Yi-Ou Li[1], Etay Ziv[1], Zoe Strominger[3], Jacquelyn Gold[3], Polina Bukhpun[3], Mari Wakahiro[3], Eric J. Friedman[4], Elliott H. Sherr[3], Pratik Mukherjee*[1,2]

[1]Department of Radiology & Biomedical Imaging, University of California, San Francisco
[2]Department of Bioengineering & Therapeutic Sciences, University of California, San Francisco
[3]Department of Neurology, University of California, San Francisco
[4]International Computer Science Institute, University of California, Berkeley

Adopting a network perspective, the structural connectome reveals the large-scale white matter connectivity of the human brain, yielding insights into cerebral organization otherwise inaccessible to researchers and clinicians. Connectomics has great potential for elucidating abnormal connectivity in congenital brain malformations, especially axonal pathfinding disorders. Agenesis of the corpus callosum (AgCC) is one of the most common brain malformations and can also be considered a prototypical genetic disorder of axonal guidance in humans. In this exploratory study, the structural connectome of AgCC is mapped and compared to that of the normal human brain. Multiple levels of granularity of the connectome are investigated, including global network metrics, modularity analysis, and edge space comparisons, uncovering four major findings. First, the network topology of AgCC is more variable than that of the normal human connectome. Second, comparison of the AgCC connectome to that of controls after simulated removal of all callosal connections ("virtual callostomy") shows that aberrant connectivity in AgCC is much more pervasive throughout the brain than can be explained by the absence of callosal fibers. Third, modularity analysis reveals that many of the tracts that comprise the structural core of the cerebral cortex have relatively weak connectivity in AgCC, especially the cingulate bundles bilaterally. Finally, virtual lesions of the Probst bundles in the AgCC connectome demonstrate that there is consistency across subjects in many of the connections of these ectopic white matter tracts, and that they are a mixture of cortical and subcortical fibers. These results go beyond prior diffusion tractography studies to provide a systems-level perspective on anomalous connectivity in AgCC. Furthermore, this work offers a proof of principle for the utility of the connectome framework in neurodevelopmental disorders.

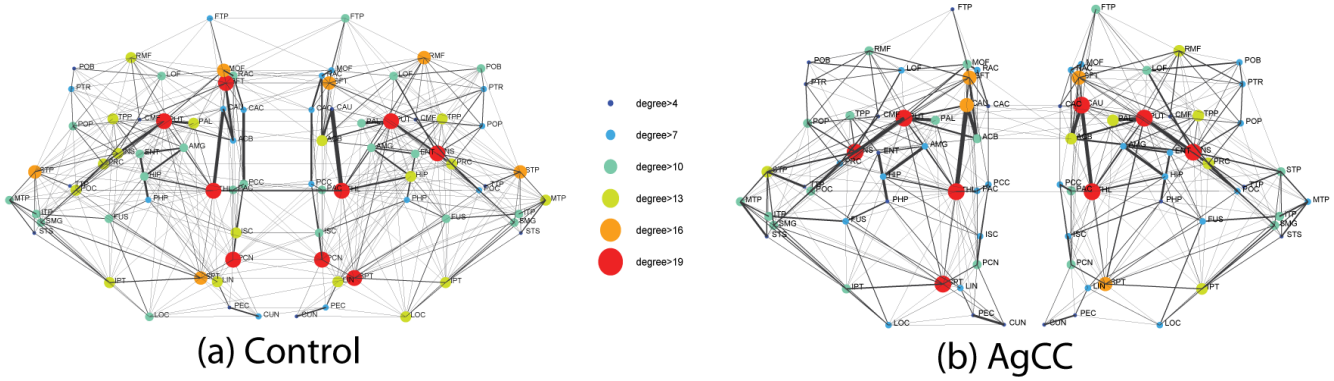

Figure: The consensus structural connectome for the control subjects (a) as compared to the consensus connectome for the AgCC subjects (b). The hubs (highly connected nodes) of the control consensus connectome are a mix of cortical and subcortical nodes. The hubs for the AgCC consensus connectome tend to be subcortical and the bilateral precuneus is demoted from hub status.

Investigating Parallel Imaging Performance of the 8-Channel Transceiver Array With Tilted Microstrip Elements

Yong Pang[1], Bing Wu[1], Daniel B Vigneron[1,2,3] and Xiaoliang Zhang[1,2,3]
[1]Radiology&Biomedical Imaging, University of California San Francisco, San Francisco, CA, United States, [2]UCSF/UC Berkeley Joint Graduate Group in Bioengineering, San Francisco & Berkeley, CA, United States, [3]California Institute for Quantitative Biosciences (QB3), San Francisco, CA, United States

Introduction: Parallel imaging techniques [1-3] require specialized multi-channel coil array with excellent decoupling performance. In previous studies, receiver array and transceiver array with tilted elements have been introduced to improve decoupling performance, enhance RF coil efficiency and reduce the power deposition [4-6]. In this work, parallel imaging performance was investigated in terms of reconstructed image quality, noise correlation matrix and g-factor.

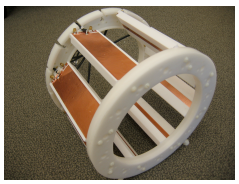

Fig.1 8-channel tilted array

Methods: Fig.1 shows the previous proposed 8-channel transceiver array with tilted microstrip elements [5,6]. To evaluate its parallel imaging performance, each element was tilted by around 30° and MR imaging experiments were performed on a General Electric (GE) 7T whole body scanner. Human knee images from a healthy volunteer were acquired with this array by using gradient echo sequences. In SENSE imaging the accelerated reconstruction with acceleration factors of 2 to 8 was demonstrated and the noise matrix was calculated. For GRAPPA accelerated imaging, 32 Auto-Calibration Signal (ACS) lines were acquired to estimate the missing lines. The GRAPPA reconstruction with acceleration factor from 2 to 8 was performed.

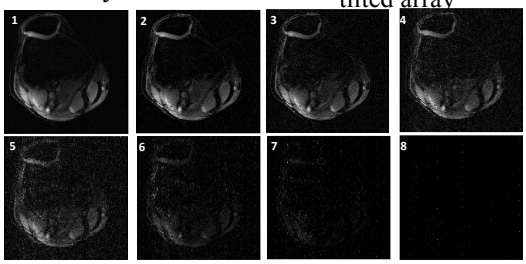

Fig.2 Image 1 is the reference image reconstructed using sum of square; Image 2 to 8 are reconstructed using SENSE at acceleration factor of 2 to 8.

Results: Fig. 2 shows the reconstructed images of the in vivo human knee using SENSE method. Fig.3 demonstrates the noise matrix which describes the noise correlation in the channels of the tilted array. Small noise correlation between array channels is desired because the SNR is inverse proportional to the noise correlation. In Fig.4, the average and maximum g-factors are plotted as functions of acceleration factor. The exact values of g-factors are listed in Tab.1.

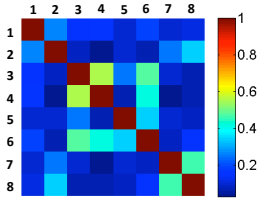

Fig.3 Noise correlation

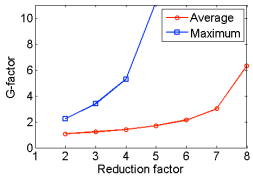

Fig.4 g-factor

Fig.5 shows the reconstructed images of human knee using GRAPPA. The first image is a reference image which was reconstructed from full *k*-space. When the acceleration factor was smaller than 4, there was not obvious distortion to the image and the image quality was acceptable.

Conclusions: The parallel imaging performance of the 8-channel tilted microstrip array has been investigated using two of the commonly used parallel imaging methods: SENSE and GRAPPA.

R	2	3	4	5	6	7	8
Ave	1.08	1.21	1.41	1.70	2.14	3.01	6.32
Max	2.23	3.39	5.27	11.26	15.05	53	457

Tab.1 Average and maximum g-factor at R=2 to 8.

In vivo human knee MR imaging was performed and images at different acceleration factors were reconstructed. The reconstructed images, noise correlation matrix and g-factor plot demonstrated excellent parallel imaging performance of the tilted microstrip transceiver array. High decoupling performance helps to decrease noise correlation among array elements, which decreases the g-factor and increases the parallel imaging performance.

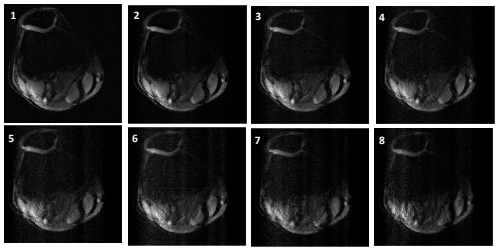

Fig.5 Images reconstructed using GRAPPA at acceleration factor of 2 to 8.

Acknowledgments: This work was supported by NIH grants EB004453, EB008699, EB007588, EB007588-03S1 and a QB3 opportunity award.

References: [1] D.K. Sodickson, et al, Magn Reson Med 1997;38(4):591-603. [2] K.P. Pruessmann, et al, Magn Reson Med 1999;42(5):952-962. [3] M.A. Griswold, et al, Magn Reson Med 2002;47(6):1202-1210. [4] C. J. Hardy, et al. ISMRM 13th 2005 pp 677. [5] B. Wu, et al. ISMRM 18th 2010 pp 3825. [6] Y. Pang, et al. ISMRM 18th 2010 pp 47.

Vessel size, Blood volume and Oxygenation: A phantom study.

Nicolas Pannetier, Norbert Schuff

Center for Imaging of Neurodegenerative Diseases

Introduction: MRI is a powerful tool to investigate the microvasculature. Various techniques benefit from the entanglement of the contrasts that arise within a voxel and provide relevant biomarkers such as vessel size index or vessel oxygenation [1-2]. However, the analysis relies on analytical models that suffer from restricted assumptions and lead to inaccurate estimates [3]. In this work, we present a versatile numerical model that overcomes these limitations. We evaluate our model on phantom data where vessels are modeled by polyamide (PA) strings. We demonstrate that this tool could be use to estimate the radius of the vessel without the use of contrast agent.

Methods: ***Model*** **–** We designed an algorithm that simulates the MR signal within a voxel taking into account the intrinsic R_2 relaxation, the magnetic field perturbations induced by susceptibility interfaces and the restricted diffusion of the water molecules. The voxel contains vessel of radius R that occupy the volume fraction Vf. The magnetic susceptibility difference between the vessels and the tissue, $\Delta\chi$, and the diffusivity of water molecules are inputs of the model. ***Phantom*** **–** Three phantoms with PA strings immersed in a NiSO4 solution were used. The radius of the PA strings were R=27µm, 89µm and 245µm with volume fraction Vf=2%, 2-3% and 2-3% respectively [4]. ***MRI*** **–** A gradient-echo sampling of the spin-echo (GESSE) sequence [5] was used to acquire the MR signal in the vicinity of the spin echo (T_E = 68ms, 32 echoes, 3x3x6mm^3). Multi spin-echo (CPMG) and multi gradient-echo sequences were used for T_2 and B_0. Water diffusion was assessed by diffusion weighted EPI sequence. ***Analysis*** **–** The CPMG signal was fitted with the extended phase graph algorithm [6] using the Levenberg-Marquardt minimization (LM). The derived value was used to correct the GESSE signal from the T_2 decay. The resulting signal was then fitted with our model using a lookup table to initiate the seed point of the LM minimization. R, Vf, and $\Delta\chi$ were eventually estimated either on averaged ROI or voxel wise. Voxels with $r^2<0.8$ were rejected.

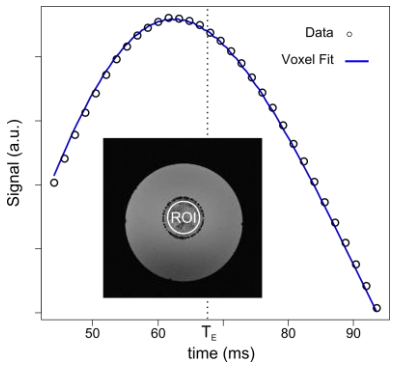

Fig 1 – Example of the ROI data and the corresponding fit (Phantom 1).

Results: ***ROI analysis*** **–** Figure 1 illustrates the result obtained in the ROI of phantom 1 (R=27µm). Table 1 presents the expected and estimated R, Vf and $\Delta\chi$ obtained from the ROI analysis within the 3 phantom datasets. For the low radius, R and Vf are in good agreement with the expected values whereas $\Delta\chi$ is unreliable. For high radius, the estimate of R is biased whereas Vf and $\Delta\chi$ are in agreement with the expected values. ***Voxel analysis*** **–** About 25% of the voxels were rejected. Figure 2 shows the histograms of R, Vf and $\Delta\chi$ estimated in phantom 1. The density of R is narrow with a maximum at 28µm in good agreement with the expected value. The scattering observed for Vf estimates can be ascribed to the inhomogeneous distribution of the strings within the phantom.

Phantom	R (µm)		Vf (%)		Δχ (ppm)	
	Expected	Estimated	Expected	Estimated	Expected	Estimated
1	27	27.5	2	2.3	1.25	0.79
2	89	59.7	2-3	5.6	-	0.81
3	245	174	3	2.8	1.02	1.04

Table 1 – Estimates of R, Vf and $\Delta\chi$ obtained from the ROI analysis.

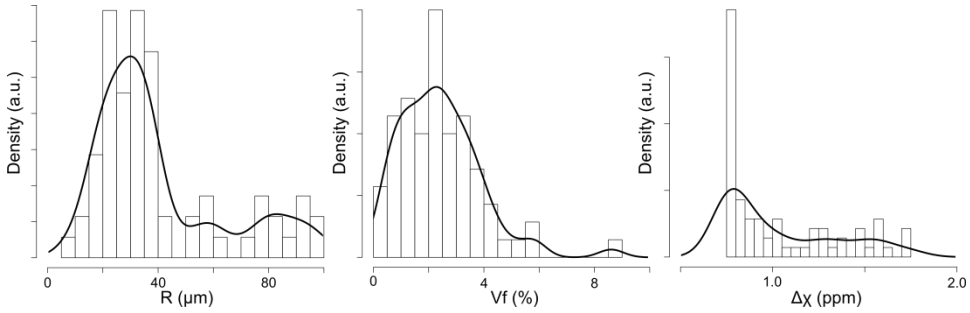

Fig 2 – Histograms of R, Vf and $\Delta\chi$ obtained with phantom 1 (R=27µm) on a voxel wise basis.

Conclusion: This phantom study demonstrates that our numerical model provides a mean to estimate the vessel radius without the use of contrast agent. This must be pursued with in vivo studies.

[1] Tropres et al., MRM, 2001. [2] Christen T et al., NMR in Biomed, 2012. [3] Dickson et al., JMR, 2011. [4] Sohlin et al, JMRI, 2011. [5] Yablonskiy, MRM, 1998 [6] Hennig, Conc Mag Res, 1991.

Mutual Coupling Effect Precompensation for Spatial Domain Method Based Parallel Transmission

Yong Pang[1], Daniel Vigneron[1,2], Xiaoliang Zhang[1, 2]
[1]Radiology&Biomedical Imaging, University of California San Francisco, San Francisco, CA, United States, [2]UCSF/UC Berkeley Joint Graduate Group in Bioengineering, San Francisco & Berkeley, CA, United States

Introduction: The mutual coupling effect on the excitation profile of transmit SENSE [1] can be reduced using the precompensation method previously proposed [2] by introducing the mutual coupling coefficient matrix into the pulse design procedure. In this project, we extended this method to the spatial domain method [3].

Theory and method: The excitation pattern from multiple coils with mutual coupling efficient $c_{m,n}$ is:

$$m(\mathbf{x}) = i\gamma M_0 \sum_{m=1}^{R} S_m(\mathbf{x}) \int_0^T \sum_{n=1}^{R} c_{m,n} B_{1,n}(t) e^{i\mathbf{x}\cdot\mathbf{k}(t)} dt \quad (1)$$

. By discretizing time to N_t samples and space to N_s samples as that in the spatial domain method [3], we can rewrite:

$$m = \sum_{r=1}^{R} D_r A B_r \quad (2)$$

, where D_r is defined as:

$$D_r = diag\{S_n^*(\mathbf{x}_i)\} \quad (3)$$

, where $S_n^*(\mathbf{x}_i)$ is:

$$S_n^*(\mathbf{x}) = \sum_{m=1}^{R} c_{m,n} S_m(\mathbf{x}) \quad (4)$$

. The sensitivity $S_n(\mathbf{x}_i)$ in Eq.(2) is replaced by $S_n^*(\mathbf{x}_i)$ which equals the sum of all the individual sensitivity pattern multiplied by the corresponding mutual coupling coefficient. This corresponds to compensation for the mutual coupling in the excitation. To investigate the feasibility, excitation pulses were designed using the two methods respectively for comparison. The desired excitation pattern was excited using a 4-element array with the reduction factor of 2. The sensitivity pattern of each element is shown in Fig.1. The mutual coupling coefficient matrix between the elements is shown in Fig.2.

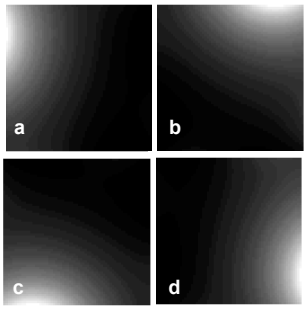

Fig. 1 Sensitivity patterns

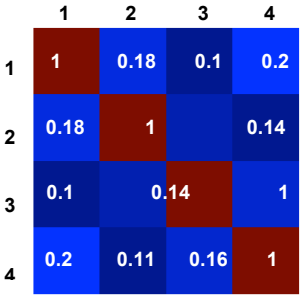

Fig.2. Coupling coefficients.

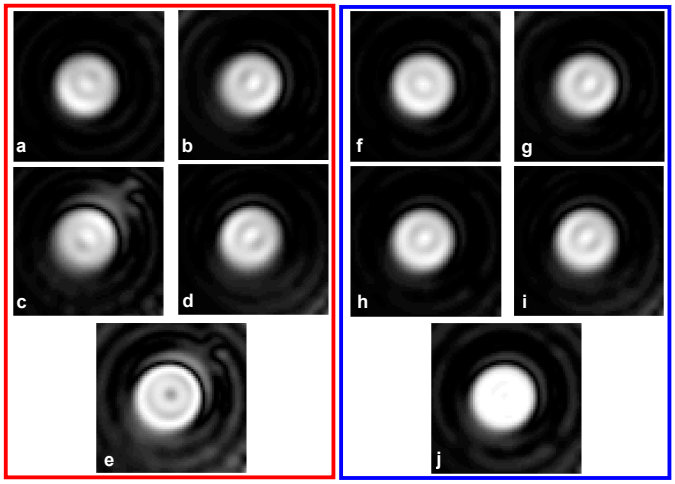

Fig.3. Simulation results of the excitation profiles using a 4-element coil array: (a – d) individual excitation pattern of each element by using spatial domain method; (e - h) individual pattern by using the precompensation method; (i) the aliasing can't cancel each other which lead to artifacts; (j) the artifacts caused by the mutual coupling were effectively reduced.

Results: The excitation pattern of each array element was illustrated in Fig. 3 (a)-(d). When the pulses were designed using spatial domain method with existence of mutual coupling, the artifacts in the resulting excitation pattern is unable to be cancelled by each other. This leads to the deteriorated excitation pattern. With the use of the proposed precompensation method, the mutual coupling between the elements is able to compensated, resulting in reduced artifacts in the excitation pattern of each element. This demonstrates that the mutual coupling effect of imperfectly designed transmit arrays can be efficiently corrected.

Conclusions and discussions: The precompensation method has been applied to the spatial domain method for parallel transmit to overcome the mutual coupling effect in transmit coil arrays and improve the parallel excitation pattern. This is very helpful for parallel transmission because current decouple methods are usually not able to thoroughly eliminate the mutual coupling in RF transmit arrays.

References: [1] Katscher U, et al, Magn Reson Med 2003; 49: 144-150. [2] Pang Y, et al, ISMRM 2005: p887. [3] Grissom W, et al, Magn Reson Med 2006; 56: 620-629.

Acknowledgements: This work was partially supported by NIH grants EB004453, EB008699, EB007588-03S1 and P41EB013598, and a QB3 Research Award.

Title:
The RSNA Image Share Network: Initial 12 Month Results from the UCSF Pilot Site

Authors:
Anand S. Patel, Wyatt M. Tellis, Mary Toroyasan, David E. Avrin, and Ronald L. Arenson

Background:
Medicare expenditure on imaging has nearly doubled from $6.5B in the year 2000 to $11.7B in 2009. At least 10-20% of these costs are due to duplicate exams, frequently due to the inaccessibility of prior studies during the transfer of care between institutions. In response the RSNA, in partnership with the NIBIB, launched the Image Share Network in 2009. The network aims to improve efficiency, safety, and empower patients with direct control of their exams via a secure HIPAA compliant cloud based personal health record (Fig. 1). As 1 of 5 national pilot sites, we present our experience with patient enrollment, adoption, and satisfaction.

Methods/Results:
With IRB approval, enrollment began in August 2011 with patients coming to the department's film library to obtain a CD of their exams. Four of the five initial pilot sites are currently online and enrolling patients. A total of 1383 patients with 5807 exams, have enrolled from all sites. The authors' site's share is 447 patients and 2288 exams. During the first ten months of the enrollment period (August 2011 – May 2012) the authors' site adopted the strategy of enrolling patients when they contacted the film library for a copy of their images on a CD. During this period a total of 90 patients, an average of 9 patients/month, were signed up. When asked about the low enrollment rates, film library staff indicated that patients were in a hurry, and not willing to spend the time to go through the educational and consent process. Starting in June 2012, the patient recruitment process was redesigned to enroll patients while they were waiting to be scanned. A recruitment coordinator was hired and dedicated to the task. As a result, in the three months (June – August 2012) since starting the new process a total of 357 patients have been enrolled. This is a monthly average of 119 patients, an increase of 1222% over the average of the previous 10 months (Fig. 2). Starting in August 2012, patients were also provided surveys to gauge their satisfaction with the system as well as their baseline computer/internet. Incentive gift cards will be provided to those patients who return the survey. Preliminary follow-up survey questions will be scored to assess for a relationship between patients' computer/internet use and their satisfaction with the Image Sharing system.

Discussion:
Despite low initial enrollment, since a lengthy conversation with patients is required for recruitment, the modification to include a study coordinator helped increase numbers to their highest monthly total to date. Survey data and initial patient demographics will be characterized in the near future once a substantial number of surveys have been accumulated to reach statistical significance (likely by late Oct 2012).

Conclusion:
A patient controlled, image enabled personal health record is feasible; however, traditional radiology film library workflow can be optimized to maximize patient enrollment.

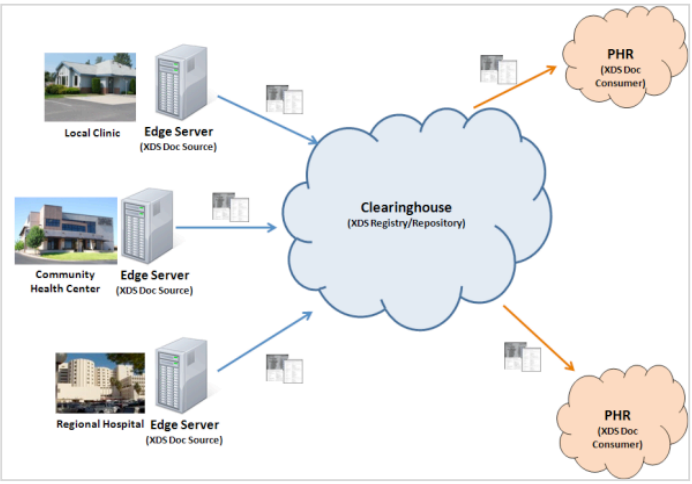

Fig 1. Overview of RSNA Image Share Cloud Based System

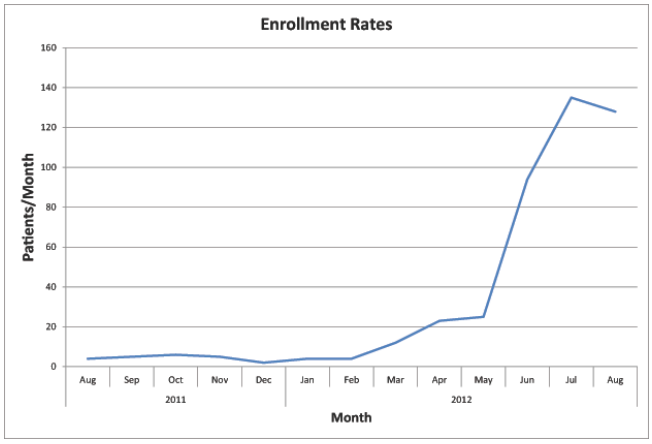

Fig 2. Enrollment rates over time of study. Notice significant increase in May 2012 after hiring of a study coordinator.

Weight loss reduces progression of cartilage T2 relaxation time values measured by 3T MRI - 48-month follow-up data from the Osteoarthritis Initiative

Authors: Theresa Poulos, Arman T. Serebrakian, Hans Liebl, Gabby Joseph, Michael C. Nevitt, John A. Lynch, Charles E. McCulloch and Thomas M. Link

Abstract

Objective

We examined the effect of weight loss on progression of knee cartilage magnetic resonance (MR) based T_2 relaxation times in asymptomatic individuals with risk factors for osteoarthritis (OA) using 3T MRI. Our specific aims were (i) to analyze how weight loss affects cartilage composition using T2 relaxation time measurements over 48 months in individuals with BMI loss of more than 10%, (ii) to compare these changes with those in a normal age- and gender-matched reference cohort without weight change, and (iii) to investigate the interplay between baseline BMI, weight loss, and T2 relaxation time measurements over a period of 4 years.

Study Design

Right knees MRIs of 127 subjects with risk factors for OA were studied. The data used in this study were obtained from the Osteoarthritis Initiative (OAI) database. Subjects were grouped into 2 cohorts based on change in BMI over a 48-month period: a weight-loss cohort (BMI decrease ≥ 10%, n=62) and a control cohort (BMI change < 3%, n=65). Segmentation of cartilage from 5 compartments (patella, medial femur, lateral femur, medial tibia, and lateral tibia) at both baseline and 48-month follow-up were performed, and T2 maps were generated. Statistical significance was determined using independent *t*-tests, χ^2 analysis, Spearman Rho correlations, and multiple logistic regression models.

Results

Progression in mean T2 values was significantly less in the medial femur, the medial tibiofemoral compartment and the global joint of the weight-loss cohort compared to the control cohort ($p<0.05$). Similar trends were seen in all other compartments. A significant correlation between change in medial femur cartilage T2 values and BMI change ($p<0.0001$) was also demonstrated. Compared to overweight subjects, obese individuals within the weight-loss cohort had significantly lower changes in T2 values in the lateral femur (p=0.032), medial femur ($p=0.027$), and patella ($p=0.015$) compartments.

Conclusions

This study showed that individuals who lost ≥10% of their baseline BMI over 48 months showed a significantly smaller increase in cartilage mean T2 relaxation times in the medial femur and overall medial compartments, and globally across the entire knee, as compared to controls who had <3% change in BMI over the same time period ($p=0.031$, $p=0.005$, and $p=0.0.044$, respectively). Furthermore, at baseline, there were no significant differences in the mean T2 relaxation times between the control and weight-loss groups in any of the knee compartments studied, while after 48 months the weight-loss group had significantly lower mean T2 values at the medial femur (OR=0.499, $p=0.031$), the medial tibia (OR=0.372, $p=0.010$), and the overall medial compartment (OR=0.315, $p=0.003$). We also observed that as more weight was lost, mean T2 values increased significantly less in the medial femur over 48 months ($p<0.0001$), with similar trends in all compartments. In conclusion, we found that weight loss is associated with decreased progression of cartilage T2 values in individuals with risk factors for OA but without radiographic or symptomatic evidence of the disease.

In Vivo Localized Correlation Spectroscopy using Spectral-Spatial Coherence Transfers

Galen D. Reed Trey Jalbert Gerd Melkus Simon Hu Peder E. Z. Larson
Sarah J. Nelson John Kurhanewicz Daniel B. Vigneron

September 21, 2012

1 Introduction

Two dimensional correlation spectroscopy (COSY) is an useful tool for in vivo detection of metabolites since the spectral sparsity afforded by the extra spectral dimension enables easier identification of overlapping resonances. *In-vivo* COSY [1] is particularly challenging for many reasons. Heterogeneous relaxation times in tissue confound water suppression by pre-saturation. Furthermore, to encode cross peaks of weakly coupled spin systems, both of the coupling partners of the molecule must be fully refocused. Therefore, all refocusing pulses must have high spectral bandwidth and thus have high peak power requirements. A variation of the COSY sequence using spectral spatial refocusing pulses for robust water suppression is presented. High bandwidth and low peak power is achieved by phase modulation of the spectral filter. Initial in vivo data from a healthy volunteer shows robust water suppression and strong metabolite cross peaks.

2 Methods

A localized COSY sequence was designed using a $\pi/2 - \pi - \pi/2$ slice select gradients played on orthogonal axes. The spectral spatial π and $\pi/2$ pulses were designed using a $T(BW) = 11$ minimum phase filter which was then root flipped to reduce peak power. Since the root flipping imparts a nonlinear phase to the transverse magnetization, the π and $\pi/2$ pulses were using the same $\beta(z)$ filter differing only by a scale factor $\sin\theta/2$. The filters were then passed through the inverse Shinnar Leroux transform [2, 3]. The resulting transverse magnetization of this sequence is

$$M_{xy} = M_{xy,0}\left(\beta^*_{180}\right)^2\left(\beta_{90}\right)^2.$$

Therefore, if β_{180} and β_{90} are phase-matched, the phase of the magnetization is unaffected. The sequence was run in a healthy volunteer on a 3T scanner using 128 indirect encodes, 8 averages per encode, 800 μs increment per encode.

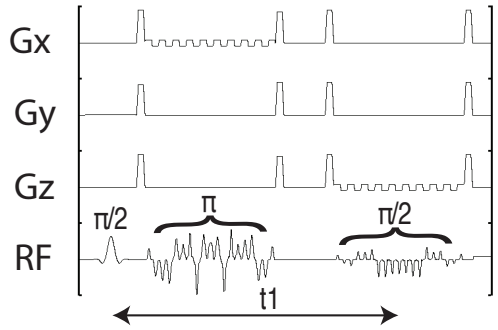

FIGURE 1: Localized COSY sequence using spectral spatial refocusing π and $\pi/2$ pulses. The pulses are phase modulated for peak power reduction.

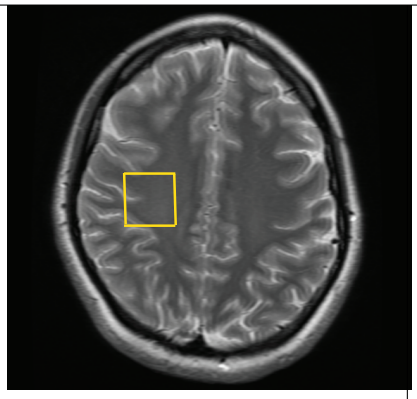

FIGURE 2: Axial SPGR of a healthy volunteer showing the 3cm × 3cm × 3cm selected volume

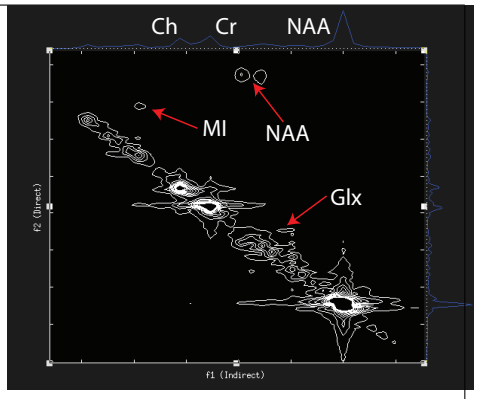

FIGURE 3: COSY data: NAA, glutamine / glutamate, and myo-inositol cross peaks are visible

3 Results

Figure 3 shows preliminary COSY data acquired from a healthy volunteer. Cross peaks are visible for N-acetylaspartate, glutamine / glutamate, and myo-inositol with a cross peak / diagonal peak ratio of .045, .33, and .32 respectively. No residual water resonance is observed. COSY acquired under using pre-saturation instead of spectral spatial refocusing gave a water / NAA ratio of approximately 100:1.

4 Conclusion

We have demonstrated an *in vivo* COSY sequence using high bandwidth, phase modulated spectral-spatial refocusing pulses. Strong metabolite cross peaks were detected even with the phase-modulated pulses. This method provides much more robust, B_1- insensitive method for water suppression for *in vivo* correlation spectroscopy.

*

[1] M. A. Thomas, *et al.*, *Magn Reson Med* **46**, 58 (2001).
[2] J. Pauly, P. Le Roux, D. Nishimura, A. Macovski, *IEEE Trans Med Imaging* **10**, 53 (1991).
[3] A. B. Kerr, *et al.*, *Proceedings of the 16th Annual Meeting of ISMRM* (Toronto, 2008), p. 226.

Evaluation of Accelerated T1ρ Acquisition Using a Combination of Compressed Sensing and Data Driven Parallel Imaging

Julien Rivoire[1], Kevin King[2] , Xiaojuan Li[1]

[1]Department of Radiology and Biomedical Imaging, Musculoskeletal and Quantitative Imaging Research, UCSF, [2]Global Applied Science Lab, GE Healthcare, Waukesha, WI, US.

Introduction: Advanced MRI cartilage imaging such as T1-rho (T1ρ) provides information associated with cartilage matrix changes and enable detection of cartilage degeneration. T1ρ measurements are relatively long since they require acquisition of multiple echoes. Parallel imaging (PI) methods are commonly used to accelerate the acquisition but the acceleration factor is limited by the number of coils used to acquire the signal. Compressed Sensing (CS) is a new method for accelerating the acquisition and does not require multiple coils. It uses the sparsity and compressibility property of the MRI signals to remove artifacts induced by under-sampling the acquisition. This technique could potentially be used to further reduce the acquisition time or to increase the resolution while keeping similar acquisition time. The aim of this study was to evaluate a combination of CS and data driven PI (ARC) acquisition [1] to accelerate T1ρ quantification.

Methods: The T1ρ MR images of an ex-vivo porcine knee were acquired using a transmit-receive 8 channels knee coil on 3.0-T scanner with a MAPS pulse sequence [2] (time of spin-lock(TSL)= 0/1/2/4/8/20/40/80ms; spin-lock frequency: 500Hz). Two measurements for each resolution (matrix: 256x128x20, 256x128x40, 3884x192x40) were performed with different net acceleration (R): non-accelerated (R=1) and R=2.3, 2.9 and 3.3 respectively. The accelerated acquisitions were reconstructed with CS followed by ARC. The CS reconstruction used a conjugate gradient solver to find an image with the minimum L1 norm of its gradient. Cartilage were segmented in 6 compartments (LFC: lateral femoral condyle; LT: lateral tybia; MFC: medial femoral condyle; MT: medial tibia; Pat: patella; T: trochlea).

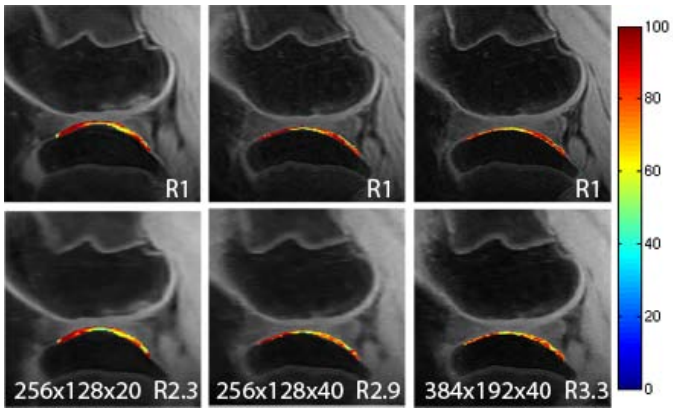

Figure 1: T1ρ maps of the medial tibia measured with different matrix size and accelerations.

Results: Figure-1 shows the T1ρ maps overlaid on the first echo of the corresponding acquisition. CS combined with ARC (bottom row) results in lower noise but appears to suffer from slight blurring. The results of the quantification in the each compartment are presented in Figure-2.

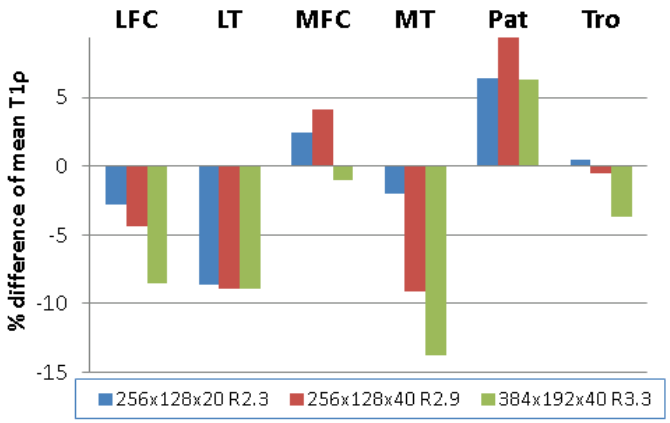

Figure 2: Percentage difference between the T1ρ value measured in the non-accelerated and the under-sampled measurement.

Discussion and Conclusion: This preliminary data shows the feasibility of combining CS and PI to accelerate T1ρ quantification. The highest quantification bias founded in these measurements was a 13.8% decrease of T1ρ in the MT compartment of the high resolution acquisition. The cartilage in MT compartment is the thinnest compartment and may suffer from greater influence of the filtering. Thus, quantitative analysis in thin structures such as the cartilage requires a robust image reconstruction and limited blurring of the images. We will further explore using correlation between echoes to improve quantification accuracy with highly accelerated acquisition.

[1] King et al, Proc ISMRM, 2010, #4881. [2] Li et al, MRM. 2008-Feb;59(2):298-307.
Acknowledgement: The research was supported by GE Healthcare.

Laminar Evaluation of T1ρ Relaxation Time in Human Knee Articular Cartilage Under Static Loading

Joseph Schooler[1,2], Justin Singh[1], Xiaojuan Li[1], Thomas Link[1], Sharmila Majumdar[1]

[1]Musculoskeletal and Quantitative Imaging Research, Department of Radiology and Biomedical Imaging, UCSF, San Francisco, CA, United States

[2]Masters of Science – Biomedical Imaging 2012 Department of Radiology and Biomedical Imaging, UCSF, San Francisco, CA, United States

Introduction

Some of the many functions of hyaline cartilage are to provide protective support, absorb mechanical load and truncate friction in synovial joints. In human knee articular cartilage, hyaline cartilage displays a characteristic laminar appearance with respect to the arrangement of collagen fibrils [1,2]. Branching out from these fibrils are associated proteoglycan (PG) and glycosaminoglycan (GAG) motifs that contribute to the tissues' ability to retain water [3].

Using MRI, there have been many proposed techniques that attempt to quantify early cartilage breakdown associated with osteoarthritis (OA) [4]. The earlier stages of OA are marked by a reduction in PG and GAG[5]. T1ρ relaxation time examines the interaction between motion-restricted water protons and their encapsulating PG matrix. T1ρ relaxation time has proved useful in the early, noninvasive quantification of biochemical changes in knee articular cartilage[5,6,7]. Correlations between elevated T1ρ relaxation time and the clinical diagnosis of OA have been previously established[8]. T1ρ relaxation time has displayed inverse relationships with PG and GAG concentrations[6]. Souza et. al.[9] showed decreases in knee articular cartilage T1ρ relaxation time under static loading conditions. However, this study did not probe laminar difference under static loading. This study investigates T1ρ relaxation time of knee cartilage in different lamina under unloaded and loaded conditions.

Materials and Methods

MR data for 10 subjects (mean age of 47y (± 11.8y), mean BMI of 24.3 kg/m2 (± 4.14), 40% female) were acquired on a 3T Signa HDx MR (GE Healthcare, Piscataway, NJ) scanner with a 8-channel phased array knee coil. Subjects were scanned supine without loading, followed by the application of a load of one half of the subjects body weight. Cartilage T1ρ maps were generated using 3D MAPSS T1ρ mapping technique [8]. A fat-suppressed, high-resolution 3D FSE CUBE (GE Healthcare, Piscataway, NJ) was acquired for clinical diagnosis and cartilage segmentation.

Six cartilage knee compartment regions of interest (ROIs) (lateral/medial femoral condyle (LFC/MFC), lateral/medial tibia (LT/MT), patella (PAT), and trochlea (TRO)) were segmented in a MATLAB (MathWorks, Natick MA) based in-house software package. 3D FSE CUBE images were registered to the first echo of the T1ρ weighted sequence prior to segmentation. Student's T-tests between loaded and unloaded scans were performed in JMPv8 (SAS Institute, Cary NC).

Results

For full-thickness, or whole compartmental ROIs, a significant (P<0.05) decrease in T1ρ relaxation time was noticed in both the MT and LT of loaded knees compared to unloaded knees, while the MFC approached significance (P=0.07). For the articular layer, significant decreases in T1ρ relaxation time were noticed in the MFC, MT, and LT. For the bone layer, a significant increase in T1ρ relaxation time was observed in the LFC with the MFC approaching (P=0.06) (Figure2).

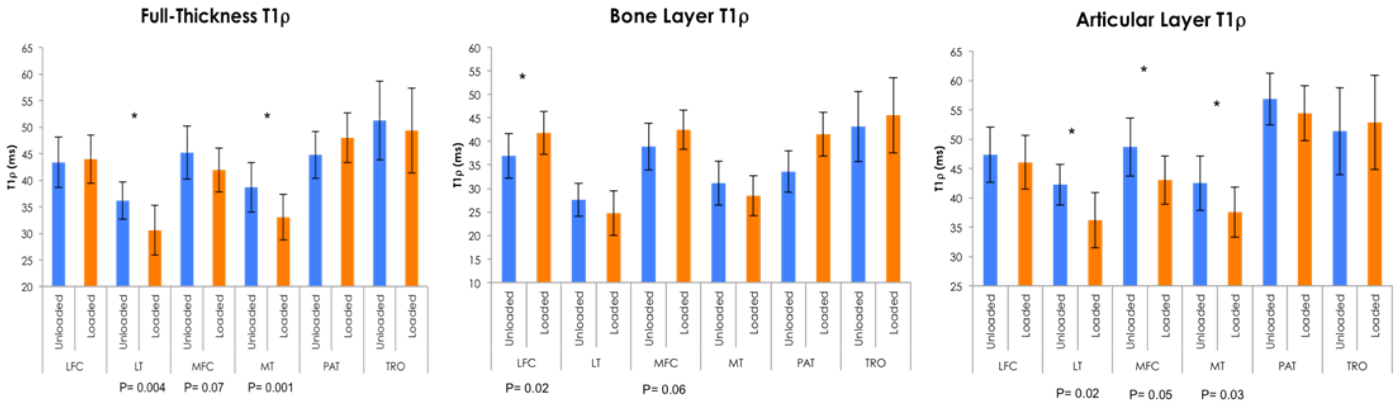

Figure 1: Full-thickness, articular and bone layer mean T1ρ values by compartment. Statistical significance indicated by asterisk and compartments approaching statistical significance with P-value displayed.

Discussion

The differences in loaded versus unloaded T1ρ relaxation time could be attributed to the way the two discrete layers respond to loading. It is possible that the load expels water from the articular layer into the bone layer, changing the motion restricted water concentration dynamic.

References

1) Cova et. al. Eur Radiol (2002) 12:814–823
3) Makin et. al. Orthopedic Basic Sciences, AAOS:1994; 3–44
2) Borthakur et al. NMR Biomed. 2006; 19: 781
4) Nieminen et. al. Magn Reson Med. 2001 Sept;43(3):487–493.
5) Akella et al, Magn Reson Med. 2001 Sept; 46(3):419-23.
6) Duvvuri et. al. Magn Reson Med 1997;38:863–867.
7) Regatte et al, J Magn Reson Imaging. 2006 Apr;23(4):547-53
8) Li X, et. al. Osteoarthritis Cartilage. 2007 July ; 15(7): 789–797
9) Souza et. al. Osteoarthritis and Cartilage 18 (2010) 1557e1563

Acknowledgements

This study was supported by NIH R01AR046905-11A1.

Mapping Microstructural Correlations of White Matter in the Human Brain Using SVC Analysis of DTI

Charvi Shetty[1], Yi-Ou Li[1], Julia Owen[1], Matthew Malter Cohen[2], BJ Casey[2], and Pratik Mukherjee[1]

[1]*Radiology, UCSF, San Francisco, CA, United States,* [2]*Sackler Institue for Developmental Psychobiology, Weill Medical Colege of Cornell University, New York, NY, United States*

Introduction

Microstructural correlations reflect phylogenetic and functional similarities between different white matter pathways [3]. Independent component analysis (ICA) has been used on group DTI data to characterize the spatial co-variation of white matter microstructure across subjects [1]. Seed-voxel correlation (SVC) analysis is often used to detect functional connectivity in resting state fMRI. These two methods are compared in a recent resting state fMRI paper finding complementary and overlapping information [2]. We demonstrate the first application of SVC to group DTI data to map white matter microstructural correlations.

Methods

200 normal adult volunteers (mean 26.4± 6.5 years, 108 men) underwent 3T DTI with 55 directions at b=1000. In FSL, FLIRT was used for motion correction, BET for brain extraction, and dtifit for fractional anisotropy (FA) calculation. We performed whole-brain registration and spatial ICA on these skeletonized FA values as described in [1]. Due to our larger cohort, we estimated 50 ICs. Z scores were computed for each of the IC maps and were thresholded at 2.5 as in [1]. The seed regions for SVC were obtained from the largest cluster in each thresholded IC map. The FA values in the seed region were averaged and the Pearson correlation coefficient was computed between the seed and every voxel on the FA skeleton with FSL's General Linear Model [4]. The correlation maps were then transformed to Z score maps and thresholded at $p < 0.05$ after false discovery rate (FDR) correction for multiple voxel-wise comparisons.

Results

As in the recent ICA of DTI study [1], voxels with the strongest FA correlations in most IC spatial maps corresponded to distinct white matter tracts, tracts segments, and/or homologous pairs of tracts. In addition to the five main groups previously found, we identified another dominant feature that could be classified as prefrontal tracts. We found 36 IC maps where the FA correlations corresponded to meaningful anatomical white matter regions. The SVC and IC maps were similar for these 36 pairs, as shown in Figure 1, with SVC confirming the unilateral, bilateral and midline FA correlations previously shown with ICA [1]. We used weighted spatial correlation [2] between each IC and SVC map to create the similarity matrix shown in Figure 1. We place the IC maps along the x-axis and the SVC maps along the y-axis, hence this matrix is not symmetric. The high values along the main diagonal demonstrate the SVC maps are most similar to their corresponding IC map. Figure 2 shows a corresponding pair of IC and SVC maps from each of these six groups; the seed region is shown in green for the SVC maps. In general, IC maps empirically thresholded at Z>2.5 exhibit more sparsity than the corresponding SVC maps, as can be seen from Figure 2.

Figure 1: Weighted Spatial Correlation

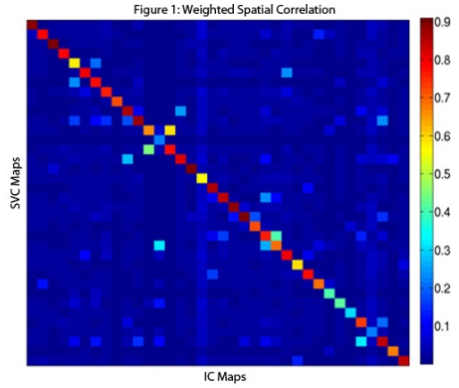

Figure 2: Example Pairs of IC and SVC Maps

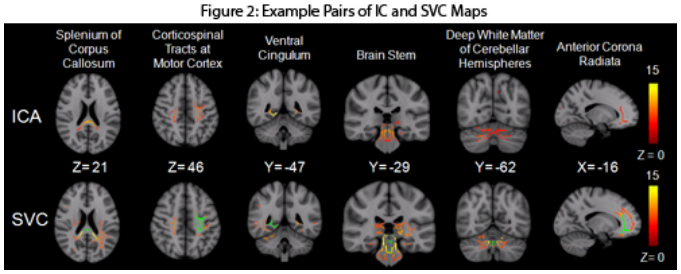

Discussion

In this study, we reveal additional spatial correlations of FA and demonstrated that SVC can be used to map white matter microstructural correlations. Advantages of SVC over ICA include the ability to perform hypothesis-driven mapping of microstructural correlations of specific white matter regions and the ability to specify a principled statistical threshold for defining regions of significant correlations. ICA and SVC can play complementary roles in mapping white matter microstructural correlations from group DTI data.

References

[1] Li, Y. (2011), 'Independent component analysis of DTI reveals multivariate microstructural correlations of white matter in the human brain', Human Brain Mapping, doi: 10.1002/hbm.21292.

[2] Suresh, J. (2011), 'On the relationship between seed-based and ICA-based measures of functional connectivity', Magnetic Resonance in Medicine, vol. 66, no. 3, pp. 644-657.

[3] Wahl, M. (2010), 'Microstructural correlations of white matter tracts of the human brain', Neuroimage, vol. 51, no. 2, pp. 531-541.

[4] http://www.fmrib.ox.ac.uk/fsl/

Calibrationless Parallel Imaging Reconstruction for Hyperpolarized ^{13}C Metabolic Imaging

P. J. Shin[1], **S. Hu**[1], **M. A. Ohliger**[1], **P. E. Z. Larson**[1], **M. Lustig**[2], and **D. B. Vigneron**[1]
[1]Department of Radiology and Biomedical Imaging, University of California at San Francisco,
[2]Department of Electrical Engineering and Computer Science, University of California at Berkeley, Berkeley

Introduction Hyperpolarized ^{13}C MR techniques enable monitoring of injected ^{13}C substrates and their metabolic products *in vivo*. Many technical challenges arise when extending the techniques to clinical applications, including the limitation of spatial coverage and T_1 relaxation of the pre-polarized ^{13}C signal. By using phased-array coils, parallel imaging (PI) offers significant acceleration. For accurate data reconstruction, either explicit coil sensitivities or sufficiently sampled calibration data in *k*-space is needed. However, these requirements can be prohivitive to achieve in hyperpolarized ^{13}C experiments. In this work, we show a calibrationless parallel imaging reconstruction method for 3D MRSI hyperpolarized [1-^{13}C]-pyruvate metabolic imaging.

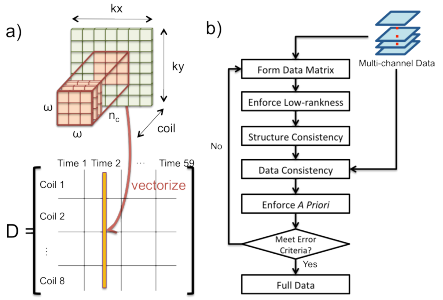

Figure 1 a) Data matrix is formed from entire coil data across all time points by vectorizing the data blocks, b) iterative calibrationless parallel imaging reconstruction.

Theory Data matrix D built from multi-channel data has low rank (Figure 1). Assuming that coil sensitivities do not change over time, we can form a data matrix with *k*-space data acquired over multiple time points and still observe the low-rankness. Thus, under-sampled spectroscopic data can be fully reconstructed by iteratively enforcing low-rankness (hard thresholding on the rank of D), structural consistency on the data matrix, data consistency with the acquired data.

Method *Simulated Experiment* K-space data of a numerical phantom containing ^{13}C compounds were generated analytically with a matrix of size 24×24×59×8 (kx-ky-time-coil). Data has been randomly under-sampled by a factor-of-four with 4x4 fully sampled center. Window size of 6x6x8 was used to generate the data matrix. Reconstruction performance were evaluated over different rank value and number of iterations (up to 300 iterations).

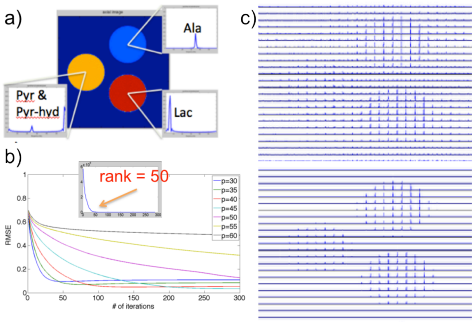

Figure 2 a) Numerical phantom, b) normalized root-mean-squared-error (nRMSE) over different values of rank and number of iterations. Full data had rank value of 50 and enforcing lower rank converges faster with higher error. c) 2D spectra of under-sampled data (top) and reconstructed data (bottom). Aliasing in spatial and spectral dimension is much reduced.

In Vivo Experiment Hyperpolarized [1-^{13}C]-pyruvate was injected to a normal male Sprague-Dawley rat. MRSI data was acquired using a 3D EPSI pulse sequence with a factor-of-four random under-sampling in kx-ky-time dimension and an 8-channel paddle-array ^{13}C receiver coil (Figure 3). Data acquisition started 25 seconds after the pyruvate injection and lasted for 13.5 seconds. Final matrix size was 24x16x16x59x8 (kx-ky-kz-time-coil) with 1cm^3 spatial and 10Hz spectral resolution. Reconstruction was done enforcing rank of 50 with 550 iterations and joint sparsity on the multi-channel spectra was additionally enforced for better reconstruction [4].

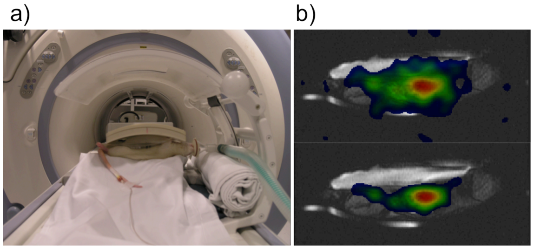

Figure 3 a) Animal experiment setup, b) pyruvate metabolic image of zero-filled (top) and fully

Result Reconstruction through proposed algorithm with rank value 50 and 550 iterations shows good result with nRMSE value less than 0.03. Reconstruction result from *in vivo* data also shows reduced spatial and spectral aliasing.

Conclusion Here, we have developed a powerful parallel imaging reconstruction method for hyperpolarized ^{13}C MR. Sequentially enforcing the desired characteristics that the data set should have, we can effectively reconstruct a full data set from a highly under-sampled one.

MRI of Ankle Tendon Pathology: Benefits of Additional Axial STIR Imaging to Reduce Magic Angle Effects

Waraporn Srikhum, Lorenzo Nardo, Dimitrios C. Karampinos, Gerd Melkus, Theresa Poulos, Lynne S. Steinbach, Thomas M. Link

Abstract

Objectives

The goals of this study were (i) to quantitatively assess the impact of STIR imaging on reducing magic angle related tendon signal alterations, (ii) to determine the value of adding an axial STIR sequence for evaluation of ankle tendons into the routinely used MRI ankle protocol, and (iii) to study the advantages and disadvantages of the axial STIR sequence compared to the axial fat-suppressed intermediate-weighted fast spin-echo (FSE) sequence.

Methods

Axial STIR sequences were used to measure normal tendon T1 and to estimate signal loss due to the inversion recovery preparation of our clinical protocol. In addition, 102 ankles were imaged with axial fat-suppressed intermediate-weighted FSE and STIR sequences. Two radiologists analyzed the tendons for signal intensity, size, abnormalities, and magic angle effect. A paired Student's *t*-test was used to calculate the differences of identified signal intensity and tendon size alterations, tendon abnormalities, and magic angle effect between those two sequences. The diagnostic value of the two sequences was compared and kappa statistics and agreement percentage were used to assess inter- and intra-observer reliability. Comparison of image quality was assessed in a side-by-side analysis.

Results

We calculated a 50% reduction of signal intensity in healthy tendons on the STIR sequence at TI=170ms compared to TI=0ms, explaining the decrease in magic angle effect in the STIR sequences. Using the STIR sequence, our study demonstrated significantly lower signal intensity within the tendons, more precise tendon size, and lower magic angle effect compared to the standard intermediate-weighted FSE sequence ($p<0.001$). Diagnostic classification of tendon abnormalities using the STIR sequences showed higher sensitivity (97.96% vs.96.87%) and better agreement with a reference standard than the intermediate-weighted sequences. Image quality of the STIR sequences was superior to the intermediate-weighted FSE sequences in visualization of the ankle tendons and of any tendon abnormality ($p<0.01$).

Conclusions

The axial STIR sequence showed a lower prevalence of increased signal intensity in the ankle tendons due to magic angle effects in comparison to the more routinely used axial fat-suppressed intermediate-weighted FSE sequence. The STIR sequence also provided better visualization of ankle tendon anatomy and pathology, and could therefore be beneficial as an alternative sequence for the evaluation of ankle tendons.

Multiparametric MRI to Identify and Characterize Prostate Cancer

Starobinets O[1], Simko J[2], Kurhanewicz J[1,3], Carroll P[4], Greene K[4], Noworolski SM[1,3]
Departments of: [1]Radiology and Biomedical Imaging, [2]Pathology, and [4]Urology, UC San Francisco
[3]Graduate Group in Bioengineering, University of California, San Francisco and Berkeley

Introduction:

Current methods used to diagnose and characterize prostate cancer cannot always distinguish between cancerous and non-cancerous tissues nor differentiate based upon aggressiveness of the disease. The purpose of the study was to use semi-quantitative parameters derived from dynamic contrast-enhanced (DCE) MRI, diffusion MR and MRI to 1) determine whether these measures can distinguish cancerous from non-cancerous cystic atrophy (a benign tissue found in virtually all prostates), identified by step-section histopathology of the excised gland, and 2) differentiate cancers based upon Gleason score.

Methods:

Thirty two men with untreated prostate cancer received 3T MR scans prior to undergoing prostatectomy. DCE imaging was performed using a 3D FSPGR sequence with TR/TE/flip=5/2.1ms/6°, 2.7mm slices, and a single-dose of Gd-DPTA over ~5 minutes. Post prostatectomy, prostate specimens were processed whole-mount. During histological review, cancerous regions were outlined and graded. ROIs were manually drawn on T2-weighted images based on the digitized histopathology slides, keeping within homogeneous regions. Separate ROIs were drawn for different cancer grade lesions within an individual. 197 cancer ROIs were drawn. This study looked at cancer regions that contained more than 50% cancer, in peripheral zone: Gleason 6 (n=44 regions were outlined in N=15 patients), Gleason 7 (n=39, N=12), and Gleason 8 (n=22, N=9), in central gland: Gleason 6 (n=13, N=4), Gleason 7 (n=5, N=2), and Gleason 8 (n=1, N=1). Noncancerous cystic atrophy regions in both peripheral zone and central gland (n=137, N=28 patients) were identified.

MR apparent diffusion coefficient (ADC), fractional anisotropy (FA) and DCE MRI parameters: time to peak, maximal enhancement slope, peak enhancement, and washout slope were calculated for each group of interest. Cancer regions were compared among grades and to cystic atrophy regions. Within each individual, ROIs were grouped in accordance to tissue type and a weighted average based on ROI areas was calculated for each metric of interest. Due to low numbers, central gland cancer regions were grouped together. Peripheral zone cancers were also grouped into less aggressive (G3+3 and G3+4), and more aggressive (G4+3 and higher) and compared to cystic atrophy.

Results:

In central gland, significant differences between cancerous and cystic regions were noted on T2w images ($p<0.01$), ADC ($p<0.01$), and FA ($p<0.02$). In peripheral zone, significant differences between cancerous regions and cystic atrophy were observed, as shown in Figure 1. While not statistically significant, a promising trend in distinguishing cancer lesions based on their Gleason scores was noted. When cancer regions were separated into less aggressive and more aggressive groups, not only were significant differences between cystic atrophy and cancerous regions noted on ADC ($p<0.05$), washout slope ($p<0.05$), peak time ($p<0.02$), and enhancement slope ($p<0.025$), but also ADC decreased and maximum enhancement slope increased from the less to the more aggressive cancers, $p<0.05$ and $p<0.025$ respectively.

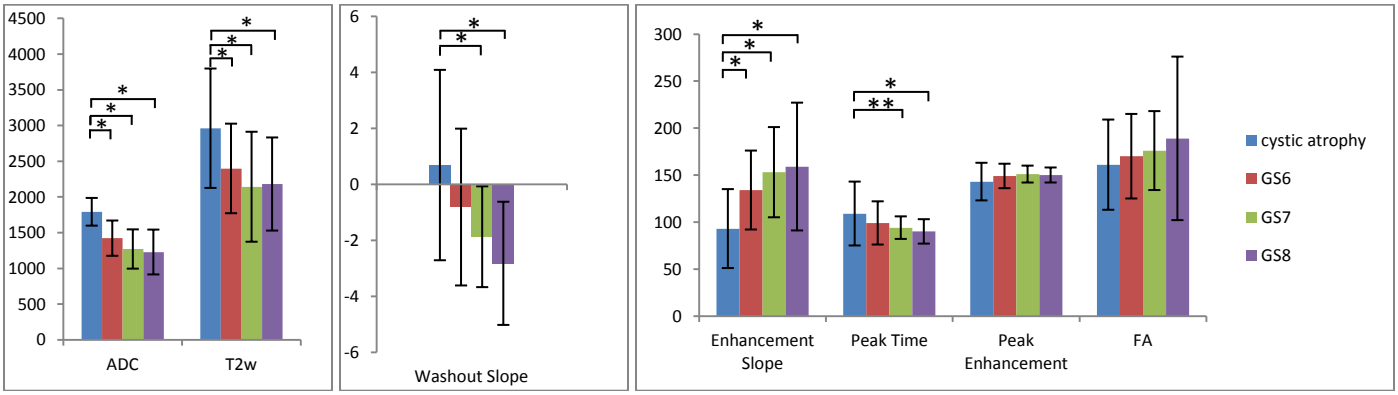

Figure 1: Average MR Measures: ADC (x10^{-3}mm^2/sec), T2w intensity (AU), washout slope (%base/min); enhancement slope (%baseline/min), peak time (sec), peak enhancement (%baseline), FA measures (%) plotted for cystic atrophy, Gleason Score (GS) 6, GS7, GS8 cancer groups. Error bars reflect standard deviation, *$p<0.01$, **$p<0.05$

Conclusion:

Prostate cancer demonstrated significantly different MR measures than histopathologically identified noncancerous regions of cystic atrophy. In characterizing prostate cancer, DCE measures showed promise at discriminating Gleason grades; which was significant when grouped into less aggressive (G3+3 and G3+4) and more aggressive (G4+3 and higher) peripheral zone cancers.

Regional Analysis of Cartilage MR Relaxation Times in Hip Joints with and without Femoroacetabular Impingement

K. Subburaj[1], C.R. Wyatt[1], A. Valentinitsch[1], A.B. Dillon[1], R.B. Souza[1,2,3], X. Li[1], T.M. Link[1], T.P. Vail[3], S. Majumdar[1]

[1] *Musculoskeletal and Quantitative Imaging Research, Department of Radiology and Biomedical Imaging*
[2] *Department of Physical Therapy and Rehabilitation Science*
[3] *Department of Orthopaedic Surgery*
University of California San Francisco, San Francisco, CA, United States - 94158

PURPOSE: The objective of this study was to perform a sub-regional analysis of cartilage magnetic resonance (MR) relaxation times ($T_{1\rho}$ and T_2) measurements in the hip joint for early assessment of cartilage defects in patients with femoroacetabular impingement (FAI).

METHODS: Morphological and quantitative images of the hip joints of 12 healthy volunteers (Age = 29.9±10.9 years; BMI=23.5±2.8 kg/m^2) and 9 FAI patients (Age = 36.6±9.7 years; BMI = 26.2±6.9 kg/m^2) were obtained using a 3T GE MR scanner and an 8-channel phased array cardiac coil. Both femoral and acetabular cartilage layers in each joint were semi-automatically segmented on sagittal 3D high-resolution spoiled gradient echo (SPGR) images. These segmented regions of interest (ROIs) were automatically divided radially into twelve equal sub-regions (30^0 intervals) based on the fitted center of the femur head (figure 1). The mean value of $T_{1\rho}/T_2$ was calculated in each sub-region after superimposing the divided cartilage contours on the MR relaxation ($T_{1\rho}/T_2$) maps to quantify the relaxation times.

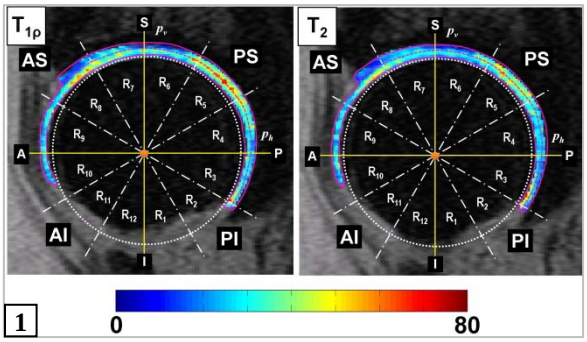

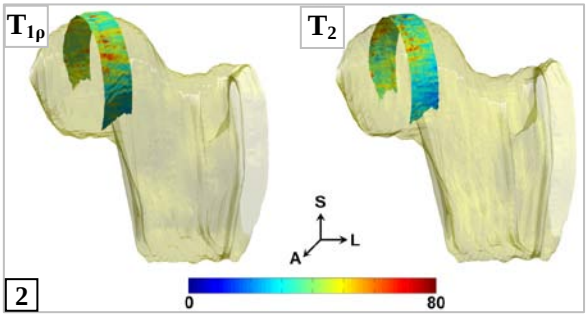

RESULTS AND DISCUSSION: $T_{1\rho}$ and T_2 relaxation times of the femoral cartilage were significantly higher in FAI subjects compared to healthy controls (39.9±3.3 msec in FAI vs. 35.4±2.3 msec in controls for $T_{1\rho}$ (P=0.0020); 33.9±3.1 msec in FAI vs. 31.1±1.7 msec in controls for T_2 (P=0.0160)). The mapping of the cartilage $T_{1\rho}$ and T_2 maps onto the 3D representation of the segmented femoral head are shown in figure 2. Sub-regional analysis showed significantly different $T_{1\rho}$ and T_2 relaxation times in the anterior-superior region (R9) of the hip joint cartilage between subjects with FAI and healthy subjects, suggesting possible regional differences in cartilage matrix composition between these two groups (Fig. 3 and Fig. 4). Receiver operating characteristic (ROC) analysis showed that sub-regional analysis in femoral cartilage was more sensitive in discriminating FAI joint cartilage from that of healthy joints than global analysis of the whole region ($T_{1\rho}$: area under the curve (AUC) =0.981, P=0.0001 for R9 sub-region; AUC=0.901, P=0.002 for whole region; T_2: AUC=0.976, P=0.0005 for R9 sub-region; AUC=0.808, P=0.0124 for whole region).

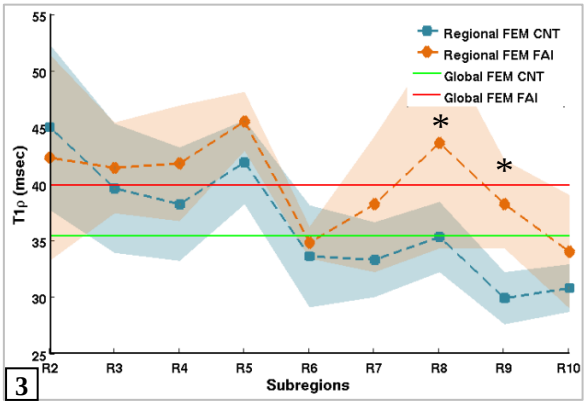

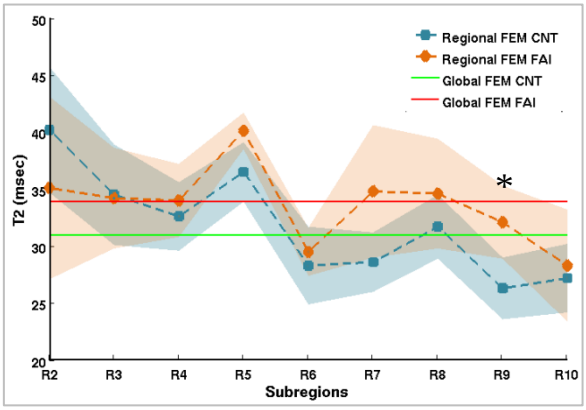

CONCLUSION: This study demonstrated (a) variations in regional composition at the hip cartilage using MR relaxation times ($T_{1\rho}$ and T_2), (b) analysis based on local regions is more sensitive than global measures of hip cartilage composition, and (c) that cartilage degeneration in subjects with and without femoral-acetabular impingement may be region-specific.

Keywords: MRI, Hip, Cartilage, $T_{1\rho}$ and T_2, femoral-acetabular impingement

Funding Source: NIH/NIAMS #P50AR060752 (SM), NIAMS U01 AR055079 (SM)

Single-shot, 2D and 3D Dynamic Imaging of Hyperpolarized 13C Biomarkers In Vivo at 14.1 Tesla

Subramaniam Sukumar, Simon Hu, Peder E. Larson, Vickie Y. Zhang, Michael Ohliger, Robert Bok, John Kurhanewicz, and Daniel B. Vigneron

Department of Radiology and Biomedical Imaging, UCSF,

Introduction

MRSI using hyperpolarized (HP) ^{13}C biomarkers can provide novel biochemical and physiological information and has been used to detect and characterize tumors in murine models. The rapid loss of the HP signal due to spin-relaxation, RF pulse saturation, and metabolism require special pulse sequences. In this project we developed single-shot imaging methods based on the echo-planar/fast-spin-echo sequence (GRASE) to provide high temporal and spatial resolution for dynamic studies.

Experimental

The GRASE pulse sequence, using frequency selective pulses is shown in Figure 1. 400ul of 80mM hyperpolarized $^{13}C_1$ pyruvate was injected into a mouse via the jugular vein and 3D, single-shot images of $^{13}C_1$-lactate and -alanine were acquired every 4s.

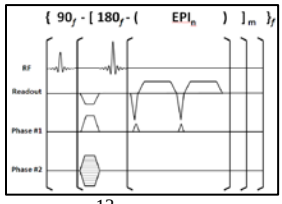

Fig. 1 - ^{13}C 3D Imaging sequence

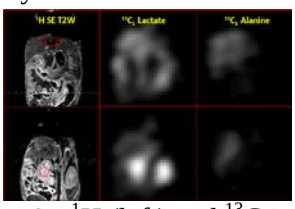

Fig. 2 - ^{1}H (left) and ^{13}C images

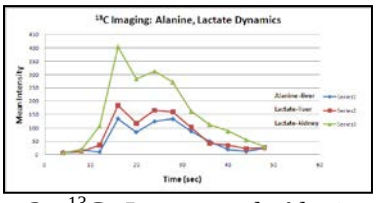

Fig. 3 - $^{13}C_1$-Lactate and -Alanine dynamics

Results and Discussion

^{13}C slices extracted from one of the 3D image is shown in Fig. 2, along with the ^{1}H reference images. Pyruvate is converted to alanine and lactate by the enzyme-catalyzed reaction of lactate dehydrogenase (LDH) and alanine transaminase (ALT) respectively. The images indicate lactate and alanine generation in the liver. High lactate signals are also detected in the kidneys. The lactate and alanine generation is better visualized in Fig. 3 where the mean signal from the liver and kidney regions (see Fig. 2) are plotted as a function of time. Since we used 90 degree excitation pulses the plot represents the rate of lactate and alanine generation during the time course experiment. Following the injection of HP $^{13}C_1$ pyruvate, its signal is rapidly depleted by metabolism and T_1. Figure 4 shows an axial, proton, reference image from a transgenic mouse prostate cancer (TRAMP) model with a large tumor along with a $^{13}C_1$ lactate (color overlay) image taken from a 2D dynamic study. After injection of HP $^{13}C_1$ pyruvate, high levels of lactate signal is detected in tumors with negligible signals from the other byproducts. Even though the tumor appears fairly uniform in the proton image, the lactate image shows a heterogeneous distribution due to differences in metabolism and perfusion (Fig. 4, 5). Dynamic plots from four regions in the tumor (Fig. 6) clearly show large differences in the rate of lactate generation. The necrotic region (series 4), for example, shows low perfusion and decreased lactate signal.

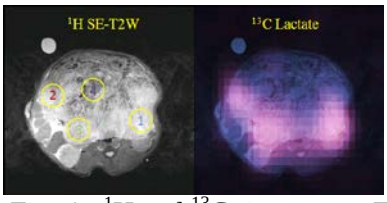

Fig. 4 - ^{1}H and $^{13}C_1$ images

Fig. 5 – 2D, dynamic, $^{13}C_1$ lactate images

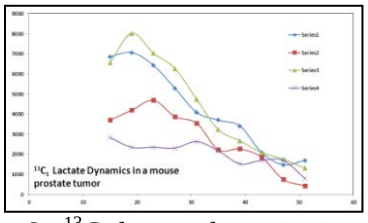

Fig. 6 - $^{13}C_1$ lactate dynamics in tumor

Summary and Conclusion

We have demonstrated, single-shot, imaging methods for obtaining 2D and 3D dynamic metabolic images *in vivo* at 14.1T. Dynamic metabolite imaging is helpful in understanding the kinetics of tumor metabolism and may help, for example, to monitor and characterize tumors during drug therapy.

Acknowledgments

NIH Grants R01-EB007588 and P41-EB013598.

Thermal ablation using resistive heating by MRI catheter in *ex-vivo* liver

Tong, R.T., M.D., Ph.D., Kolli, K.P., M.D., Rieke, V. Ph.D., Evans, L., Hetts, S. M.D., Saeed, M.,Ph.D.,and Wilson, M.W. M.D.
UCSF Department of Radiology and Biomedical Imaging

Background

Steerable endovascular catheters are designed for interventional procedures performed in clinical MRI scanners. The tips of these catheters are mounted with copper coils that create tiny magnetic moments upon application of direct electrical current (Figure 1). The byproduct of this process is the generation of resistive heating. Steerable catheters have been shown to create reproducible heating in a phantom comprised of bovine serum albumin (BSA) in polyacrylamide gel when sufficient power is applied. The goal of this study was to create a steerable endovascular catheter that can be used to perform controlled tissue ablation under real-time MRI guidance.

Results

We have demonstrated ablation catheters creating reproducible heating in ex-vivo liver (Figure 2). The maximum temperature achieved at the center of catheter is roughly linear with the power supplied by the power supply. At 1.62W, the tip of ablation catheter reached near 100°C. As power increases, the time to reach target temperature significantly decreases. For example, it takes less than 50 seconds to reach 60°C at 1.3W as compared to over 200 seconds at 1.0W. Visible irreversible changes of ablated tissue surrounding ablation catheter can be seen on gross specimen when the temperature of ablation catheter reaches above 60°C. Real time MRI thermometry study is underway to monitor temperature changes during ablation intervention. The ablation catheter will also be tested in swine to ablate liver tissue *in-vivo*.

Conclusion and future direction

Steerable endovascular catheters can be used as ablation catheters via resistive heating. In the near future, real time MRI thermometry can be used to monitor temperature changes during ablation experiments.

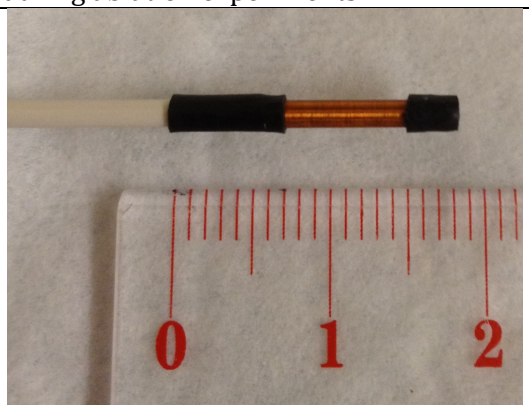

Figure 1: 5 Fr catheter with 46 AWG coil-tipped copper wire.

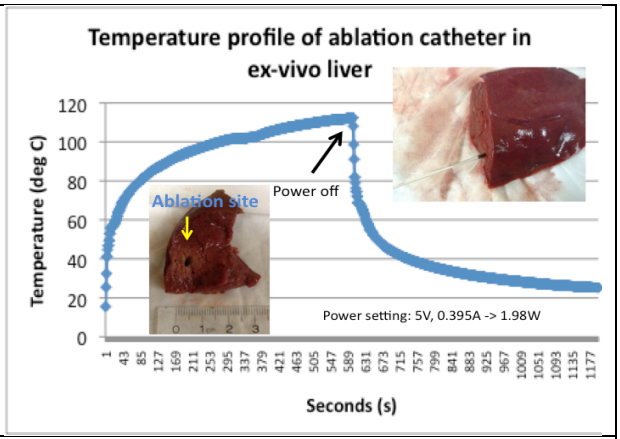

Figure 2: Temperature profile of an ablation catheter in ex-vivo liver during a heating experiment. Left lower photo demonstrates the cross sectional view of ablated area.

DEVELOPMENTAL CHANGES IN STRUCTURAL BRAIN NETWORKS

Olga Tymofiyeva[1], Christopher P Hess[1], Etay Ziv[1], Patricia N Lee[1], Hannah C Glass[2,3], Sonia L Bonifacio[3], Patrick S McQuillen[2,3], Donna M Ferriero[3], A James Barkovich[1], and Duan Xu[1]

[1]Dept. of Radiology & Biomedical Imaging, [2]Dept. of Neurology, [3]Dept. of Pediatrics, UCSF

Introduction. Understanding of how the human brain is "wired", at least on a macroscale, may become possible due to the newly emerging field of MRI connectomics. However, mapping the developing infant brain networks poses additional challenges. Recently, we developed a "baby connectome" framework for studying structural connectivity in infants that is based on an automated template-free parcellation scheme suitable for the rapidly changing developing brain [1]. The purpose of this study was to examine the maturational changes of the structural "baby connectome" in subjects of different ages, including premature neonates, term-born neonates, six-month old infants, and adults.

Methods. Diffusion MRI was performed in 5 prematurely born neonates (gestational age at scan: GA=31.14-39.71 weeks), 7 term-born neonates, and 10 six-month old babies; the two latter groups had transient encephalopathy at birth but had no evidence of brain injury. Four adults (age 24-31y) were included as a reference. The subjects were scanned on a 3T GE EXCITE MR scanner using SE EPI with a FOV=24-25.6cm, 128x128 matrix, slice thickness 1.8-2mm, 30 directions, b=600s/mm^2 for preterm babies, b=1000s/mm^2 for adults, and 700s/mm^2 otherwise. To assess structural networks, the "baby connectome" framework was employed [1], which included data quality assurance, deterministic whole-brain streamline fiber tractography (Fig. 1A), and template-free parcellation of the brain surface based on equal area sphere partitioning. The number of nodes was chosen to be 100 based on the network-driven method for determining the optimal number of nodes in six-month old babies [2]. The resulting weighted networks (Fig. 1B) were binarized (threshold=1) and network metrics were assessed using the Brain Connectivity Toolbox [3].

Results and Discussion. The characteristic path length and clustering coefficient showed a negative correlation with increasing age in term-born babies (Fig. 2). These results are consistent with a previous study on white matter maturation in subjects between ages 2 and 18 [4] and may reflect the increasing brain network efficiency and decreasing local connectivity with age. We were able to extend the age span to include younger babies by employing a template-free parcellation, which is more flexible than atlas-based approaches and suits the rapidly changing developing brain. Characterizing the maturation of the infant brain networks contributes to our understanding of how brain structure and function develop.

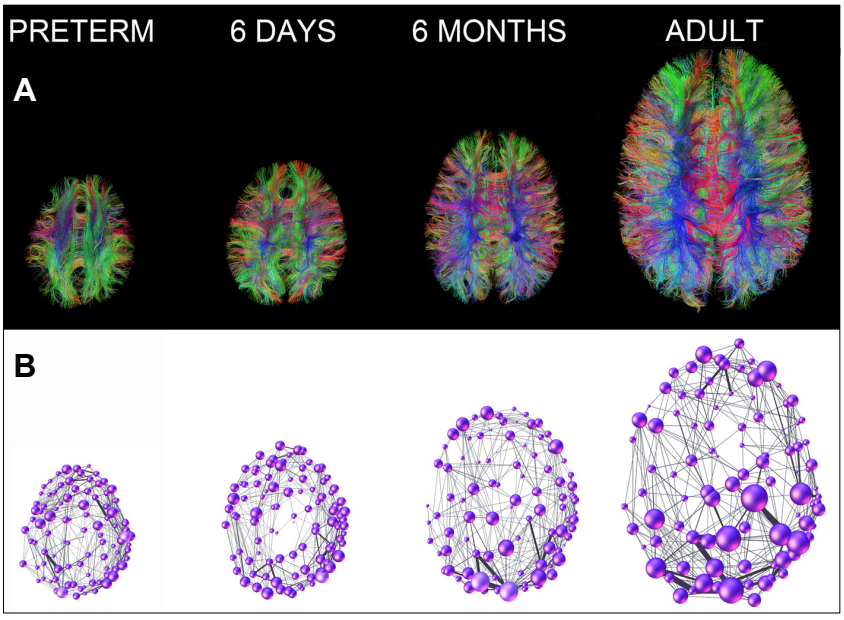

Fig 1. Maturation of the "baby connectome" - examples at four different ages. A) Tractograms. B) Weighted graphs.

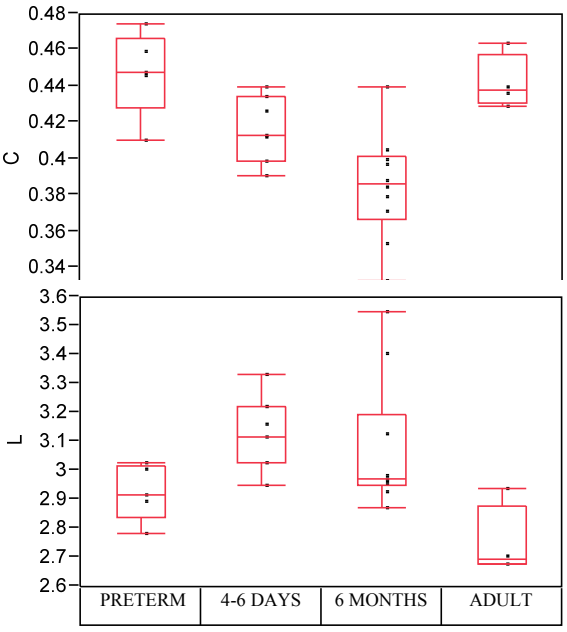

Fig 2. Variability of the clustering coefficient C and characteristic path length L.

References. [1] Tymofiyeva O et al (2012) PLoS ONE 7(2):e31029. [2] Tymofiyeva O et al (2012) Proc OHBM, #680. [3] Rubinov M & Sporns O (2010) NeuroImage 52:1059-1069. [4] Hagmann et al (2010) PNAS 107:19067-72.

Monitoring urea transport in rat kidney *in vivo* using hyperpolarized ^{13}C MRI

Cornelius von Morze Ph.D.[1], Robert A. Bok M.D. Ph.D.[1], Jeff M. Sands M.D.[2], John Kurhanewicz Ph.D.[1], Daniel B. Vigneron Ph.D.[1]
[1]Dept. of Radiology and Biomedical Imaging, UCSF, [2]Dept. of Medicine, Emory University

Introduction- Urea plays a vital role in the urinary concentrating mechanism by functioning as a key osmolyte[1]. Facilitated transporters UT-A1 and UT-A3 allow specific reabsorption of urea from the luminal fluid. Transport is required since urea is a highly polar molecule with low diffusivity across lipid bilayers. Activity of UT-A1 is acutely sensitive to antidiuretic hormone (ADH, or vasopressin), facilitating faster equilibration in the concentration of urea between lumen and interstitium of the inner medulla, resulting in more highly concentrated urine[2]. We monitored signal changes in dynamic imaging of infused hyperpolarized (HP) urea in rats in acute antidiuretic and diuretic states[3].

Methods- 99% [^{13}C]urea was dissolved in glycerol to 6.4M, with 23mM trityl radical OX063 and 1.5mM Dotarem. The sample was polarized by DNP and rapidly dissolved for a 150mM solution. Four male rats were scanned in both antidiuretic and diuretic states on the same day. For antidiuresis, rats were deprived of food and water overnight for 16hrs[3]. For diuresis, rats were allowed free access to 10% glucose water for 8hrs. Rats were placed in a 3T scanner and infused with 1.5mL 150mM urea over 6sec. A single axial slice (15 mm) was imaged every 3sec over 2min. Pulse sequence parameters: bSSFP, matrix=32x32, resolution=2.5mmx2.5mm, ±15°, TE / TR = 5.75ms / 11.5mm. Dynamic curves were plotted for renal medulla and cortex. We applied the concept of 'moment of inertia' (MOI) to measure spatial centralization of the urea signal over time, which reflects medullary urea transport since medulla is located radially inward from cortex.

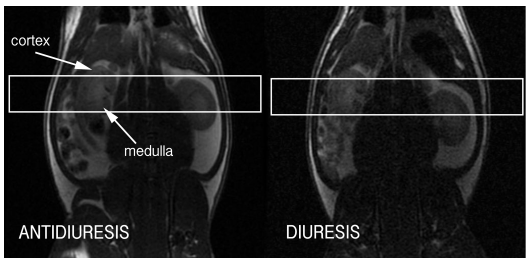

Figure 1. Coronal ^{1}H images through rat kidneys in antidiuresis (left) and diuresis (right), showing ^{13}C scan slices through rat right kidney.

Results- Dynamic images from diuretic and antidiuretic states are shown in Fig. 2. Faster medullary enhancement is evident in antidiuresis, as more rapid centralization of the urea signal. The antidiuresis MOI curve was statistically lower at any given timepoint (p= 0.0004, sign test). The mean maximum difference between curves was 6.5 ± 3.1% (p= 0.012).

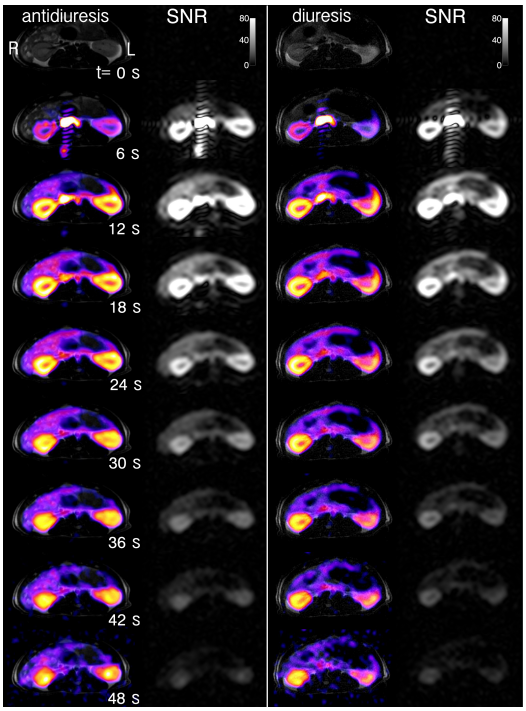

Figure 2. Dynamic renal imaging of hyperpolarized urea (color) in antidiuretic (left) and diuretic (right) states.

Discussion- By imaging HP urea, we detected increased activity of urea transporters in antidiuresis *in vivo*. Faster equilibration between lumen and interstitium results in a larger space for urea, and thus faster medullary enhancement. Glomerular filtration rate (GFR) should not vary between the two states. Monitoring urea transport *in vivo* is exciting for its role in disease states such as lithium-induced diabetes insipidus[6] and for novel diuretic drugs that inhibit urea transporters[7].

Acknowledgements- We acknowledge grant support from NIH P41EB013598-01.

References- 1. Sands and Layton. *Semin Nephrol.* 2009. 2. Klein et al. *JASN.* 2006. 3. von Morze et al. *Am Journ Physiol Renal Physiol*. 2012. 4. Kato and Sands. *Am Journ Physiol.* 1999. 5. von Morze et al. *JMRI.* 2011. 6. Klein et al. *Kidney Int.* 2002. 7. Levin et al. *Faseb J.* 2007.

High-resolution diffusion weighted imaging for the separation of benign from malignant BI-RADS 4/5 lesions found on breast MRI at 3 Tesla

DJ Wisner, N Rogers, VS Deshpande, GA Laub, DA Porter, BN Joe, and NM Hylton

Diffusion weighted imaging (DWI) has shown potential for separating malignant from benign lesions on breast MRI, theoretically improving the specificity of the breast MRI exam. However, standard DWI is hampered by multiple factors in the breast that limit utility in clinical practice. A readout segmented diffusion technique (RESOLVE)(1) permits the use of extremely short echo spacing and resamples uncorrectable data using a real-time navigator, reducing image distortion and potentially providing more accurate apparent diffusion coefficient (ADC) within lesions. In order to study the potentially utility of this method against standard diffusion, we compared ADC values from retrospectively-identified BI-RADS 4/5 (suspicious) lesions with both standard single shot-spin echo EPI (ss-EPI) and RESOLVE diffusion at 3 Tesla. All patients subsequently went to image-directed biopsy over a 10-month period.

The imaging parameters were as follows: TR/TE=7500-10000/60 ms (ss-EPI) and 8000-12000/64 ms (RESOLVE), averages=8 (ss-EPI) and 1 (RESOLVE), readout segmentation factor 5 with echo spacing of 0.3 ms (RESOLVE), slices = 47-50, b-values 0, 800 s/mm^2, resolution = 1.8x1.8x2.4 mm^3, imaging times of approximately 5 minutes for both techniques. Freehand ROI's were drawn on each suspicious lesion based on b=800 maps in close reference to the post-contrast T1 series by a board-certified radiologist who was blinded to final pathology and sequence. Similar ROI's were drawn in normal tissue as a control. For each lesion, mean ADC values and signal intensities at b=800 were recorded. ADC values were averaged by technique and pathologic outcome (benign or malignant). Signal intensity at b=800 was normalized by dividing mean signal intensity of the lesion ROI by that of the control. Significance was determined using Wilcoxon rank-sum test for ADC, and paired t-test for signal intensity measures.

Retrospective search identified a final cohort of 38 lesions in 31 patients. Of these, 9 were malignant and the remainder were benign. Two lesions were no longer present at breast MRI biopsy, and hence deemed benign. The lesion-to-background signal intensity on diffusion was higher (p=0.05) on RESOLVE (1.9±0.1) compared to standard diffusion (1.7±0.1). Statistically significant differences between benign and malignant lesion were observed for mean ADC obtained by both methods (Table 1). Between sequences, there was excellent agreement between RESOLVE and standard EPI for control values obtained from normal tissue, and for mean ADC values of benign lesions. Among malignant lesions, however, there was a statistically significant decrease in mean ADC values measured by RESOLVE (p = 0.05), which effectively widened the separation between benign and malignant lesions.

Our results suggest improved separation of benign from malignant lesions by RESOLVE compared to standard diffusion, as well as increased lesion-to-background contrast, suggesting that this diffusion method has particular promise as an adjunct to dynamic-contrast-enhanced breast MRI.

(1) Porter DA, et al MRM 2009; 62:468-75.

Table 1: Apparent diffusion coefficient (x 10^{-3} mm^2/sec) for BI-RADS 4 and 5 lesions with subsequent biopsy, obtained using RESOLVE versus standard diffusion (ss-EPI) sequence.

	Control	Lesion		
		Benign	Malignant	p
ss-EPI	1.79 ± 0.05	1.45 ± 0.05	1.00 ± 0.05	<0.001
RESOLVE	1.73 ± 0.05	1.42 ± 0.06	0.89 ± 0.04	<0.001

COMPARISON OF T1RHO IMAGING AT 3 TESLA AND 7 TESLA IN KNEE CARTILAGE

C. R. Wyatt[1], X. Li[1], R. Krug[1], D.A. Kelley[2], W. Chen[3], S. Majumdar[1];
[1] Department of Radiology and Biomedical Imaging, University of California San Francisco, San Francisco, CA, USA, [2]GE Healthcare Technologies, San Francisco, CA, USA, [3]Global Applied Science Laboratory, GE Healthcare, Menlo Park, CA, USA

INTRODUCTION: MR T1rho relaxation times have been used as markers for proteoglycan and collagen content in articular cartilage and elevated T1rho have been associated with the osteoarthritis. While these mechanisms have been studied extensively at 3 Tesla, very few studies have been done at 7 Tesla, particularly for T1rho. Kogan, et al. (MRM, 2011, DOI: 10.1002/mrm.23213) have studied T1rho relaxation using the proton transfer ratio, but have not performed T1rho mapping. To our knowledge, no comparisons of the T1rho relaxation time have been reported between 3T and 7T in vivo. In this work, we present T1rho results at 3T and 7T in vivo.

OBJECTIVE: T1rho measurement at 7T will provide increased SNR and sensitivity when compared to measurement at 3T.

METHODS: The 3D MAPSS sequence previously developed for T1rho imaging at 3T (Li, X, MRM, 2008:59) was implemented on a 7T GE MR scanner.

To determine the differences in field strength in vivo, the knee of a healthy volunteer (Male, Age 23) was imaged at 3T and 7T. Imaging parameters used for both scans were FOV=15cm, 256x128 matrix, slice thickness=4mm, spin lock frequency=200Hz, TSL=[0,10,15,45ms], TR/TE=5.2/2.9ms, slices=30, and parallel imaging (R=2.67). The bandwidth was doubled at 7T compared to 3T due to anticipated SAR limitations. Imaging at 3T was performed with an 8-channel knee coil (Invivo Inc., Gainesville, FL) while imaging at 7T was performed with a 28-channel knee coil (QED, Mayfield Village, OH). For all spin lock preparation pulses, 135° composite pulses were added to address B0 and B1 inhomogeneities.

RESULTS: Figure 1 shows the T1rho values of the phantoms at 3T and 7T. T1rho in vivo images at similar slices in the knee are shown in Figure 2. Mean values of T1rho in areas of the cartilage are shown in Table 1. SNR values at 3T and 7T are reported in Table 2

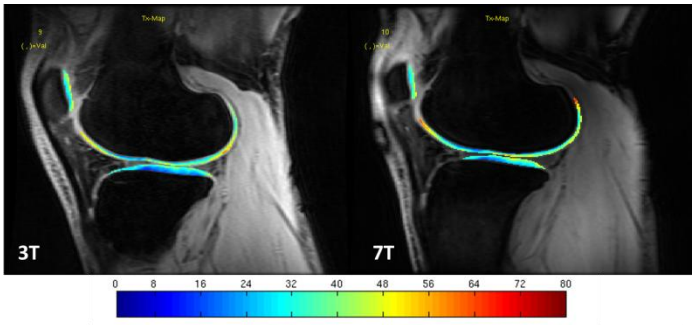

Figure 1: T1rho images at 3T/7T

Table 1: T1rho values of the cartilage

Region	3T	7T
Patella	36.61	36.50
Femoral	38.65	38.30
Tibial	27.43	31.70

Table 2: SNR value at TSL=0

Region	3T	7T
Patella	99.28	255.12
Central Cartilage	87.70	118.52

CONCLUSION: The 7T images display higher SNR, particularly in the patella. This was expected as the signal to noise ratio increases with field strength and the number of coil elements. However, these numbers are impressive considering the increased bandwidth used at 7T.

The results presented demonstrate the feasibility of 3D MAPSS T1rho imaging at 7T. Future work will involve imaging of additional healthy subjects at 3T and 7T, to provide statistical significance.

Endovascular Catheter for Magnetic Navigation under MRI Guidance: Evaluation of Heating In Vivo at 1.5T

Erin J. Yee, Mark W. Wilson, Maythem Saeed, Alastair J. Martin, Lee Evans, Anthony F. Bernhardt, Vincent Malba, Fabio Settecase, Aaron D. Losey, Prasheel Lillaney, Ryan S. Sincic, Loi Doi, Shuvo Roy, Ronald L. Arenson, Steven W. Hetts

Introduction:

Current catheter guidance techniques used in endovascular procedures face multiple challenges including difficulty navigating tortuous vessels. This can be improved by a magnetically assisted remote controlled microcatheter (MARC) system with current-carrying wires at the distal tip. A small magnetic moment generated by current at the microcatheter tip aligns with the magnetic field of an MR scanner allowing controlled deflection. Because resistive heating is a product of current application, thermal damage of vessel walls is a possible side effect. The purpose of this study was to determine a maximum level of applied current safely useable in this MARC system at 1.5T.

Methods:

Copper solenoid coils were hand-wound onto alumina tubes (Figure 1) and attached to commercially-available microcatheters (Figure 2). Catheters were tested in the carotid arteries of 8 pigs. Using X-ray fluoroscopy, catheters were advanced to the external carotid artery (ECA). Current up to 700mA was applied over time intervals ranging from 0.5 to 10 minutes during imaging to assess potential thermal damage. Current was activated at 6 or 7 locations in the carotids beginning at the proximal ECA 1 cm distal to the origin of the ascending pharyngeal artery. To assess possible RF heating and mechanical damage, experiments with no applied current were examined during MR imaging. Imaging was performed with a SSFP sequence with real-time imaging.

To conduct pairwise comparisons on the likelihood of vessel wall damage, variables examined included normal carotid arterial flow versus arterial stasis, amount of current to the catheter tip (≤ 300 mA versus >300 mA), duration of current catheter tip activation (≤1 minute versus >1 minute), and rate of guide catheter saline drip.

Carotids were sectioned and stained with hematoxylin and eosin staining, Masson's trichrome, and cleaved caspase 3 to assess vessel damage. Histological damage was analyzed with STATA version 10 using case control odds ratios, 2-sided Fisher's exact tests, and Wilcoxon log-rank sum tests.

Results and Conclusion:

Several heat mitigation techniques demonstrated negligible vascular damage compared to control arteries. Coil currents ≤300 mA resulted in no damage (0/58 samples) compared to 9/36 (25%) for >300 mA activations ($p<0.0001$). Coil activation ≤1 minute and carotid guide catheter saline drip >2 mL/minute had nonsignificantly lower likelihood of vascular damage. Catheter tip coil activations ≤300 mA for ≤1 minute in normal carotid flow, 0/43 samples had tissue damage.

Low current used to activate copper coils at the tip of microcatheters in 1.5T MR scanners can be applied without causing damage to blood vessel walls. Further optimization of catheter design and procedure protocols are necessary for safe remote control magnetic catheter guidance.

Figure 1. Hand-wound solenoid coil

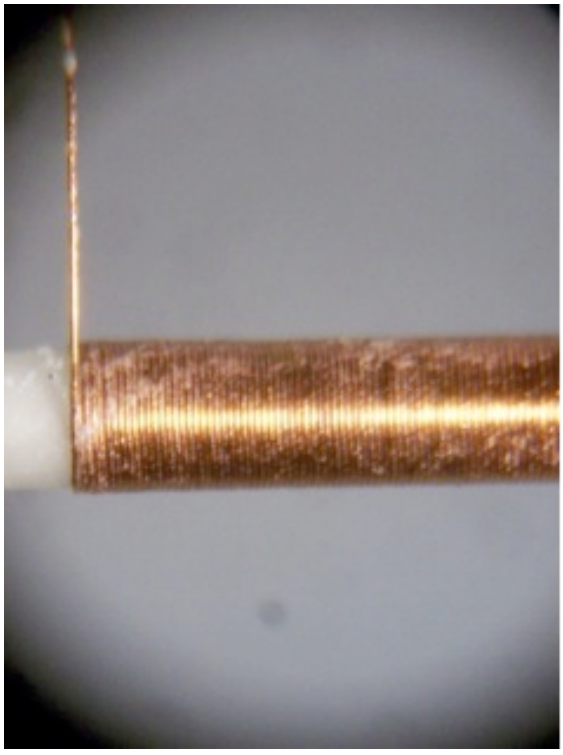

Figure 2. Magnetically Assisted Remote Control (MARC) system

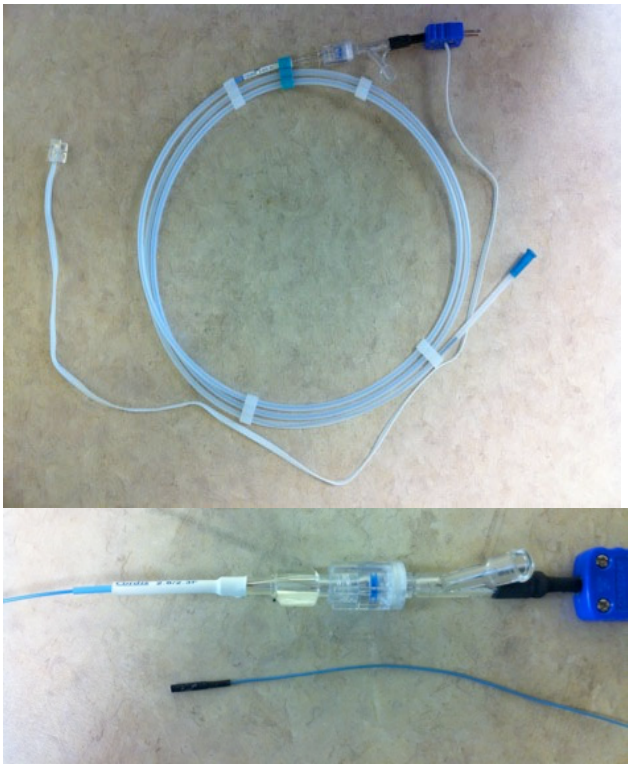

Detecting Early Tumor Response of Prostate Cancer to Radiaton Therapy using Multi-Parametric 14T ^{1}H and Hyperpolarized ^{13}C MR imaging

V. Y. Zhang[12], R. Bok[1], S. Sukumar[1], A. Cunha[3], I-C. Hsu[3], J. Pouliot[3], D. Vigneron[12], and J. Kurhanewicz[12]
[1]Dept. of Radiology and Biomedical Imaging, University of California, San Francisco
[2]Graduate Program in Bioengineering, UC Berkeley / UC San Francisco
[3]Dept. of Radiation Oncology, University of California, San Francisco,

Motivation:
Radiation therapy remains one of the most common definitive treatments for prostate cancer, but despite excellent success rates, a significant number of patients suffer post-treatment cancer recurrence. Clinical dose-escalation trials reported that higher radiation doses significantly improve biochemical control and clinical disease-free survival particularly for locally advanced prostate cancer patients. The purpose of this study was to investigate whether hyperpolarized MR can provide biomarkers of radiation dose response that could be used in future patient radiation dose escalation trials.

Objective:
Investigate the early metabolic & physiologic impact of increasing radiation dose levels (4-12 Gy) using:

- ***Hyperpolarized (HP) ^{13}C MR markers****:* [1-^{13}C] pyruvate & ^{13}C urea
- ***^{1}H MR****:* T_2 weighted, Dynamic contrast enhancement imaging (DCE), Diffusion weighted imaging (DWI)

Method:
Radioactive seed (Nucletron microSelectron-HDR) created a range of dose levels – high dose: 12-9 Gy, intermediate dose: 9-7 Gy, low dose: 7-4 Gy. 14T WB micro-imaging spectrometer (Agilent)was used. 3D GRASE imaging at 45 sec after injection of HP [1-^{13}C] pyruvate and ^{13}C urea.
Proton imaging: T_2 wt imaging, Dynamic contrast enhancement (T_1 wt gradient echo sequence, Gd-DTPA, temporal resolution = 6 sec, 0.312x0.312x1.25mm) and diffusion weighted imaging (Spin-echo sequence, b-values = 19, 182, 324, 508 s/mm^2) were acquired.

Result & Conclusion:

- HP lactate/pyruvate ratio demonstrated early changes in tumor metabolism after radiation therapy, with the ratio being reduced relative to the untreated tumor in a dose dependent fashion.
- HP urea and DCE MR demonstrated dose dependent increases in perfusion/permeability after radiation therapy.
- Increased perfusion correlated with decreased cellularity (increased ADC) measured by DWI.
- ^{1}H & HP ^{13}C MR imaging provides measures of several metabolic and physiological parameters, which can differentiate high versus low dose effects of radiation therapy.

Multivariate Analysis of Diffusion Tensor Metrics in Mild Cognitive Impairment and Healthy Aging

Y Zhang[1,2], N Schuff[1,2], K Yaffe[2], H Rosen[2], BL Miller[2], MW Weiner[1,2]

[1]Center for Imaging of Neurodegenerative Diseases, VA Medical Center and
[2]University of California San Francisco, CA USA

Introduction: Diffusion tensor imaging (DTI) is generally considered a sensitive tool [1] for the detection of white matter (WM) microstructural alterations in mild cognitive impairment (MCI), a potential precursor of Alzheimer's disease. Previous DTI studies in MCI have used univariate tests of either fractional anisotropy (FA) or radial diffusivity (DR) [2,3] that may not provide maximum sensitivity to detect WM alterations in MCI. The goal of this study was to test if multivariate tests of the three diffusion eigenvalues would be more sensitive than univariate tests using FA or DR in identifying MCI from healthy aging.

Methods: 66 healthy elderly controls (age: 67.2±10; MMSE: 29.4±1.0) and 54 MCI subjects (age: 73.3±8.7; MMSE: 27.6±2.0) had high-resolution MPRAGE and DTI (TR/TE = 6000/77ms; 2 ×2 ×3mm^3 with 40 continuous slices, 6 diffusion sensitizing directions, b = 800 s/mm^2, 4 averages, and 2-fold acceleration by parallel imaging) scans on a 4 Tesla (Bruker /Siemens) MRI system. Individual DTI images were corrected for eddy-currents, susceptibility distortions. A white matter atlas package 'JHU ICBM-DTI-81' (cmrm.med.jhmi.edu/) including 50 labeled deep WM ROIs was imported in SPM8. DARTEL algorism [4] was applied to transform FA image and WM parcellations from ICBM space onto individual FA space to obtain mean DTI metrics in each ROI. To reduce noise bias, regional DTI values were included only in voxels with FA>0.2. ROIs with visual misregistration or white matter lesions were excluded. The regional DTI data was first corrected for age and gender by cross-covariance and then the effect of diagnosis was tested on the corrected data sets using linear models. For univariate analyses, t-tests were used to determine the effect of diagnosis on the distributions of FA or DR, while for multivariate analyses, MANOVA was used to test the effect of diagnosis on the mixed distribution of the three eigenvalues l1, l2 and l3. All reported p-values are two-sided and significance is at $p<0.05$ with adjustment of a false discovery rate (FDR).

Results: Both univariate and multivariate tests showed group differences in some regions of the limbic and commissural fiber regions. However, the univariate tests of FA and DR were not entirely consistent: Specifically, univariate analyses between MCI and controls showed significant FA reduction in splenium, left isthmus posterior cingulum and fornix regions, whereas significant DR effects were found in the splenium, left isthmus posterior cingulum and bilateral uncinate fasciculi regions. In contrast to the univariate tests, the multivariate analysis of the diffusion eigenvalues captured all regions that appeared significant in FA or DR.

Conclusion and Discussion: We used multivariate analyses of all three diffusion eigenvalues to capture microstructural WM alterations in mild cognitive impairment subjects. Our results show that a multivariate analysis of the diffusion eigenvalues detects regions of white matter alterations more consistently than a univariate analysis. This method has potential to identify early cognitive impairment.

Reference:

[1] Chua TC. Curr Opin Neurol. 2008 Feb;21(1):83-92
[2] Stahl R. Radiology. 2007 May;243(2):483-92.
[3] Rogalski, Behav Neurol. 2009;21(1):51-61.
[4] Ashburner J. NeuroImage.2007 38, 95–113.